PLASTIC HINGE BEHAVIOR OF REINFORCED CONCRETE AND ULTRA HIGH PERFORMANCE CONCRETE BEAM-COLUMNS UNDER SEVERE AND SHORT DURATION DYNAMIC LOADS

By

TRICIA CALDWELL

A THESIS PRESENTED TO THE GRADUATE SCHOOL
OF THE UNIVERSITY OF FLORIDA IN PARTIAL FULFILLMENT
OF THE REQUIREMENTS FOR THE DEGREE OF
MASTER OF ENGINEERING

UNIVERSITY OF FLORIDA

2011

To my family

ACKNOWLEDGMENTS

I sincerely thank my advisors, Dr. Theodor Krauthammer and Dr. Serdar Astarlioglu, for their guidance and assistance over the course of this research, as well as the Defense Threat Reduction Agency (DTRA), the generous sponsors of this project. Finally, I thank my parents for their continued support of all of my efforts.

TABLE OF CONTENTS

LIST OF TABLES

LIST OF FIGURES

LIST OF ABBREVIATIONS

A_g	Area of gross section
A_s	Area of steel
b_w	Width of concrete section
c	Damping coefficient
c_{NA}	Neutral axis depth
d	Effective depth of element
E_c	Concrete elastic modulus
E_s	Steel elastic modulus
f_c	Concrete stress
f_c'	Compressive strength of concrete
f_c''	Maximum strength of concrete
f_s	Steel stress
f_{su}	Ultimate steel stress
f_{tj}	Tensile strength of concrete matrix
f_y	Yield stress
F	Force
F_e	Equivalent force
F_T	Total force
h	Depth of element
H	Height of element
i_{pos}	Positive phase impulse
ILF	Inertia load factor
k	Stiffness
kd	Neutral axis depth

K_e	Equivalent stiffness
KE	Kinetic energy
KE_e	Kinetic energy of equivalent system
K_L	Load factor
K_M	Mass factor
ℓ_p	Plastic hinge length
L	Length of element
m	Mass
M	Moment
M_e	Equivalent mass
M_T	Total mass
N_u	Axial load
P	Pressure
P_d	Downward pressure
P_{max}	Peak pressure
P_r	Reflected pressure
P_{S0}	Incident pressure
P_t	Transverse pressure
P_u	Upward pressure
Q_i	Reaction force per time step
R	Standoff distance
R_e	Resistance function
t	Time
T_{neg}	Duration of negative phase
T_{pos}	Duration of positive phase

$T_{pos/}$	Equivalent duration of positive phase
u	System displacement
$\dot{u}$	System velocity
$\ddot{u}$	System acceleration
U	Shock front velocity
V	Shear/reaction force
w	Point load
w/c	Water-cement ratio
w(x)	Distributed load
W	TNT equivalent charge weight
WE	Work
WE_e	Work of equivalent system
x	Location non structural element
X	Acceleration
z	Distance from the critical section to the point of contraflexure
Z	Scaled distance
α	Blast decay coefficient
β	Newmark-Beta coefficient
γ	Newmark-Beta coefficient
γ_i	Load proportionality factor
δ	Shear slip
Δ	Deflection
Δ_e	Elastic deflection
Δ_p	Plastic deflection
ε_o	Strain at maximum concrete stress

ε_c	Concrete strain
ε_{cm}	Strain at extreme compression fiber
ε_s	Steel strain
ε_{sh}	Steel hardening strain
ε_{su}	Ultimate steel strain
ε_y	Yield strain
θ	Rotation between two points
θ_e	Elastic rotation
θ_p	Plastic rotation
λ	Modification factor relative to normal-weight concrete
ρ	Longitudinal reinforcement ratio
τ	Shear stress
φ	Curvature
φ_u	Ultimate curvature
φ_y	Yield curvature
$\Phi(x)$	Shape function along element length
$\Psi(x)$	Deflected shape function

Abstract of Thesis Presented to the Graduate School
of the University of Florida in Partial Fulfillment of the
Requirements for the Degree of Master of Engineering

PLASTIC HINGE BEHAVIOR OF REINFORCED CONCRETE AND ULTRA HIGH PERFORMANCE CONCRETE BEAM-COLUMNS UNDER SEVERE AND SHORT DURATION DYNAMIC LOADS

By

Tricia Caldwell

August 2011

Chair: Theodor Krauthammer
Major: Civil Engineering

Given the prospective threat of a blast or impact load causing severe damage to a structural element or system, it is critical to investigate and understand the dynamic behavior and potential failure modes of such members. One method used to perform such an analysis in a computationally efficient manner is the programming code Dynamic Structural Analysis Suite (DSAS). The presented study's intent is to evaluate the incurrence of plastic hinges via DSAS and inspect the resultant behavior of both normal strength reinforced concrete and ultra high performance concrete columns under severe loads. Ultra high performance concrete (UHPC) is an emerging engineering technology characterized by increased strength and durability compared with normal and high performance concretes. As a relatively new material, UHPC remains to be fully characterized, and to study the material's response under simulated loading conditions contributes to widening its use, especially with respect to protective applications.

As a particularly vulnerable structural element under blast and impact loadings, columns are the specific interest of the study. To introduce the dynamic behavior of concrete columns, the analytical methods and models detailed in engineering literature

are first reviewed. The study then examines the process by which DSAS was adjusted to approximate the plastic hinge formation and respective curvature along the column length, allowing for the evaluation of concrete columns' behavioral response under various boundary and load conditions. The considered normal strength concrete and UHPC columns are subsequently compared with the output from the finite element program ABAQUS for corresponding material models as well as the simulated behavior of each other using DSAS. Such comparisons respectively intend to validate the generated models and to demonstrate the elevated properties of UHPC.

CHAPTER 1
INTRODUCTION

1.1 Problem Statement

A cyclic relationship exists between the development of protective structures and the destructive forces used against them. While advancements are made on behalf of defense engineering, so too is technology dedicated toward the improvement of weaponry. The increasing severity of explosive devices warrants an examination and improvement of the techniques used to analyze severe blast and impact forces and prepare structural entities to withstand resultant loads. Though challenging, government and engineering agencies across the globe strive to meet the adaptability inherent to and required of protective technologies. It is recognized that a number of steps may be taken to enhance defense systems and procure an increased degree of safety. For instance, in a recent report, the U.S. Army Engineer Research and Development Center (ERDC) emphasized the necessity of research and development of both advanced computational methods and structural materials to aid in disabling evolving threats (Roth et al. 2008). The time required of complex dynamic and finite element analyses is a critical facet, and it is therefore relevant to develop simplified and expedite, but nevertheless accurate, numerical methods for such work. In addition to thorough behavioral studies, the engineering of improved and/or new materials is essential to the evolution of protective structures and defense mechanisms.

The consideration of blast and impact loads involves a detailed look at the failure modes of structural elements. Of particular interest is the vulnerability of reinforced concrete columns under explosive or other detrimental attacks. Generally, the linear-elastic model of behavior for reinforced concrete is regarded as conservative and its

plasticity is ignored. Although this approach may be suitable for design purposes, a proper analysis would address the realistic aspects of the material's plastic range. The section(s) of a reinforced column reaching ultimate moment and incipient failure may exhibit the formation of a plastic hinge and an additional load carrying capacity. The inspection of these plastic rotations would be prudent and contribute to the efforts of advancing the analysis techniques of systems under severe dynamic loading.

The Dynamic Structural Analysis Suite (DSAS) is a software program developed at the Center of Infrastructure Protection and Physical Security (CIPPS) and responds to the need of numerical methods for modeling (Astarlioglu 2008). The program performs static and dynamic analyses of structural elements including reinforced concrete, steel, and masonry members. DSAS is specifically intended to analyze severe dynamic loads, and it uses single degree-of-freedom (SDOF) systems to simplify and expedite the process. With respect to reinforced concrete columns, the program considers combined axial and transverse loads as well as the effects of large deformation behavior (Tran 2009; Morency 2010). The integration of plastic hinge formation in reinforced concrete columns would supplement DSAS and allow the program to complete its analyses in a more realistic fashion than at present.

In response to the need for stronger yet feasible structural materials, ultra high performance concrete (UHPC) has emerged as a prominent research topic over the course of the past few decades. This new technology is characterized by increased strength and durability compared with normal or high performance concretes as well as an impressive resistance to blast and impact loadings. Taking advantage of such traits, the ERDC has implemented the use of UHPC in threatening environments with the

creation of an armor panel and invested in the further research and development of the material (Roth et al. 2008). As the employment of UHPC with respect to protective applications grows, it is pertinent to study the material's response under simulated impacts. Alongside a full material characterization, the ability to model UHPC via programs such as DSAS will assist in advancing its current technological state.

1.2 Objective and Scope

The culmination of the conducted research is twofold: the evaluation of DSAS's ability to recognize and account for the formation of plastic hinges in concrete columns and the analytical comparison of normal strength concrete (NSC) against the performance of UHPC as a structural material. In completing this effort, a literature review was organized to present the pertinent information supporting each function.

To fulfill the goals presented above and enhance the structural analysis software, the following items are accomplished and accordingly reported.

- Dynamic analysis techniques, such as those for blast and impact loads, are reviewed, and the current methods and algorithms by which DSAS operates are summarized.
- The theoretical background of plastic hinge formation, experimental proceedings on hinge length development, and the resultant impact on column curvature are presented. Dually, a full overview of ultra high performance concrete as a relatively new material is organized to establish its usability.
- An algorithm is verified to signify the development of plastic hinges at the critical sections of reinforced concrete columns based on the establishment of the hinge length. This algorithm is then integrated into the current DSAS programming.
- The comparison of DSAS with the finite element software ABAQUS (SIMULIA 2010) is verified with respect to material models.
- Validation of the plastic hinge algorithm for NSC and UHPC is conducted. ABAQUS is used to run simulations to be compared with the DSAS output as part of a parametric study.

1.3 Research Significance

The research and algorithm development proposed enhances DSAS and allows it to broaden its structural analysis capabilities. The verified program is subsequently capable of expediently evaluating the plastic hinge formation in reinforced concrete columns under severe dynamic loading, as well as analyzing the behavior of ultra high performance concrete employed as structural elements under similar conditions. With the introduction of plastic hinges, the program performs a more realistic analysis of column behavior and its resistance to failure, and the addition of UHPC updates the DSAS system and includes the relatively new, but technologically available, material.

CHAPTER 2
LITERATURE REVIEW

2.1 Overview

The literature review provides a comprehensive background of the structural analysis of reinforced normal strength and ultra high performance concrete beam-columns under short duration blast loads. Section 2.2 reviews methods of dynamic analysis and the assessment of pressures exerted by blasts or explosions. Section 2.3 discusses the behavioral response of reinforced concrete columns, while section 2.4 examines the impact of plastic hinge formation on concrete behavior. Finally, section 2.5 provides a thorough background on the development of ultra high performance concrete and an introduction to the material's analytical behavior.

2.2 Structural Load and Response Analysis

To design or analyze a structural element, information must be known about the loads to which it is or may be subjected. For example, Figure 2-1 illustrates a potential loading scheme of a frame. In the diagram $P_t(t)$, $P_d(t)$, and $P_u(t)$ represent pressure loads that vary over time. This section reviews the techniques used to assess a material's response to such dynamic loads. In particular, the ability to approximate the pressure emitted from a known explosive or blasting device is examined.

2.2.1 Static and Dynamic Responses

A static analysis requires only displacement-dependent forces to be considered, whereas dynamic analyses include velocity and acceleration-dependent forces. All structural systems realistically behave in a dynamic sense, however it is often reasonable to ignore the negligible effect of the time-dependent forces and conduct a static analysis using stiffness relationships. Such is not the case for time-dependent

blast or impact forces as the damping and inertial responses of a structural element become significant.

2.2.2 Dynamic Analysis Methodology

Dynamic systems may be modeled either as single-degree-of-freedom or multi-degree-of-freedom (MDOF) problems. Given the additional computational energy inherent of MDOF systems (which may have infinite degrees-of-freedom), methods for simplifying them to equivalent SDOF systems are typically sought and successfully used to expedite the analysis process (Biggs 1964).

For a SDOF system, the equation of motion is expressed as Equation 2-1, where m is the system's mass, c is the damping coefficient, k is the stiffness, $F(t)$ is the force varied over time, and $\ddot{u}$, $\dot{u}$, and u are the system acceleration, velocity, and displacement, respectively. Similarly, Equation 2-2 is used to represent the equivalent SDOF system of a more complex system, where m, k, and $F(t)$ are replaced by M_e, K_e, and $F_e(t)$, or the equivalent system parameters.

$$m\ddot{u} + c\dot{u} + ku = F(t) \tag{2-1}$$

$$M_e\ddot{u} + c\dot{u} + K_e u = F_e(t) \tag{2-2}$$

Figure 2-2 displays the representation of a beam element by its equivalent SDOF system. The equivalent system is chosen so that its displacement corresponds to that of a designated point along the length of the real system. The simply supported beam of Figure 2-2 is shown to have experienced deformation, the shape of which is expressed by the function $\Phi(x)$. This shape function of a structural member is used in the evaluation of the equivalent SDOF parameters.

The ku and $K_e u$ terms of the equations of motion apply to linear-elastic systems. For nonlinear systems the equation of motion is typically expressed by Equation 2-3,

where $R_e(u)$ is known as the resistance function. The stiffness term is no longer proportional to displacement for a nonlinear system. The resistance function, defined as the restoring force in the spring, therefore becomes dependent on the loading path of the system and its material properties rather than simply its displacement.

$$M_e\ddot{u} + c\dot{u} + R_e(u) = F_e(t) \tag{2-3}$$

Equivalent mass. The equivalent mass of a system is determined by equating the kinetic energies of the real and equivalent structures. The velocity function is estimated using the shape function by Equation 2-4. The kinetic energy of the real system is given by Equation 2-5, within which the velocity function may be replaced by Equation 2-4 to produce Equation 2-6. The equivalent system's kinetic energy is given by Equation 2-7. Finally, equating the kinetic energy equations and solving for the equivalent mass leads to Equation 2-8. Another significant value used in dynamic analysis is the mass factor (K_M), a ratio of the equivalent mass to the system's total mass (M_T), or Equation 2-9.

$$\dot{u}(x,t) = \phi(x) \cdot \dot{u}(t) \tag{2-4}$$

$$KE = \frac{1}{2}\int_0^L m(x) \cdot \dot{u}^2(x,t)dx \tag{2-5}$$

$$KE = \frac{1}{2}\int_0^L m(x) \cdot \phi^2(x) \cdot \dot{u}^2(t)dx \tag{2-6}$$

$$KE_e = \frac{1}{2} \cdot M_e \cdot \dot{u}^2(t) \tag{2-7}$$

$$M_e = \int_0^L m(x) \cdot \phi^2(x)dx \tag{2-8}$$

$$K_M = M_e/M_T \tag{2-9}$$

Equivalent load. The equivalent load of a system is determined by equating the work done by the external load on the real and equivalent structures. Like the velocity function for the equivalent mass, the displacement function is estimated using the shape function which results in Equation 2-10. The work done by the external load on the real

system is found by integrating the product of the load and displacement across the length of a member via Equation 2-11. The substitution of Equation 2-10 for the displacement function results in Equation 2-12. For a uniformly distributed load *w(t)* may be substituted for *w(x,t)* and pulled out of the integral since the load would not vary across the length of the member. The work done on the equivalent system is given by Equation 2-13. Equating the works performed by the external load, the equivalent force is given by Equation 2-14. The load factor (K_L) may then be found as the ratio of the equivalent load to the total load (F_T) or Equation 2-15.

$$u(x,t) = \phi(x) \cdot u(t) \tag{2-10}$$

$$WE = \int_0^L w(x,t) \cdot u(x,t) dx \tag{2-11}$$

$$WE = \int_0^L w(x,t) \cdot \phi(x) \cdot u(t) dx \tag{2-12}$$

$$WE_e = F_e \cdot u(t) \tag{2-13}$$

$$F_e = \int_0^L w(x,t) \cdot \phi(x) dx \tag{2-14}$$

$$K_L = F_e / F_T \tag{2-15}$$

Equivalent parameters per time step. For every time-step the mass and load factors, K_M and K_L, will be linearly interpolated by the displacement at each time-step *i*. The generalized method for determining either parameter (simply represented by *K*) is demonstrated by Equation 2-16, where $u_i < u < u_{i+1}$.

$$K = K_i + \frac{K_{i+1} - K_i}{u_{i+1} - u_i}(u - u_i) \tag{2-16}$$

2.2.2.1 Newmark-beta method

While a number of accepted methods exist for solving the equation of motion for a linear or nonlinear system subjected to dynamic loading, the technique considered within this study is a specific case of the Newmark-beta method referred to as the linear

acceleration method. This technique involves the direct integration of the equation of motion and is considered more applicable to nonlinear systems compared with other techniques. Along with the equation of motion, the two incremental time-step equations of Equations 2-17 and 2-18 are to be used, where the coefficients γ and β are to be taken as $^1/_2$ and $^1/_6$, respectively.

$$\dot{u}_{i+1} = \dot{u}_i + (1-\gamma)\cdot\ddot{u}_i\Delta t + \gamma\cdot\ddot{u}_{i+1}\Delta t \tag{2-17}$$

$$u_{i+1} = u_i + \dot{u}_i t + \left(\frac{1}{2}-\beta\right)\cdot\ddot{u}_i(\Delta t)^2 + \beta\cdot\ddot{u}_{i+1}(\Delta t)^2 \tag{2-18}$$

The initial values for u_i and $\ddot{u}_i$ should be known, and a time-step value (Δt) should be selected that establishes an accurate and stable system. The solution is considered stable if a time-step less than $^{\sqrt{3}}/_{\pi}$ times the natural period is utilized. However, a smaller time-step may be required to reach an appropriate degree of accuracy. The general procedure for determining the system behavior at each time-step is as follows:

- Compute $\ddot{u}_i$ using the equation of motion.
- Estimate a value for $\ddot{u}_{i+1}$.
- Compute u_{i+1} and $\dot{u}_{i+1}$ using Equations 2-17 and 2-18.
- Compute $\ddot{u}_{i+1}$ from the equation of motion.
- Verify convergence of $\ddot{u}_{i+1}$ or iterate until convergence is established.

2.2.2.2 Reaction forces

The support reactions of a dynamically loaded element may be analyzed following the method prescribed by Krauthammer et al. (1990). This technique expands Biggs's (1964) assumption that the inertia force distribution corresponds to the deflected shape function so as to account for structures not behaviorally perfectly elastic or plastic. Considering the beam element illustrated in Figure 2-3 with a length L, dynamic load $Q(t)$, and deflected shape function $\Psi(t)$, the procedure for determining the reaction forces is as follows:

- Calculate the reactions (Q_1 and Q_2) at the supports for each time-step (i) and report the load proportionality factors (γ_1 and γ_2) by Equations 2-19 and 2-20.

$$\gamma_{1i} = Q_{1i}/Q_i \tag{2-19}$$

$$\gamma_{2i} = Q_{2i}/Q_i \tag{2-20}$$

- Calculate the inertia load factor (ILF) by integrating $\Psi(t)$ across the beam length via Equation 2-21.

$$ILF_i = \frac{1}{L}\int_0^L \Psi(x_i)dx \tag{2-21}$$

- Estimate the inertia proportionality factors $\dot{\gamma}_{1i}$ and $\dot{\gamma}_{2i}$ by linear beam theory per time-step.

- Calculate the end reactions per time-step by Equations 2-22 and 2-23, where m is the beam's mass and X_i is the acceleration.

$$V_{1i} = \gamma_{1i} \cdot Q_i(t) + ILF_i \cdot \dot{\gamma}_{1i} \cdot m \cdot X_i \tag{2-22}$$

$$V_{2i} = \gamma_{2i} \cdot Q_i(t) + ILF_i \cdot \dot{\gamma}_{2i} \cdot m \cdot X_i \tag{2-23}$$

As for the equivalent mass and load factors, the load and inertial proportionality factors are linearly interpolated between each time-step via Equation 2-24, where γ may represent any of γ_1, γ_2, $\dot{\gamma}_1$, or $\dot{\gamma}_2$, and u is the system displacement.

$$\gamma = \gamma_i + \left(\frac{\gamma_{i+1}-\gamma_i}{u_{i+1}-u_i}\right) \cdot (u - u_i) \tag{2-24}$$

2.2.3 Blast Loads

A blast or explosion is a sudden release of energy emitted as a shock or pressure wave. Blasts may be idealized as either free-air or ground bursts, the difference being the resultant wave propagation and pressure functions. Figure 2-4 illustrates a free-air blast. For a ground burst the shock wave immediately reflects off the rigid ground surface, whereas from Figure 2-4 it is evident that a secondary reflected wave is generated for a free-air burst. The overall effect of a blast is demonstrated by the pressure-time history of Figure 2-5. At an arrival time after the blast is detonated the structure (or point) of interest experiences a spike above the ambient pressure to a

peak overpressure. As the shock wave passes, the pressure declines and drops below the ambient pressure, effectively creating a vacuum. The pressure-time history is easily divided into positive and negative phases based on whether the pressure is above or below the ambient pressure (Smith and Rose 2002).

The pressure-time history of a blast with respect to a specific point is also represented in Figure 2-6. The chart assumes that the arrival time is the start time and demonstrates the difference between the incident pressure P_{S0} and the reflected pressure P_r. The overpressure P_r is the result the shock wave's reflection off of an encountered obstacle in addition to the incident pressure.

The pressure-time history of a blast may be modeled by Equation 2-25, the modified Friendlander equation, where P_{max} is the peak pressure, T_{pos} is the duration of the positive phase, and α is the blast decay coefficient. Due to the blast load's short duration, a system's dynamic response is dependent upon the pressure impulse. The positive impulse load is found by integrating the pressure over time by Equation 2-26.

$$P(t) = P_{max}\left(1 - \frac{t}{T_{pos}}\right) \cdot e^{-t/\alpha} \tag{2-25}$$

$$i_{pos} = \int_0^{T_{pos}} P(t)dt \tag{2-26}$$

If the peak pressure and impulse are known values, the positive pressure-time history may be simplified by a triangular loading history. As Figure 2-7 details, the duration of the triangular positive phase could then be estimated by Equation 2-27.

$$T_{pos/} = 2 \cdot i_{pos}/P_{max} \tag{2-27}$$

Any number of materials may be contrived into explosives, but for ease of analysis explosive materials are typically equivocated to TNT. The size of an explosive charge may be expressed by its TNT equivalency (*W*), or the weight of TNT needed to produce

an identical effect. Blast analyses are further simplified by the use of the scaled distance parameter (*Z*). This parameter is dimensional and relates the standoff distance from an explosion (*R*) to the charge weight (*W*) by Equation 2-28.

$$Z = R/\sqrt[3]{W} \tag{2-28}$$

Curves have been prepared for the determination of a number of blast wave parameters from the scaled distance values. The U.S. Department of Defense, for instance, assembled charts for idealized spherical and hemispherical TNT equivalent explosions (Unified Facilities Criteria 2008). Using the scaled distance, functions reported include the peak positive incident and normal reflected pressures, positive incident impulse, time of arrival, duration of the positive phase, shock front velocity, and positive phase wavelength.

2.3 Structural Analysis of Reinforced Concrete Columns

This portion of the literature review summarizes the general characteristics examined during the structural analysis of a reinforced concrete column. First the stress-strain relationships for concrete and steel reinforcement as well as their potential dynamic increase factors are presented. The flexural, shear, and axial behaviors of reinforced concrete elements are then reviewed, while a detailing of large deformation behavior, including the P-delta effect and the Euler buckling model, concludes the overview of analytical behavior.

2.3.1 Stress-Strain Relationships for Reinforced Concrete Columns

The behavior of a reinforced concrete column is dependent on the stress-strain properties of its constitutive materials. The relationships between stress and strain for each of concrete and steel reinforcement are influenced by a number of parameters, and the curves presented on their behalf are idealized representations.

The modified Hognestad curve for concrete is displayed in Figure 2-8. This stress-strain relationship assumes the concrete section is unconfined and uniaxially loaded in compression. The modified Hognestad curve consists of two functions between the concrete stress (f_c) and strain (ε_c). As the stress approaches its maximum value (f_c'') corresponding to the strain ε_0, its relationship with the strain is represented by the parabolic function of Equation 2-29. After achieving the maximum strength, the stress of a reinforced concrete member is assumed to linearly decrease in relation to strain.

$$f_c = f''_c \left[\frac{2\varepsilon_c}{\varepsilon_0} - \left(\frac{\varepsilon_c}{\varepsilon_0}\right)^2\right] \tag{2-29}$$

The reference materials of Park and Paulay (1975) and Krauthammer and Shahriar (1988) address the changes in stress-strain behavior for instances of biaxial or triaxial compressive behavior or for concrete confined by circular spirals or rectangular hoops, all instances outside of the assumptions of the modified Hognestad curve. Figure 2-9 exemplifies a factored adaptation of the stress-train curve for a rectangular beam or column given the inclusion of confinement. As depicted, confinement improves the strength of a reinforced concrete member as well as the ductility through its increasing of the experienced lateral pressure.

The strength of concrete in tension is only a small fraction of that displayed in compression. The tensile strength is represented by the stress at which the concrete fractures, or the rupture strength, and it is often approximated to be between $8\sqrt{f'_c}$ and $12\sqrt{f'_c}$. The behavior may be idealized as linear using the elastic modulus observed in the compressive range.

A sample stress-strain relationship for steel reinforcement is shown in Figure 2-10. This reinforcement curve assumes that the steel bars are loaded monotonically in

tension. The function between steel stress (f_s) and steel strain (ε_s) consists of four distinct regions. The first region is characterized by the linear elastic relationship of Equation 2-30 until the steel yields, where E_s is the modulus of elasticity for the steel. A yield plateau is then observed until the strain ε_{sh} is reached. The third region (strain-hardening) is marked by a second range of increasing stress. This region spans between the yield and ultimate (f_{su}) stresses and the strain hardening and ultimate (ε_{su}) strains. Park and Paulay (1975) modeled the region by Equation 2-31, where the variable r is represented by Equation 2-32. Though not illustrated in Figure 2-10, after achieving the ultimate steel stress and strain, the final region of reinforcement's curve consists of the stress decreasing until fracture occurs.

$$f_s = E_s \varepsilon_s \tag{2-30}$$

$$f_s = f_y \left[\frac{r(\varepsilon_s - \varepsilon_{sh}) + 2}{60(\varepsilon_s - \varepsilon_{sh}) + 2} + \frac{(\varepsilon_s - \varepsilon_{sh})(60 - r)}{2(30\varepsilon_{su} - 30\varepsilon_{sh} + 1)^2} \right] \tag{2-31}$$

$$r = \left[\left(f_{su}/f_y \right)(30\varepsilon_{su} - 30\varepsilon_{sh} + 1)^2 - 60(\varepsilon_{su} - \varepsilon_{sh}) - 1 \right] / [15(\varepsilon_{su} - \varepsilon_{sh})^2] \tag{2-32}$$

2.3.2 Dynamic Increase Factors

When loads are introduced to a structural system in a dynamic sense, it has been observed that engineering materials such as concrete and steel display strengths in excess of those statically reported and held as standard (Dusenberry 2010). The degree by which an apparent strength is heightened is specified by its dynamic increase factor (DIF). DIFs have typically been linked to the strain rate imposed during loading, the value of which may exceed 100 s^{-1} for blast loads. Numerous experimental studies have been conducted and are ongoing to develop DIF curves for various materials models, and a preliminary compilation of those for concrete has been assembled by Malvar and Crawford (1998).

The high strain rate work outlined by Malvar and Crawford primarily addresses the DIFs of concrete in tension, but also briefly touches upon the effect held on concrete in compression and reinforcing steel. In tension, the concrete DIF has been shown to potentially reach 2.0 at a strain rate of 1 s^{-1} and to exceed 6.0 at a rate of 100 s^{-1}. For the higher spectrum of strain rates, the compressive concrete DIF may reach 2.0, and the DIF for steel reinforcement, 1.5.

2.3.3 Flexural Behavior and Moment-Curvature Development

The flexural behavior of reinforced concrete is typically reflected by a structural element's moment-curvature diagram. A cross-sectional view of a concrete beam or column, along with its respective strain, stress, and force diagrams, may be configured as exemplified in Figure 2-11. Given the stress-strain relationships for concrete and steel reinforcement (as previously explicated) and using the methods of strain compatibility and equilibrium, the moment-curvature curve for a concrete element may be prepared like that of Figure 2-12. An element's curvature is its rotation per unit length as well as its strain profile gradient. Based on the diagram of Figure 2-11, the curvature (φ) and moment (M) may be derived from trigonometry and the summation of moments about the neutral axis, respectively, by Equations 2-33 and 2-34. The variables ε_{cm} and kd represent the strain at the extreme compression fiber and the neutral axis depth, respectively. As part of the moment equation, f_{si}, A_{si}, and d_i are the strength, area, and depth of each longitudinal steel bar. The mean stress factor (α) is derived from the area under the stress-strain curve, while the centroid factor (γ) is related to the first moment of area about the origin of area under the stress-strain curve. These factors are expressed more specifically by Equations 2-35 and 2-36.

$$\varphi = \varepsilon_{cm} \,/\, kd \tag{2-33}$$

$$M = \alpha f''_c b(kd)\left(\frac{h}{2} - \gamma kd\right) + \sum_{i=1}^{n} f_{si} A_{si}\left(\frac{h}{2} - d_i\right) \quad (2\text{-}34)$$

$$\alpha = \left(\int_0^{\varepsilon_{cm}} f_c d\varepsilon_c\right)/(f''_c \varepsilon_{cm}) \quad (2\text{-}35)$$

$$\gamma = 1 - \left(\int_0^{\varepsilon_{cm}} \varepsilon_c f_c d\varepsilon_c\right)/\left(\varepsilon_{cm} \int_0^{\varepsilon_{cm}} f_c d\varepsilon_c\right) \quad (2\text{-}36)$$

To use Equations 2-33 through 2-36, the strain at the extreme compression fiber is varied (thereby varying curvature), and the depth of the neutral axis is determined by equilibrium of the internal forces. The given equations apply to rectangular concrete sections, though the prescribed process would be similar for irregular section areas.

With respect to flexural behavior, reinforced concrete may potentially fail by either the crushing of concrete in compression or the fracture of longitudinal reinforcement in tension. Both possibilities are to be accounted for when establishing the ultimate moment-curvature point.

2.3.4 Diagonal and Direct Shear Behavior

Two forms of shear are apparent in reinforced concrete elements: diagonal shear and direct shear. Diagonal shear occurs in coincidence with flexure. As cracks form in the tensile region of a concrete beam or column, the shear stress acts in addition to the flexural stresses to propagate secondary cracks in a diagonal direction. This behavior is illustrated in Figure 2-13. The effect of diagonal shear on the flexural behavior and failure of concrete has been determined to be a function of the longitudinal steel reinforcement ratio (ρ) as well as the shear span to effective depth ratio (a/d). For structural elements without web reinforcement, Figure 2-14 models the trend of the shear reduction factor (SRF) by which the ultimate moment is decreased to account for diagonal shear. The SRF is plotted as the ratio M_u/M_{fl}, where M_u is the ultimate moment due to the combined effort of flexure and shear and M_{fl} is the moment due solely to

flexural. To further counteract diagonal shear failure, stirrups may be placed vertically or diagonally in the concrete element to provide web reinforcement.

Direct shear is recognized by cracking perpendicular to a concrete beam or column's axis. Such behavior is typically caused by a concentrated shear force located at a support or under a point load and assumed to act independently of flexural behavior. Therefore, individual analyses may be performed for each of the flexural and direct shear failures. Figure 2-15 charts the relationship between direct shear stress and shear slip as elaborated upon by Krauthammer et al. (2002). The model consists of five regions of either linear or constant stress-slip relationships. To appropriate the diagram for dynamic loading cases Krauthammer et al. (1988) provides a shear resistance envelop that accounts for and models the effect of load reversal.

2.3.5 Axial Behavior

The column of Figure 2-1 is both transversely and axially loaded by the dynamic pressures. The diagram represents a typical loading scenario, but thus far only transverse, flexure inducing loads have been accounted for behaviorally. To consider an axial load working alone on a column, the structural member exhibits a compressive axial strength (N_u) based on the relative areas and strengths of the concrete and reinforcing steel as depicted by Equation 2-37. Given steel's superior tensile strength, the tensile axial strength of the column is based solely on the area of reinforcement.

$$N_u = 0.85f'_c\left(A_g - A_s\right) + f_y A_s \tag{2-37}$$

The consideration of an axial load's effect on a column's flexural and shear behavior has been documented in the ACI 318-08 code. For the case of flexure combined with axial compression, the experienced moment is altered as a function of

the load, column depth, and tension reinforcement depth. Also note that the P-delta effect may become predominant given axial loads (see large deformation behavior).

The effect of axial loads on diagonal shear behavior is separated into whether the loads act in tension or compression. If subjected to axial tension, the shear strength (V_c) may be calculated by Equation 2-38, where N_u is negative for tensile forces. For axial compression however, the shear strength is to be taken by Equation 2-39 with N_u/A_g expressed in units of psi. The maximum shear under this condition is to be capped at the value given by Equation 2-40. For Equations 2-38 through 2-40, A_g, b_w, λ and f_c' are defined as the gross concrete area, the concrete section width, the modification factor relative to normal-weight concrete, and the concrete compressive strength, respectively.

$$V_c = 2 \cdot \left(1 + \frac{N_u}{500A_g}\right) \lambda \sqrt{f'_c} b_w d \tag{2-38}$$

$$V_c = 2 \cdot \left(1 + \frac{N_u}{2000A_g}\right) \lambda \sqrt{f'_c} b_w d \tag{2-39}$$

$$V_c \leq 3.5\sqrt{f'_c} b_w d \sqrt{1 + (N_u/500A_g)} \tag{2-40}$$

2.3.6 Large Deformation Behavior

The large deformation behavior of a reinforced concrete column includes the column's response to deflection-dependent mechanisms such as the P-delta effect, Euler buckling, and compression and tension membrane modeling. This section highlights the critical aspects of these behaviors, but for a more detailed evaluation of each, Morency's (2010) report may be referenced.

An eccentrically loaded column will deflect laterally under an axial load. The resultant deflection will generate a secondary moment related to the axial load, an occurrence known as the P-delta effect. The "delta" may be represented by either δ or

Δ, based on the deformation reference point. The P-δ moment is produced by a column's deflection away from its initial axis, while the P-Δ effect relates to the lateral deflection of a column's joint(s). This behavior is also highly influenced by a column's classification as either short or slender. Short columns are less likely to deform enough for the secondary moment to generate and impact the whole of the structural element's behavior. Slender columns are also more likely to exhibit failure by buckling.

Buckling of slender reinforced concrete columns is based on the differential equation for an axially loaded elastic column, or Equation 2-41, where *EI* is the concrete's flexural rigidity and *P* is the applied axial load. For Equation 2-42 Euler derived the critical axial load (P_{cr}), where *n* is the mode shape, and ℓ is the unsupported member length. The Euler buckling load (P_E) corresponds to the first modal shape, as given by Equation 2-43.

$$EI\frac{d^2y}{dx^2} = -Py \tag{2-41}$$

$$P_{cr} = (n^2\pi^2EI)/\ell^2 \tag{2-42}$$

$$P_E = (\pi^2EI)/\ell^2 \tag{2-43}$$

The Euler buckling form of failure is subdivided into two categories: global, compressive buckling of a section and buckling of the longitudinal reinforcement in the areas between stirrups. For the case of global buckling, Equation 2-43 may be directly applied to the concrete element. For localized buckling of the longitudinal steel reinforcement, the critical steel stress (f_{cr}) may be approximated in terms of the steel's tangent modulus (E_t), the tie spacing (*s*), and the radius of the reinforcement (r_s) by the relationship given in Equation 2-44.

$$f_{cr} = (\pi^2E_t)/(s/r_s)^2 \tag{2-44}$$

A final result of large deformations in reinforced concrete elements is that the elements may exhibit non-linear material behavior and the development of compression and tension membranes. This behavior has been commonly documented for the case of reinforced concrete slabs, though the general theory may be expanded to include members such as beams or columns. Post initial concrete cracking, a member's flexural strength may be increased by the interaction of a membrane formed along its compressive zone. Figure 2-16 displays a simplified diagram of a beam's deflection, cracking, and formation of a compressive membrane. The illustration dually documents the beam's ability to act with a tension membrane. After full cracking of the section, only the longitudinal reinforcement remains to generate the entire member's strength. This tension membrane is often modeled by steel cable theory, as the reinforcement alone carries the flexural load until its own failure.

The analysis of compression and tension membranes is a significant contribution to the modeling of collapse mechanisms under blast and impact loadings. The procedure for such analysis has been chronicled by Morency (2010) and adapted into a methodological algorithm.

2.4 Plastic Hinge Formation

The consideration of plastic hinge formation with respect to columns or other structural elements typically lowers the conservatism behind approximating member behavior. The occurrence of inelastic curvature allows for additional load to be carried after the critical section has sustained its ultimate moment. Predicting the exact behavior of plastic hinges though is difficult and largely based on experimental evidence. Research devoted to the topic has seen varied results, particularly in relation to the calculation of plastic hinge length. It has also predominately focused on hinge

development in solely flexural members, rather than in columns enduring both flexural and axial loads. Nevertheless, analyzing the large deformations characteristic of plastic hinging and the final collapse mechanisms of reinforced concrete columns is critical of dynamic loading applications.

This section compiles the information relevant to the plasticity of reinforced concrete columns. Topics to be discussed include the formation and locations of plastic hinges, factors influencing and methods used to approximate hinge length, and the relationship between plastic hinge length and a column's moment-curvature response.

2.4.1 Plasticity of Reinforced Concrete

A concrete element, such as a beam or column, exhibits one of two behaviors upon reaching its maximum load or capacity, brittleness or ductility. Brittle failure occurs at the ultimate load and usually without significant forewarning. This mode of collapse may be avoided through selective composition of the concrete and/or the addition of steel reinforcement. Figure 2-17 illustrates the flexural response for both behaviors. If ductile, the member will continue to deflect under a load without a sudden, abrupt failure. Plastic hinges exercise concrete's ductility. Rather than fail upon sustaining its ultimate capacity, a beam or column may experience the continued absorption of energy. The allowance to exceed the elastic deformation and generate moment redistribution is a trait of the inelastic, or plastic, range of concrete behavior. The resultant large inelastic curvatures are typically braced over cracking in the concrete's tension zone by steel reinforcement.

At the location(s) deemed a critical section of a structural element, the possibility of plastic hinge formation exists. A hinge results in the inelastic rotation and moment redistribution of a member. Figure 2-18 displays the effect of a plastic hinge on a

cantilever beam's curvature: in *(a)* the reinforced beam is shown with a tip load and cracking along its tensile region, in *(b)* the corresponding moment diagram is drawn, and in *(c)* the curvature diagram details the actual and idealized curvatures of the beam (indicated by thick and dashed lines, respectively) as the plastic hinge spreads across a portion of it. The shaded region denotes the inelastic behavior and hinge rotation, the area of which is translated into a rectangular area of a certain length to simplify and idealize the diagram. Over this specific distance (the plastic hinge length (ℓ_p), curvature is assumed to jump from approaching the yield curvature (φ_y) to the ultimate (φ_u). The effect of cracking is also illustrated, as the curvature realistically peaks at each crack.

Plastic hinges are often ignored, partially due to the difficulty inherent in their prediction. Although the spread of a hinge is not easily approximated given the number of factors affecting length, the locations where a hinge may form are easily discernable.

2.4.2 Locations of Plastic Hinge Formation

As stated previously, plastic hinges form in the region where a member reaches its maximum moment. Inelastic rotation of the element occurs and the moment continues to build along its remainder. Moment is essentially redistributed given a plastic hinge.

The locality of plastic moments is dependent on a structural member's system of support and loading pattern. Figure 2-19 demonstrates the relationship between the experienced moment and the hinge formation for a cantilever column. For a cantilever column loaded at its tip, the maximum moment develops at its base, as does the hinge. If a beam is simply supported however, the location of the maximum moment, and therefore plastic hinge, will spread outward from its midpoint. If the end supports are fixed, then plastic hinges will potentially occur at the supports, while the ultimate

moment may also be subsequently reached at its midpoint forming a third hinge. Hinge location is predictable given the type of support and loading scheme.

2.4.3 Factors of Plastic Hinge Length

In early studies of plastic hinge formation in concrete members, beams were the primary focus of research. The hinge lengths were typically considered functions of concrete strength, tension reinforcement, moment gradient, and beam depth. Past research reflects a lack of consensus regarding the influence of axial load on column hinges. This conflict was addressed by Bae and Bayrak (2008), who resolved to determine the factors specifically affecting columns. In their report Bae and Bayrak listed the following factors as holding influence on the length of a plastic hinge: axial load, moment gradient, shear stress, type and quantity of reinforcement, concrete strength, and confinement in the hinge area. Of these characteristics, three were examined intently by Bae and Bayrak, namely axial load, the shear span-depth ratio, and amount of longitudinal reinforcement.

Bae and Bayrak discovered axial load to, in general, have a positive trending affect on the hinge length of a column. For a small axial load, the plastic hinge length is not substantially affected. This case of having an axial load ratio below 0.2 was cause for some experimenters deeming axial load insignificant. Larger applied axial loads have substantial influence over hinge length however, with Bae and Bayrak demonstrating that the hinge length ratio (plastic hinge length to member depth) increased from approximately 0.65 to 1.15 when the axial load ratio (acting axial load to ultimate axial load) was increased from 0.4 to 0.8. This trend is also emphasized by the relationship between hinge length, shear span-depth ratio (L/h), and axial load. The L/h ratio linearly relates to the length, and as the axial load approaches capacity the trend

steepens. Finally, Bae and Bayrak related hinge length to longitudinal reinforcement. The greater the ratio of steel area to gross concrete area, the longer the plastic hinge region stretches. Increasing the steel ratio from 2% to 10% approximately triples the hinge length for any given axial load scenario.

2.4.4. Plastic Hinge Length

The following discussion summarizes the research conducted and empirical expressions formulated for plastic hinge length as well as the applicability of such expressions to columns.

Baker (Park and Paulay 1975). For unconfined concrete Baker proposed Equation 2-45 for the plastic hinge length, where k_1, k_2, and k_3 are factors for the type of steel employed, the relationship between axial compressive force and axial compressive strength with bending moment of a member, and the strength of concrete, respectively, z represents the distance from the critical section to the point of contraflexure, and d is the member's effective depth. Equation 2-45 was based on testing the variables of concrete strength, tensile reinforcement, concentrated loads, and axial loads. Baker indicated that for a normal range of span-to-depth and z/d ratios found in practice, ℓ_p lies between 0.4d and 2.4d. Later work by Baker considered concrete confined by transverse steel and resulted in Equation 2-46 for hinge length, where c is the neutral axis depth at the ultimate moment.

$$l_p = k_1 k_2 k_3 (z/d)^{1/4} d \tag{2-45}$$

$$l_p = 0.8 k_1 k_3 (z/d) c \tag{2-46}$$

Corley (Bae and Bayrak 2008). Corley studied simply support beams and proposed that the plastic hinge length may be given by Equation 2-47. Equation 2-47

was generated after considering the concrete confinement, size effects, moment gradient, and reinforcement, and the variables of *d* and *z* are to be reported in inches.

$$l_p = 0.5d + 0.2\sqrt{d}(z/d) \tag{2-47}$$

Mattock (Park and Paulay 1975). After approximating data trends Mattock simplified Corley's expression to Equation 2-48.

$$l_p = 0.5d + 0.05z \tag{2-48}$$

Sawyer (Park and Paulay 1975). The formula for the equivalent plastic hinge length as proposed by Sawyer is given by Equation 2-49. Sawyer's expression is based on a number of assumptions regarding a member's moment distribution. The maximum moment is assumed the ultimate, the ratio of yield to ultimate moment is assumed to be 0.85, and the yield region is assumed to spread *d*/4 past where the being moment is reduced to the yielding moment.

$$l_p = 0.25d + 0.075z \tag{2-49}$$

Paulay and Priestly (Bae and Bayrak 2008). Paulay and Priestly included the influence of steel reinforcement via bar size and yield strength into their equation for the equivalent plastic hinge length of a concrete member, resulting in Equation 2-50. In Equation 2-50 L is the member length, d_b is the reinforcing bar diameter, and the steel yield strength (f_y) is to be reported in units of ksi.

$$l_p = 0.08L + 0.15d_b f_y \tag{2-50}$$

Bae and Bayrak (2008). Bae and Bayrak generated the chart represented in Figure 2-20 to compare the equivalent hinge length predictions of some of the empirical equations reviewed above. Amongst these expressions are the constant values approximated by Shelkh and Khoury and Park et al. for all shear span-depth ratios. The

variation between the equations is evident. It is also interesting to note that for several of the equations proposed *z* and *d* (the distance from the critical section to the point of contraflexure and effective beam depth, respectively) are the contributing variables.

From their experimental and parametric studies, Bae and Bayrak also produced a new equation for the plastic hinge length in a concrete column. This expression is given by Equation 2-51, where *h* is the depth of the column. All three factors examined during the parametric studies are incorporated into Equation 2-51, including axial load level, shear span-depth ratio, and amount of longitudinal reinforcement. A least squares analysis technique was used for determination of each parameter's coefficient and the procurement of Equation 2-51.

$$l_p/h = \left[0.3(P/P_o) + 3(A_s/A_g)\right](L/h) + 0.25 \geq 0.25 \tag{2-51}$$

2.4.5 Moment-Curvature and Plastic Hinges

The rotation and deflection of a structural element may be determined from its curvature. The rotation (*θ*) between two points is the result of integrating curvature along the member via Equation 2-52, where *dx* is an incremental length of the member, while the deflection (*Δ*) of the member is expressed by Equation 2-53.

$$\theta = \int_A^B \varphi dx \tag{2-52}$$

$$\Delta = \int_A^B x\varphi dx \tag{2-53}$$

Referring to Figure 2-18, the rotation between two points, or the integration of curvature, is equivalent to the area under the curvature graph. This area may be considered to have two distinct sections, specifically the elastic and plastic regions. Therefore, the rotation or deflection of a member may be calculated by adding the contribution of each region as represented by Equations 2-54 and 2-55.

$$\theta = \theta_e + \theta_p \tag{2-54}$$

$$\Delta = \Delta_e + \Delta \tag{2-55}$$

For elastic behavior, the curvature may be substituted for by the ratio *M*/*EI*, with the rotation given by Equation 2-56. In Equation 2-56 *M* is the moment and *EI* is the elastic flexural rigidity at a given location of a member. The plastic rotation may be idealized, like that in Figure 2-19, by Equation 2-57.

$$\theta_e = \int_A^B (M/EI)dx \tag{2-56}$$

$$\theta_p = (\varphi_u - \varphi_y)l_p \tag{2-57}$$

Through the use of strain compatibility and small angle approximation (as Figure 2-11 represents), the curvature may be represented by Equation 2-58, where *kd* is the neutral axis depth for a strain ε. The plastic rotation may thereby be taken as Equation 2-59, where ε_c and c_{NA} denote the strain and neutral axis depth at the ultimate moment, and ε_{cm} and *kd* represent the strain and neutral axis depth at the yield moment.

$$\varphi = \varepsilon/kd \tag{2-58}$$

$$\theta_p = [(\varepsilon_c/c_{NA}) - (\varepsilon_{cm}/kd)] \cdot l_p \tag{2-59}$$

2.5 Ultra High Performance Concrete

An emerging technology, ultra high performance concrete is predominately characterized by an increased strength and durability in comparison with normal concrete or high performance concrete (HPC). The remainder of the literature review provides a comprehensive background on this structural material. First, a broad description and the developmental history of UHPC are presented, followed by an examination of the material characterization of UHPC. A description of the UHPC manufacturing industry is narrated, noting the products marketed as Ductal©, CeraCem,

and Cor-Tuf, and finally reviews of the status of regulatory codes and the completed and potential applications of UHPC are conducted.

2.5.1 UHPC Defined

The American Concrete Institute (ACI) depicts high performance concrete as "meeting special combinations of performance and uniformity requirements that cannot always be achieved routinely using conventional constituent materials and normal mixing, placing, and curing practices" (FHWA 2005). This definition also encompasses ultra high performance concrete as it alludes to a material functioning at a level above that of normal concrete. To differentiate the term "ultra high" from "high," a limit compressive strength may be used. UHPC is commonly classified by a strength of, or exceeding, 150 MPa (22 ksi). To wholly define a concrete's performance level, a number of material properties must be evaluated, or specifications met. The Federal Highway Administration (FHWA), for example, uses freeze-thaw durability, scaling resistance, abrasion resistance, chloride ion penetration, alkali-silica reactivity, sulfate resistance, compressive strength, modulus of elasticity, shrinkage, and creep as criteria for characterizing HPC (FHWA 2005). While research is underway to document similar standards for UHPC, the comparatively new material is characterized by fewer and more general traits, namely strength, durability, and ductility (Astarlioglu et al. 2010).

UHPC is marked by high durability in addition to an impressive strength. These qualities are attributed to a low porosity, which coincides with a denser packing of the constituent molecules. A sample composition of UHPC is provided in Table 2-1. The concrete characteristically excludes the use of coarse aggregates and classically consists of Portland cement, silica fume, a superplasticizer, and steel fibers. The materials collaborate on a micro-particle level (the average size being 2.5 mm for fine

aggregate and 0.2 µm for silica fume) and induce a densification of the concrete (Rong et al. 2009). Sand and/or other fine aggregates are combined with Portland cement to create a more homogeneous and compact mixture than if large aggregates were utilized. In addition to being pozzolanic (reactive with calcium hydroxide to enhance concrete strength), silica fume particles fill void spaces left in the cement, thereby reducing porosity (Shah and Weiss 1998). Superplasticizers further promote the densification process as water-reducing admixtures. They are employed to increase the composite mixture's fluidity and allow a simultaneous decrease in the water-cement ratio, a value inversely proportional to strength.

The high compressive strength of UHPC is attributed to its mixture proportions and methods, factors dually resulting in an increased brittleness compared with normal concrete. Figure 2-21 represents the brittle behavior of UHPC via its stress-strain diagram. After reaching the peak load (peak stress), the decrease in load-carrying capacity is steeper for UHPC and HPC than for the normal concrete. The near vertical slope of the UHPC stress-strain curve (post peak capacity) illustrates the possibility of an unpredicted, rapid failure of the material. To lessen the severity of such a failure and increase ductility, micro fibers, either of steel and/or another synthetic material, may be added to the cement mix, creating a composite material commonly known as ultra high performance fiber-reinforced concrete (UHPFRC). Steel fibers strengthen the cement bonding and positively affect the cracking pattern of concrete. The fibers cause a number of micro-cracks to form in the place of large single cracks, improving both ductility and tensile strength. Embedded fibers may also limit the need for mild steel reinforcement such as stirrups used for shear or confinement reinforcement.

2.5.2 Evolution of UHPC

The development of UHPC began in the 1960s, a century after W.B. Wilkinson patented reinforced concrete in 1854. At that time, the strongest concrete had a compressive strength in the range of 60 to 80 MPa and a water-to-cement (*w/c*) ratio of 0.30 (Buitelaar 2004). Given a firm understanding of normal concrete, researchers hoped to exploit the recognized inverse relationship between strength and the w/c ratio. Concrete with a compressive strength in excess of 800 MPa was subsequently created. The material was prepared following a strict procedure however, utilizing high pressure and thermal treatment in a laboratory to drive its *w/c* ratio down (Schmidt and Fehling 2004). Though relevant to improve concrete strength, such a specialized treatment does not prove overly construction or cost effective.

Under the leadership of Hans Henrik Bache in Denmark, the idea that the ultimate strength of concrete depended on more than the selection of cementitious materials was tested. It was discovered through experimentation that strength is also dependent on the compaction of the concrete and the porosity established after the hardening process (Buitelaar 2004). Results reported in 1970 of Bache's research displayed the compressive strength increasing from approximately 60 MPa to 290 MPa when the porosity ratio was decreased from 0.6 to 0.4. The use of vibration or pressure to compact cement paste is able to substantially increase the compressive strength.

Through the 1970s alternate methods for decreasing porosity were investigated. Superplasticizers emerged as effective admixtures for improving the workability of concrete in the presence of lower water contents. They are generally sufficient in quantities of 1-2% of the cement weight, and an excessive amount will induce concrete segregation. Their development eased the dispersion of particles throughout

cementitious mixtures and led to a rise in the interest of fine particles, particularly the microsilica by-products of silicon and ferrosilicon production (Buitelaar 2004). Over a hundred times smaller than typical cement particles, silica fume acts as a void filler and compactor. Its reactivity with calcium hydroxide in the cement paste creates calcium silicate hydrate and dually enhances the molecular bonding and strength. The Danish research team led by Bache developed a superplasticizer and microsilica infused cement paste named D.S.P. By 1980 the material saw practical application in the security field, employed in the construction of vaults and other protective structures (Schmidt and Fehling 2004).

Alongside a further restriction in fine aggregate grain size (<1 mm in diameter), the cement mixtures implementing the use of reactive constituents became known as reactive powder concretes (RPC). The term “ultra high performance concrete” was established to reference a boarder scope of concretes, encompassing RPCs and other formulations reaching a compressive strength of 150 MPa (Schmidt and Fehling 2004).

As for fiber reinforcement, it became a modern development with the addition of asbestos fibers to cement paste in the early 1900s. Steel fibers, in particular, were first proposed in reports published by Romualdi in 1963-64 and have been researched and refined for over 45 years. Other well-established, though less common, reinforcements include polypropylene and glass fibers (Brandt 2008). The advantages of each material vary. Steel fibers increase fracture energy (ductility) and compressive and tensile strengths and lower concrete’s tendency toward cracking. Polypropylene fibers limit early shrinkage and micro-cracking but improve fire resistance, while glass fibers reduce the internal stresses present in early-age concrete (Orgass and Klug 2004).

Ultra high performance fiber-reinforced concrete has become a prominent research topic over the past two decades. As of the mid-1990s, multiple engineering and production companies have ventured into producing particular varieties of UHPFRC. Among the earliest companies were Lafarge and Eiffage, developing their concretes Ductal© and BSI (now CeraCem), respectively. The library of data collected, including research of its constituent materials, reinforcement, characterization, construction method, etc., has since begun to compile on an international level. Two international symposiums have been held in Kassel, Germany (in 2004 and 2008) with specific interest in UHPC. The proceedings from each symposium have been published and cover presentations on topics such as raw materials, fiber reinforcement, early age behavior, structural behavior, material modeling and predicting, impact and blast effect, and worldwide applications. Relevant data and information have also been gathered by several engineering committees into sets of preliminary design recommendations. The current research and findings on behalf of UHPC are subsequently reviewed in greater detail.

2.5.3 Characterization of UHPC

The analysis of ultra high performance concrete's material properties has been conducted across the globe by researchers seeking to fully understand their structural advantages and disadvantages. An overview of the material characteristics distinctive to UHPC ensues, and it is divided into three areas of focus. First, the effects of raw material proportions and production methods on material behavior are examined. The typical mechanical properties of UHPC are then summarized, followed by a discussion of the research pertinent to the blast and impact resistance of UHPC.

Important to the design process and structural use of UHPC, the general compressive and tensile behaviors of UHPC are illustrated in Figure 2-22. The stress-strain diagrams are representative of the employment of fiber reinforcement. Displayed are the general ranges for compressive and tensile strengths (typically 150–200 MPa and 20–30 MPa, respectively), as well as a comparison between the behaviors of UHPC and normal strength concrete. Not only does UHPC substantially surpass normal concrete in strength, but it also exhibits a fiber-enhanced ductility.

2.5.3.1 Constituent materials and mixing methods

The proportioning of raw materials and the mixing techniques utilized in concrete preparation are studied in order to generate product optimization. Raw materials such as silica fume and fiber reinforcement contribute to UHPC's functionality, provided they are employed in effective quantities, while specialized compaction and mixing methods improve the strength and durability properties of UHPC mixtures. However, for optimization purposes it is important to recognize that these noted benefits may not always prove efficient coupled with time or cost constraints. For high strength concretes the cost of production is generally proportional to the strength developed. Figure 2-23 presents this relationship as determined by the Norwegian Defence Estates Agency (Markeset 2002). The costs are normalized to the concrete strength of 45 MPa. At a point, the increase in concrete strength fails to outweigh the additional incurred cost.

Silica fume. Silica fume is added to a mixture as a percentage or ratio of the cement present. A study of silica fume's effect on the mechanical properties of UHPC was conducted by Jayakumar (2004), the results of which are organized in Table 2-2. The percentage of silica fume reported is relative to the density of ordinary Portland cement. The case of no silica fume associates with a cement density of 500 kg/m^3, and

the case of 5.0% silica fume corresponds to 23.8 kg/m^3 of silica fume and 476.2 kg/m^3 of cement. For each of the evaluated strengths, the optimum employment was at 7.5%, though the tensile and flexural strengths displayed limited improvement with silica fume.

Steel fiber reinforcement and curing time. Fiber reinforcement is added to UHPC mixes to enhance the overall ductility of the resultant concrete. Testing performed by Rong et al. (2009) examined the effect of percent volume of steel fiber reinforcement on the compressive strength, flexural strength, and toughness of UHPC. Three volume fractions (relative to the entire cementitious mixture) of steel fibers were tested: 0%, 3%, and 4%, and they are compared in Table 2-3. An increase in the quantity of steel fibers saw an increase in all values presented, particularly the toughness index. As expected of concrete, strength accrues over time, and the compressive and flexural strengths rise per an extended curing time. The benefit of employing fibers was particularly observed by a jump in flexural strength between 0% and 3% fiber content from approximately 20 MPa to 65 MPa at 180 curing days. The bonding inherent between the steel fibers and cement matrix enhances the concrete's tensile region during flexure.

Optimum mixture. Park et al. (2008) completed similar laboratory testing for each UHPC raw material and generated the sample configuration depicted in Table 2-4.

Densification and heat treatment. Teichmann and Schmidt (2004) analyzed the effect of packing density on the durability properties of UHPC. Normal, high performance, and ultra high performance concretes were differentiated by relative packing density values of 0.68, 0.71, and 0.76. The experimental outcomes are exemplified in Table 2-5. The percentages of porosity and capillary pores decrease with

an increase in the density. As a form of transportation through concrete, capillary pores promote chemical intrusion, and UHPC is evinced to provide improved defense against harmful attacks. Other durability traits evaluated were the permeability coefficient, water absorption, and chloride penetration depth of each material. The permeability coefficient dropped from 6.7E-17 m^2 for normal concrete to 0.08E-17 m^2 for UHPC, and a corresponding trend was viewed for the water absorption. Monitoring the chloride diffusion via a quick-migration test, the penetration depth of chloride into the concrete was substantially reduced by the densification (measured at 2.3 cm, 0.7, and 0.1 cm for normal, high performance, and ultra high performance concrete).

While all three materials were cured under water, a second batch of UHPC was cured under a two day heat treatment of 90°C for comparison purposes. This variation between curing techniques was reflected by a difference in compressive strengths at 28 days. The heat treatment was observed to raise the UHPC's strength from 162 MPa to 213 MPa. Also, the permeability coefficient dropped to 0.01E-17 m^2 (one-eighth of that for normally cured UHPC).

Pressure treatment. The relationship between strength and density was also emphasized by Schachinger et al.'s (2004) testing the effect of pressure treatment on cement mixtures. Multiple techniques for removing the air void content of UHPC were examined, one of which was pressurization. A mixer with vacuum capabilities was used, and the change in pressure from 1000 mbar to 50 mbar decreased the air void content from approximately 4% (of volume) to less than 1%. The specialized treatment was demonstrated to raise the compressive strength of UHPC by nearly 100 MPa, a substantial increase.

2.5.3.2 Mechanical properties and behavior

Structural materials are typically defined by their mechanical properties, and the characteristics of UHPC to be examined include the compressive, flexural, and tensile behaviors, shrinkage and creep, and the effect imposed by strain rate.

Compressive behavior. In addition to the stress-strain representation of compressive strength in Figure 2-22 and the effects held on it by various production methods, the biaxial compression behavior of UHPC has been investigated by Curbach and Speck (2008). The difference between uniaxial and biaxial behavior was exhibited by Curbach and Speck via comparison of their resultant stress-strain diagrams. The confinement caused by dually loaded axes decreases the brittle behavior of the UHPC, expressed by an extension of the stress-strain diagram.

Flexural behavior. The flexural behavior of UHPC, compared with other types of concrete such as high strength concrete, fiber reinforced concrete, and engineered cementitious composite (ECC), was investigated by Millard et al. (2009). The impressive strength of UHPC may be credited to the use of fiber reinforcement and the cracking pattern it influences. Instead of a single large flexural crack forming, a number of micro-cracks develop in the concrete. Millard et al. also prepared load-deflection curves which correspond to the energy absorption possible of the concretes, as their potential is indicated by the area under a curve. Based on such curves, the fiber reinforced UHPC had the greatest energy absorption potential of the concretes examined.

Tensile behavior. Ultra high performance concrete's tensile strength is also greatly shaped by its employment of fiber reinforcement. Habel and Gauvreau (2008) presented the general behavior, dividing it in two areas: strain hardening and strain softening. Differentiated by their manner of energy dissipation, strain hardening's loss is

considered volumetric and strain softening's loss is via localized cracking. Habel and Gauvreau represented the hardening and softening behaviors by a stress-strain curve and the relationship between stress and crack width, respectively.

Shrinkage and creep. The shrinkage and creep of UHPC under various curing methods was tested by Graybeal (2005). Although steam treatment speeds the process and the ultimate shrinkage is attained very early, the air-cured UHPC experiences less shrinkage overall. Nearly the opposite is true for creep, as the steam-cured concrete experiences approximately one-fourth of the ultimate creep of the air-cured concrete

Strain rate. The primary intent of Rong et al.'s (2009) research was to investigate the dynamic compression behavior of UHPC. Testing was carried out on specimens varied by their volume percentage of steel fibers (again, 0%, 3%, or 4%). For each UHPC and fiber configuration multiple strain rates were applied. The stress-strain relationships were prepared by Rong et al. to represent strain rates from 25.9/s to 93.4/s. Not only does the increase in strain rate amplify the peak stress attained, but it also contributes to an increase in the ultimate strain. The sensitivity to strain rate inherent of UHPC was clear from the experiments performed by Rong et al.

2.5.3.3 Blast and protection research

The enhanced material properties of ultra high performance concrete have been shown to provide notable defense against dynamic loading of a structural system, and its attributes have influenced specific interest in its use as protection from impact and blast forces. The durability and ductility of UHPC impart resistance against aggressive environments, and its increased strength allows for thinner members, which in turn reduces cost and construction needs. Blast research has been performed by Cavill

(2005) and Wu et al. (2009), while penetration testing has been conducted by Markeset (2002), the discussion and results of which follow.

The endurance of UHPC panels against blast loading was documented by Cavill (2005) after testing was conducted in 2004. The experiment at Woomera consisted of subjecting plain and pretensioned panels at three varying distances (30, 40, and 50 meters) to a six ton TNT equivalent of Hexolite. The panels had thicknesses of 50mm, 75mm, and 100mm and compressive strengths of approximately 180 MPa. The blasting resulted in minimal damages. Fractures occurred in the plain panels and the pretensioned panels subjected to the highest pressures (relative to their thickness), and the largest final deformation observed was 150 mm. The thickest and farthest placed panels appeared entirely undamaged. For all cases, spalling and fragmentation did not occur. The testing was deemed successful as all panels endured the exerted pressures, with note being given to their thinness.

Supporting the Woomera conclusions, Wu et al. (2009) studied a number of different types of concrete slabs under blasting. Two UHPC slabs were investigated, one with steel reinforcement and one without it. Each slab measured 2000 mm x 1000 mm x 100 mm, and their compressive and tensile strengths were recorded at 151.6 MPa and 30.2 MPa, respectively. The charge was suspended from a pipe and centered over a slab constrained by a steel frame. The slab lacking reinforcement had a scaled distance of 0.5 $m/kg^{1/3}$ (standoff distance of 0.75 m and 3.433 kg of explosive), while the reinforced slab had a scaled distance of 0.37 $m/kg^{1/3}$ (distanced at 1 m with 20.101 kg of explosive). After blasting, the plain slab experienced flexural cracking at its center and quarter points, as well as a final deflection of 4.1 mm. The reinforced slab,

subjected to the much larger quantity of explosive, was displayed post-blast to have crushed at mid-slab and the LVDT recording the deflection had been destroyed. Though the reinforced UHPC slab experienced considerable damage, it was deemed superior to the others by Wu et al. based on its predicted energy absorption capacity.

Finally, Markeset (2002) studied the relationship between compressive strength and penetration depth of UHPC materials. To determine the protective abilities of UHPC, the concrete samples were subjected to 45 kg, 152 mm caliber projectiles, with the average impact velocity being about 500 m/s. The experimental results were based on a penetration depth relative to a compressive strength of 30 MPa, and the penetration depth was observed to decrease by approximately half with an increase to 150 MPa. Protection is evidenced to substantially improve given the use of UHPC over normal concrete. Markeset also compared the penetration results with the cost effectiveness of UHPC production. Referencing Figure 2-23, the increased cost of creating 200 MPa concrete over 150 MPa does not appear to result in an equivalent return in penetration depth (Markeset 2002). Cost feasibility plays a significant role in the consideration of a material's use in construction projects.

2.5.4 UHPC Manufacturers

The continued development and optimization of ultra high performance concrete will ease its production and distribution over time. Currently, few UHPC mixtures or products have been commercialized. Research practices call for UHPC's production either on an individual laboratory basis or through one of the readily available manufacturers. Three examples of the industrialization of UHPC are Ductal©, CeraCem, and Cor-Tuf. Ductal© and CeraCem were each developed in France over the past few

decades, while Cor-Tuf emerged more recently in the United States. A review of these UHPC products and their research data follows.

2.5.4.1 Ductal© technology

Ductal© is an ultra high performance fiber-reinforced concrete product originating from the efforts of three companies: LaFarge (construction materials manufacturer), Bouygues (civil engineering contractor), and Rhodia (chemical materials manufacturer), in response to the development of reactive powder concrete in the 1990's. The term "ductal" refers to the enhanced durability that is generated by a reduction in defects like micro-cracking and/or pore spaces (Acker and Behloul 2004). The standard mixes reflect the typical UHPC composition, with particle sizes ranging between 0.1 µm and 600 µm, but variations in fiber reinforcement exist. The fibers used may either be steel, an organic material, or a combination of the two.

The parent companies gathered research data from over twenty different laboratory facilities and universities testing their products. The results supported the enhancement of mechanical and durability behaviors expected. Indicators of the material's heightened properties are an average *w/c* ratio of 0.18, an average density of 2,450 kg/m^3, and a 2%–6% porosity (four to five times lower than that of normal concrete). The use of steel fibers (which demonstrate a tensile strength of 2,000 MPa and Young's modulus of 200,000 MPa) provides additional insight to the concrete strengths recorded. The research reports include ranges for the compressive strength, flexural strength, and fracture energy measured: 174–186 MPa, 25–39 MPa, and 20,000–30,000 J/m^2, respectively (Cavill 2005).

Acker and Behloul (2004) present the compressive and bending behaviors of Ductal©. Their graphical representations also compare the Ductal© stress-strain and

stress-displacement diagrams with those of ordinary concrete. The ductility apparent prior to reaching the peak bending stress is due to micro-cracking of the concrete (Acker and Behloul 2004). The formation of multiple small cracks provides the beams with greater support than if a central major crack were to develop.

Ductal© materials may or may not be thermally treated. In either case, the total concrete shrinkage is comparatively minimal; heat treatment simply expedites the process. With heat treatment, a concern need not exist with respect to the member's shrinkage after placement. A similar benefit occurs for creep. Heat treatment minimizes the creep coefficient to nearly 0.2, as opposed to approximately 0.8 without treatment.

2.5.4.2 CeraCem (formerly BSI)

CeraCem was developed by Eiffage, a contracting and consulting company based in France, in partnership with Sika Regional Technology. CeraCem is classified as an ultra high performance fiber-reinforced concrete, as well as a self-compacting concrete. CeraCem consists of three commercial premixes each of which applies to either the structural, aesthetic, or grouting and anchoring fields (Abdelrazig 2008). Property values reported by Eiffage for the structural premix (commonly called BFM-Millau) are listed in Table 2-6.

CeraCem was originally marketed as BSI (Béton Spécial Industriel), the name under which several engineering projects were carried out. The majority of its projects have been localized in France, the most prominent of which was the Millau viaduct toll gate constructed in 2004 and discussed later alongside other UHPC applications.

2.5.4.3 Cor-Tuf

Cor-Tuf was developed by the Geotechnical and Structural Laboratory (GSL) of the U.S. Army Corp of Engineers' Engineer Research and Development Center. It was

created with a fixed material composition to regulate the UHPC testing performed. In 2009, the ERDC published a detailed report on Cor-Tuf: *Laboratory Characterization of Cor-Tuf With and Without Steel Fibers*. The report is the primary literature available on the Cor-Tuf material and describes the ultra high performance concrete as a reactive powder concrete (RPC) with concrete cylinder strengths in the range of 190 to 244 MPa. It documents the results of six mechanical tests completed for both concrete with and without steel fibers, including hydrostatic compression, unconfined compression, triaxial compression, unconfined direct pull, uniaxial strain, and uniaxial strain/constant volume strain loading tests.

The triaxial compression tests performed characterize the brittle versus ductile behavior of concrete. A collection of the data from a total of twelve such tests is provided by the ERDC is graphical form. The principal stress difference versus axial strain graph compares six different confining pressures that range from 10 MPa to 300 MPa. Below a pressure of 100 MPa, strain softening is observed by a drop in the stress after reaching its peak. The 200 MPa and 300 MPa confining pressures however promoted strain-hardening and an increased growth in strength (Williams et al. 2009).

2.5.5 UHPC Codes and Regulations

Though ultra high performance concrete developed from normal concrete, their properties are too fundamentally different to group them together as a single material. Correspondingly, their regulations of their use must not be assumed to overlap with guidelines prepared for normal concrete or HPC to be recycled on UHPC's behalf. The next step toward generating a broader use of UHPC is establishing standards to which the material can be held. As the breadth of UHPC literature has expanded, civil engineering societies have begun organizing the findings and creating a foundation for

future codes. UHPC is still relatively young with respect to its material characterization, and accordingly, the completion of such regulatory codes will likely not occur before the material has sufficiently aged. To date though, societies in France and Japan have each published a set of recommendations, with similar work being conducted in other nations.

The first complete set of guidelines prepared on behalf of ultra high performance fiber-reinforced concrete was the French Association for Civil Engineering's (AFGC) *Interim Recommendations* of 2002. The recommendations classify UHPC as a cement-based product with a compressive strength in the range of 150 MPa to 250 MPa (approximately equivalent to 22 ksi to 36 ksi), and it elicits the use of steel fiber reinforcement "to achieve ductile behavior under tension and, if possible, to dispense with the need for passive (non-prestressed) reinforcement." AFGC's *Interim Recommendations* is divided into three sections: characterization, design and analysis, and durability of UHPFRC.

In *Part 1* the relationship between UHPFRC's characterization and the behavioral contribution of its fiber reinforcement is highlighted. Considered are the effects imposed on tensile strength and the concrete's geometry during placement. The diagram displayed in Figure 2-24 represents the elastic and post-cracking stages defining the tensile behavior of UHPFRC. The elastic stage is surpassed upon reaching of the cement's tensile strength (f_{tj}) and the transfer of strength to that of the composite structure. The document notes that the diagram is representative of the strain-hardening case.

*Part 1*of the *Interim Recommendations* also serves as a provision for laboratory testing, including instruction for compressive, direct tensile, and flexural tensile strength

tests, and for the routine checking of the concrete's design, mixing, and placement. The document emphasizes the usefulness of evaluating each batch of UHPFRC on an individual basis and provides property coefficients for use when they cannot be directly determined. Values defined are as follows:

- Static modulus of elasticity, 55 MPa
- Poisson's ratio, 0.2
- Thermal expansion coefficient, 1.1×10^{-5} m/m/°C
- Shrinkage, 55 μm/m
- Creep coefficient, 0.2 (with heat treatment) or 0.8 (without heat treatment)

Part 2 delves into the design and analysis of UHPFRC members and is largely based on the French BPEL and BAEL codes (which respectively address the limit state designs of prestressed concrete structures and reinforced concrete structures). Some excerpts are pulled directly from one of the previous codes, while others are slightly adapted to the UHPFRC material. The recommendations' third and final section, *Part 3*, evaluates potential threats (biological or chemical agents) to the concrete's sustainability and its potential to endure any such damage. Observations of early UHPFRC applications demonstrate the concrete's suitability to aggressive environments and structural longevity. Also, though not typically considered a trait of durability, the section addresses fire resistance and its connection to the material's bearing capacity.

The Japanese Society for Civil Engineers (JSCE) released its *Recommendations for Design and Construction of Ultra High Strength Fiber Reinforced Concrete Structures, Draft* in 2006. The recommendations classify UHPFRC by a compressive strength exceeding 150 MPa, similar to AFGC's guidelines, and a tensile strength greater than 5 MPa. JSCE specifically highlights two ways by which the document deviates from normal concrete standards. First, in reference to the tensile strength

apparent in UHPFRC without conventional steel reinforcement, methods for safety and serviceability evaluations are provided. The recommendations also limit the required durability testing and set the material's standard lifespan at 100 years (under typical environmental conditions) due to the enhanced density and its resultant durability.

2.5.6 Applications of Ultra High Performance Concrete

Structural materials are selected for use based on the evaluation of four primary characteristics: strength, workability, durability, and affordability (Tang 2004). As exemplified, UHPC excels in the areas of strength and durability, but its widespread employment has been inhibited by both its workability and affordability. Though the addition of superplasticizers lessens the constraint inherently placed upon workability (fluidity), it remains a challenge to readily adapt established construction methods to the more specialized practices required. This same needed specialization leaves the cost of UHPC above that of other comparable structural materials. The lack of widespread availability and increased cost encourage developers to seek new, advantageous applications for UHPC. Even given its relative youth with respect to research and development, UHPC has been successfully employed in a number of completed projects based on its benefits of high durability, high strength, and architectural aesthetics. Examples of these three aspects are subsequently discussed.

Introduced in the recap of UHPC's history, the earliest UHPC applications involved the use of the D.S.P. cement created in Denmark. The applications primarily focused on exploiting durability and pertained to protective structures and wear resistance. For instance, scoop feeders were built from UHPC for the cement mill of Aalborg, Denmark, and cavities caused by erosion in the Kinuza (Denmark) and Raul Leoni (Venezuela) dams were corrected with UHPC. The material performed well under testing devised to

qualify barrier materials and began employment in security structures such as vaults or ATMs worldwide (Buitelaar 2004). Its continued high performance has warranted its use against blast and impact loads and in the construction of larger protective structures. For example, the ERDC has worked in conjunction with the United States Gypsum Company to develop and supply armor material ready for military use (Roth et al. 2008).

Larger scale applications have included the construction of pedestrian and traffic bridges, as well as a runway expansion at the Haneda Airport (Tokyo, Japan). The more common bridge designs consist of precast and prestressed UHPC beams and girders. Examples of such include the Sherbrooke footbridge constructed in 1997 (the first prestressed hybrid bridge) and the Sakata Mirai footbridge constructed in 2002. One of the most documented bridge applications has been the Gärtnerplatz Bridge in Kassel, Germany. The bridge is a hybrid of UHPC and structural steel, the first of its kind, and consists of six spans totaling a distance of 132 meters.

UHPC is well suited for bridge construction due to its combination of inherent high strength and use of fiber reinforcement. Its increase in strength over normal concrete allows for thinner and ultimately lighter precast elements. Another facet of research has focused on designing new beam and girder specifications to optimize UHPC's particular attributes. The steel fiber reinforcement, on the other hand, is instrumental in replacing mild steel. The improved flexural strength due to the fibers, especially in tension, dually improves beam shear capacity. The capacity is increased enough to void the need of mild reinforcement, and without any stirrups or other passive steel, construction costs may be reduced (Acker and Behloul 2004).

An example of the architectural use of UHPC is the toll gate constructed for the Millau viaduct in France. The toll also serves to demonstrate use of the CeraCem product. Completed in 2004, its arched roof consists of 53 concrete segments joined longitudinally with prestressing rods and spans a total of 98 meters. UHPC's properties support a reduction in the structure's depth, without which the implementation of concrete would likely not have been feasible. Utilizing thin members trims the overall weight of the structure (beneficial for the structural support) and produces an aesthetically pleasing design.

2.6 Summary

This chapter prepared the literature review for the structural and dynamic analysis of normal strength and ultra high performance concrete columns subjected to severe blast and impact loads. Section 2.2 was devoted to processing an element's response to dynamic loads and modeling the pressure exerted from explosives. Section 2.3 summarized the modes of failure and material behavior of reinforced concrete columns. The primary focus of the development of plastic hinges in reinforced concrete columns and the material of ultra high performance concrete were discussed in depth in sections 2.4 and 2.5, respectively.

Table 2-1. Sample of UHPC mix proportions. [Adapted from Habel, K. and Gauvreau, P. 2008. Response to ultra-high performance fiber reinforced concrete (UHPFRC) to impact and static loading. (Page 939, Table 1) Cement & Concrete Composites 30.]

Constituent	Type	Weight (kg/m^3)
Cement	Portland cement	967
Silica fume	White, specific surface: 15-18 m^2/g	251
Silica sand	Size < 0.5 mm	675
Steel fibers	Straight (length/diameter: 10 mm/0.2 mm)	430
Superplasticizer	Polycarboxylate	35
Water		244

Table 2-2. Percent replacement of Portland cement with silica fume. [Adapted from Jayakumar, K. 2004. Role of Silica fume Concrete in Concrete Technology. (Page 169, Table 3). Proceedings of the International Symposium on Ultra High Performance Concrete. Kassel, Germany.]

Strengths	0.0%	2.5%	5.0%	7.5%	10.0%	12.5%
Compressive @ 90 days (MPa)	72.75	74.50	79.75	89.25	81.50	76.25
Split tensile @ 28 days (MPa)	4.46	4.52	4.65	5.47	4.71	4.52
Flexural @ 28 days (MPa)	6.42	6.44	6.90	7.63	6.51	6.36
Young's modulus @ 28 days (GPa)	37.17	38.26	38.65	43.73	39.13	38.41

Table 2-3. Static mechanical tests with increasing volume of steel fibers. [Adapted from Rong, Z. et al. 2009. Dynamic compression behavior of ultra-high performance cement based composites. (Page 517, Table 2). International Journal of Impact Engineering 37.]

UHPC type	Compressive strength (MPa)	Peak value of strain (x 10^{-3})	Elastic modulus (GPa)	Toughness index		
				η_{c5}	η_{c10}	η_{c30}
0% fiber	143	2.817	54.7	2.43	2.43	2.43
3% fiber	186	3.857	57.3	53.59	5.08	5.57
4% fiber	204	4.165	57.9	4.57	6.32	7.39

Table 2-4. Optimized UPHC mix proportions. [Adapted from Park, J.J. et al. 2008. Influence on the Ingredients of the Compressive Strength of UHPC as a Fundamental Study to Optimize the Mixing Proportion. (Page 111, Figure 10). Proceedings of the Second International Symposium on Ultra High Performance Concrete, Kassel, Germany.]

Mixutre component	Proportion
Sand	1.1
Cement	1.0
Filling Powder	0.3
Water	0.25
Silica Fume	0.25
Superplasticizer	0.016
Steel fiber (% of volume)	2.0

Table 2-5. Varied packing densities. [Adapted from Teichmann, T. and Schmidt, M. 2004. Influence of the packing density of fine particles on structure, strength and durability of UHPC. (Page 318, Table 3). Proceedings of the International Symposium on Ultra High Performance Concrete. Kassel, Germany.]

Property		NC C35	HPC C100	UHPC C200
Total porosity	(vol. %)	15.0	8.3	6.0
Capillary pores	(vol. %)	8.3	5.2	1.5

Table 2-6. Summary of CeraCem (structural premix) properties. [Adapted from Abdelrazig, B. 2008. Properties & Applications of CeraCem Ultra High Performance Self Compacting Concrete. (Page 220, Table 1). Proceedings of the International Conference on Construction and Building Technology. Kuala Lumpur, Malaysia.]

Property	Measured Value
Compressive strength @ 2 days	122 MPa
Compressive strength @ 28 days	199 MPa
3-point flexural strength @ 28 days	30 MPa
4-point flexural strength @ 28 days	29 MPa
Tensile strength @ 28 days	8 MPa
Modulus of elasticity @ 28 days	71 GPa
Total shrinkage @ 1 year	725 microstrain
Total shrinkage (with SRA) @ 1 year	<500 microstrain

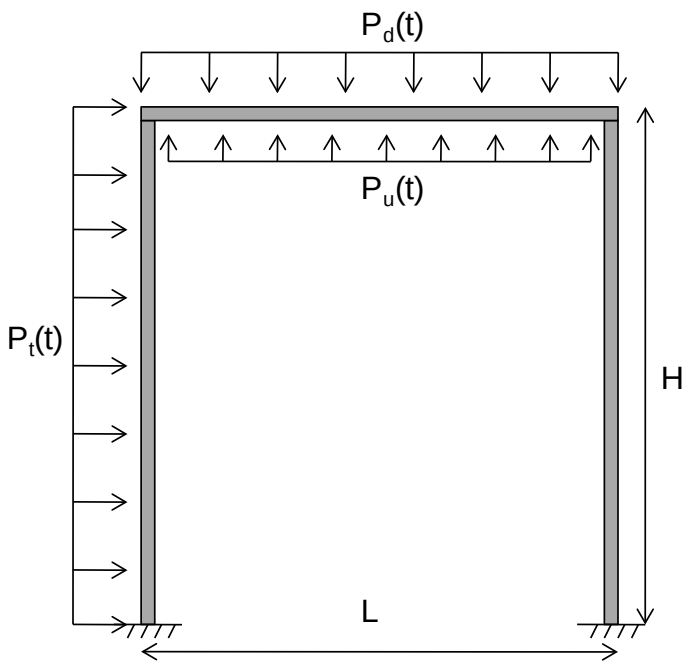

Figure 2-1. Example of frame loading. [Adapted from Tran, B.A. 2009. Effect of short-duration-high-impulse variable axial and transverse loads on reinforced concrete column. MS thesis. (Page 48, Figure 3-1). University of Florida, Gainesville, Florida.]

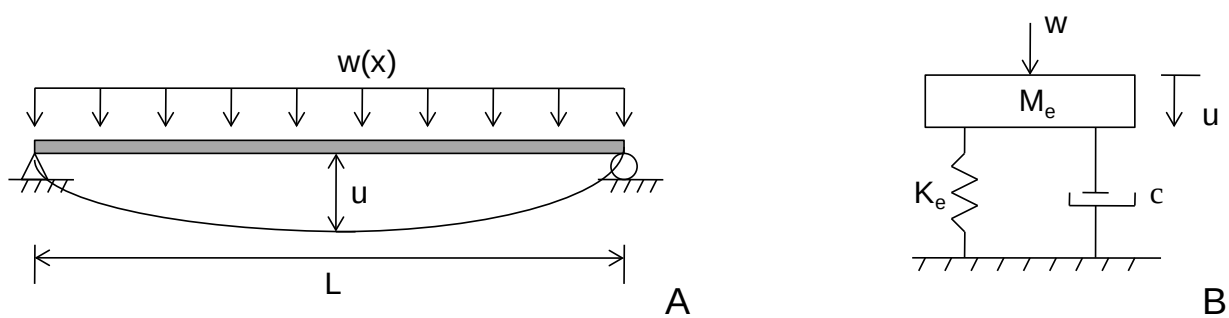

Figure 2-2. Equivalent systems. A) Loaded beam element. B) Equivalent SDOF system. [Adapted from Morency, D. 2010. Large deflection behavior effect in reinforced concrete columns under severe dynamic short duration load. MS thesis. (Page 79, Figure 2-3). University of Florida, Gainesville, Florida.]

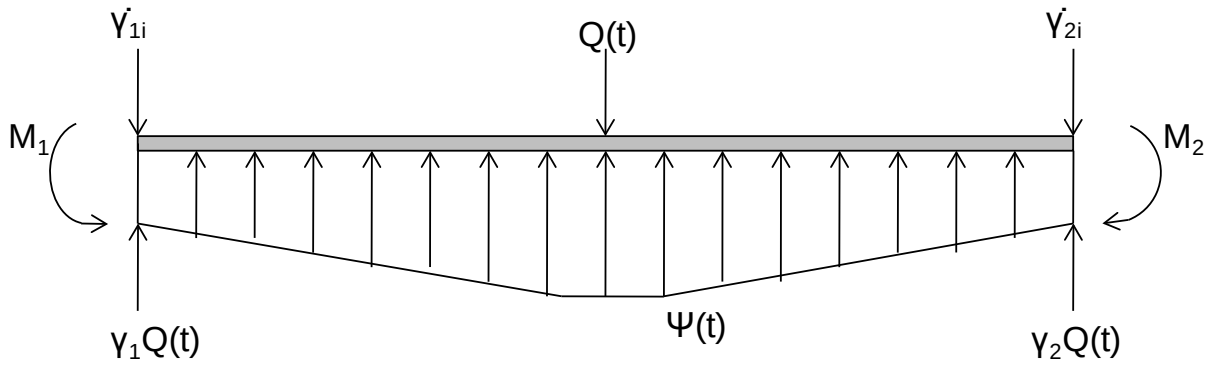

Figure 2-3. Reaction force schematic for beam with arbitrary boundary conditions. [Adapted from Krauthammer, T. and Shahriar, S. 1988. A Computational Method for Evaluating Modular Prefabricated Structural Element for Rapid Construction of Facilities, Barriers, and Revetments to Resist Modern Conventional Weapons Effects. ESL-TR-87-60. (Page 122, Figure 44). Engineering & Services Laboratory Air Force Engineering & Services Center, Florida.]

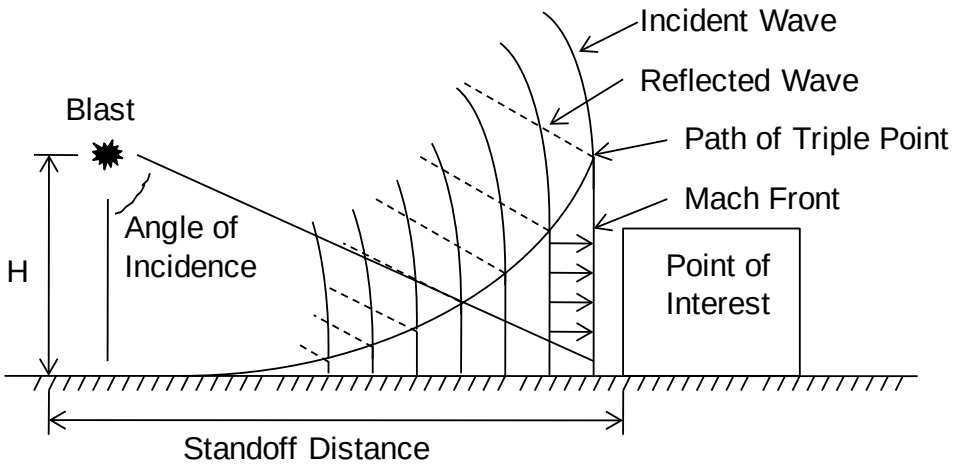

Figure 2-4. Free-air blast. [Adapted from Unified Facilities Criteria. 2008. Structures to Resist the Effects of Accidental Explosions. UFC 3-340-02. (Page 87, Figure 2-12) U.S. Department of Defense, Washington D.C.]

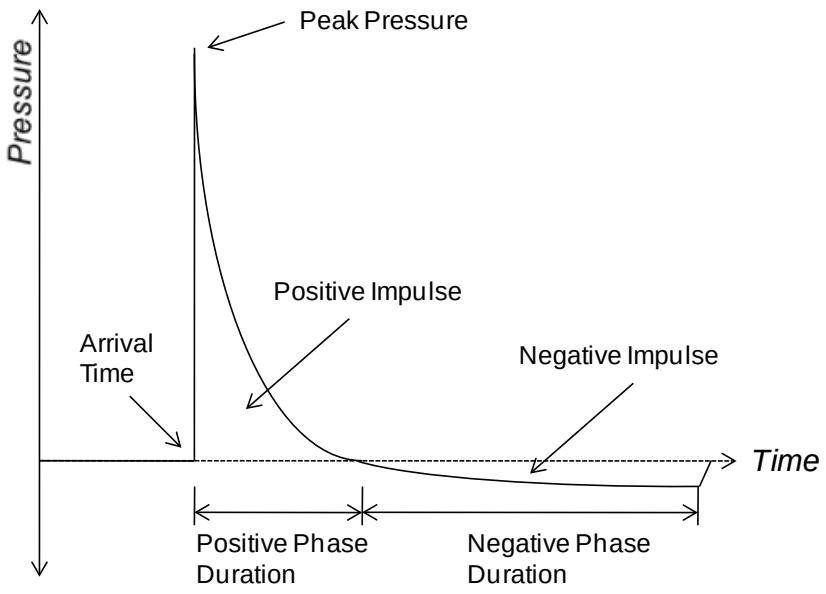

Figure 2-5. Pressure-time history for an idealized free-air blast wave.

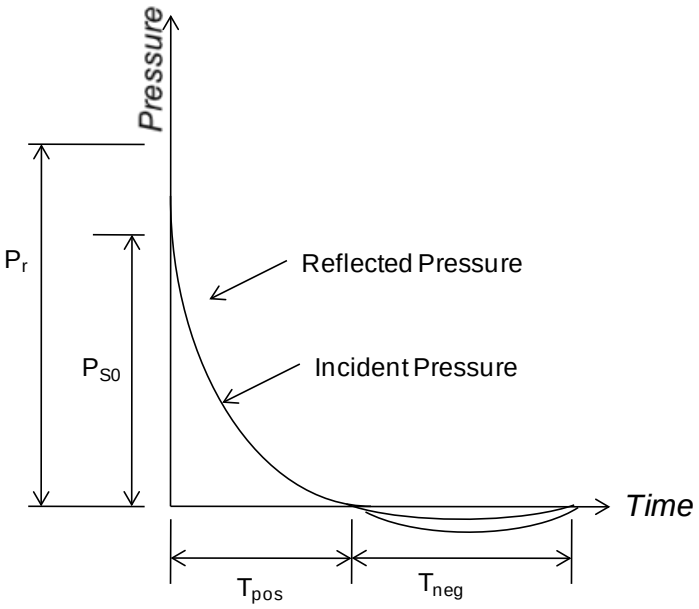

Figure 2-6. Simplified pressure-time history.

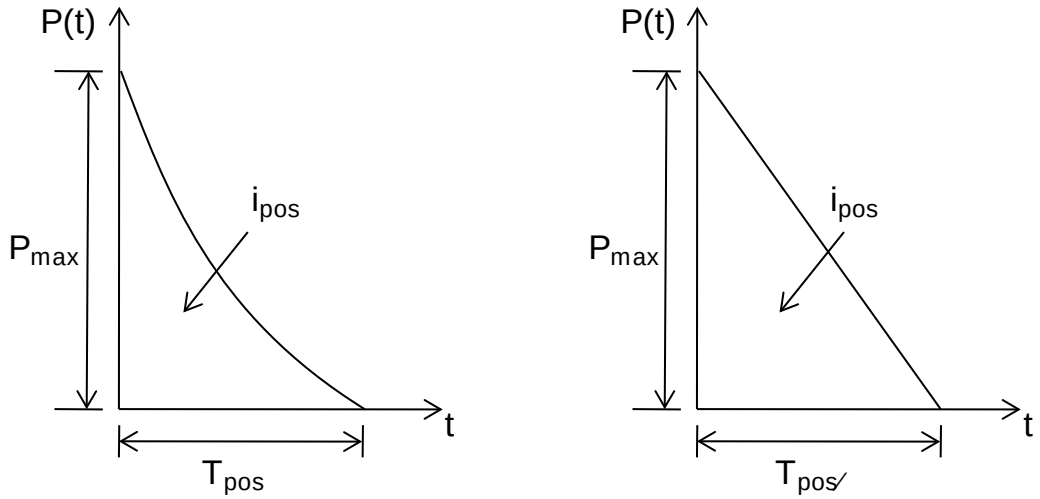

Figure 2-7. Equivalent triangular pressure-time history.

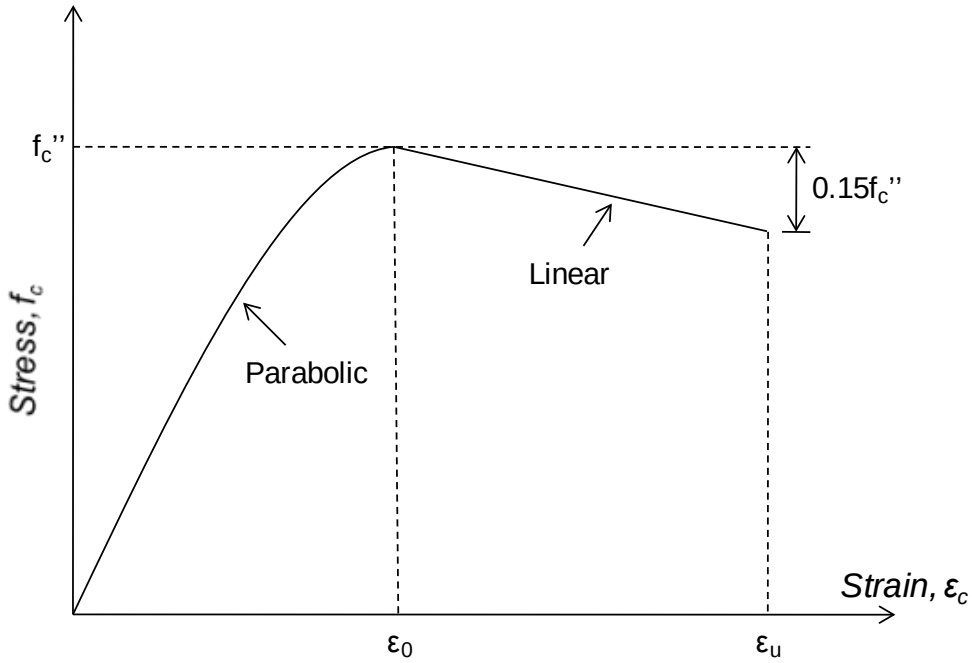

Figure 2-8. Ideal concrete stress-strain curve for uniaxial compression.

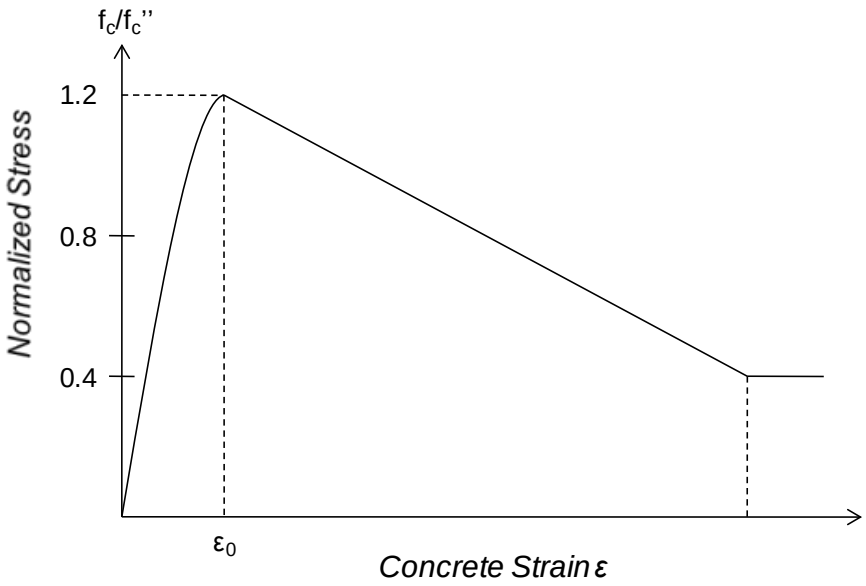

Figure 2-9. Confined concrete stress-strain curve. [Adapted from Krauthammer, T. and Shahriar, S. 1988. A Computational Method for Evaluating Modular Prefabricated Structural Element for Rapid Construction of Facilities, Barriers, and Revetments to Resist Modern Conventional Weapons Effects. ESL-TR-87-60. (Page11, Figure 3). Engineering & Services Laboratory Air Force Engineering & Services Center, Florida.]

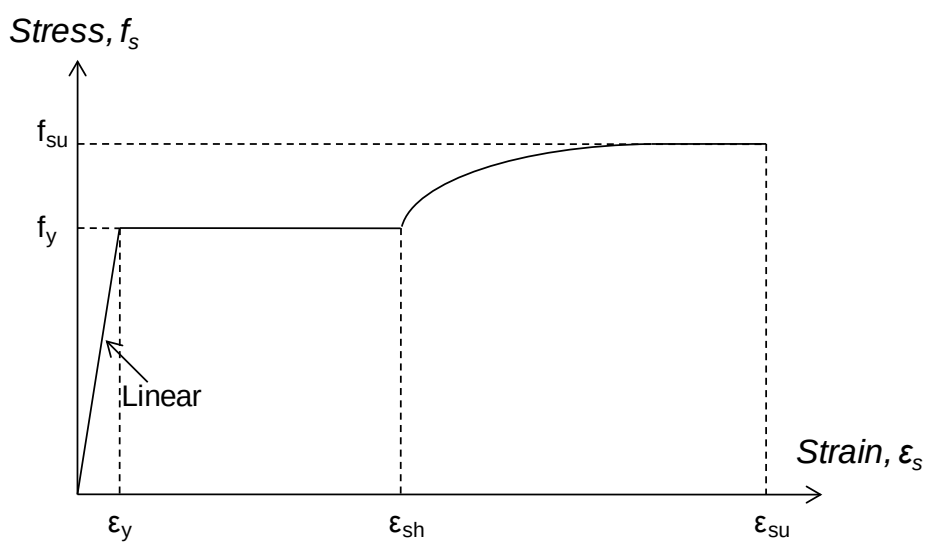

Figure 2-10. Steel reinforcement stress-strain curve.

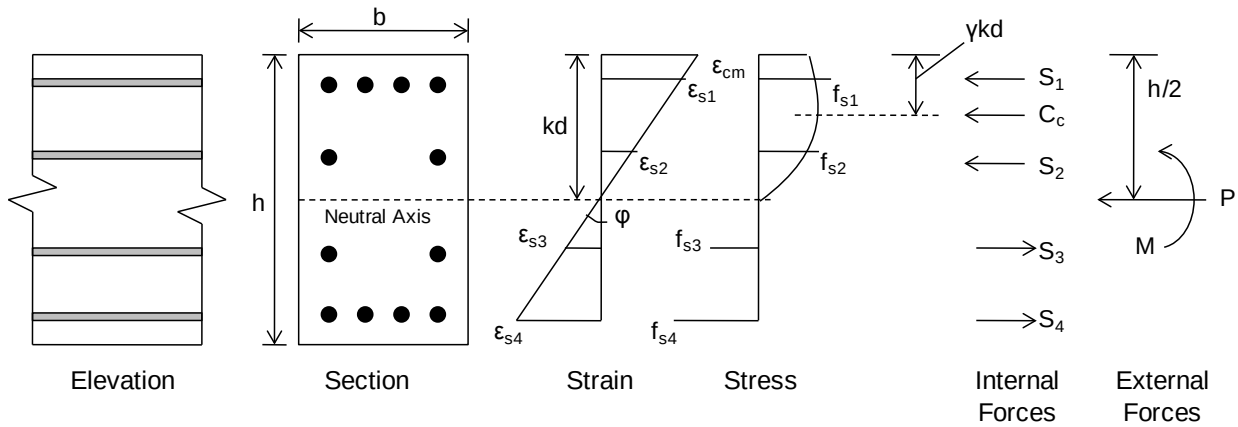

Figure 2-11. Concrete section with strain, stress, and force distributions. [Adapted from Park, R. and Paulay, T. 1975. Reinforced Concrete Structures. (Page 201, Figure 6.5). John Wiley & Sons Inc., New York, New York.]

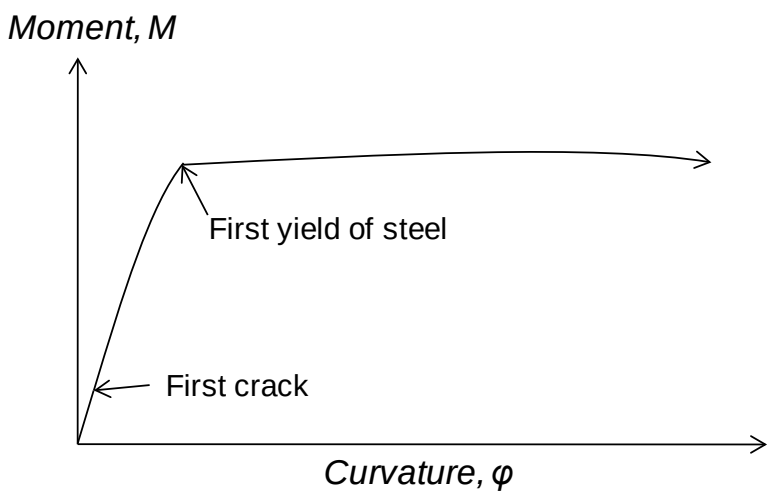

Figure 2-12. Typical moment-curvature diagram. [Adapted from Park, R. and Paulay, T. 1975. Reinforced Concrete Structures. (Page 198, Figure 6.3). John Wiley & Sons Inc., New York, New York.]

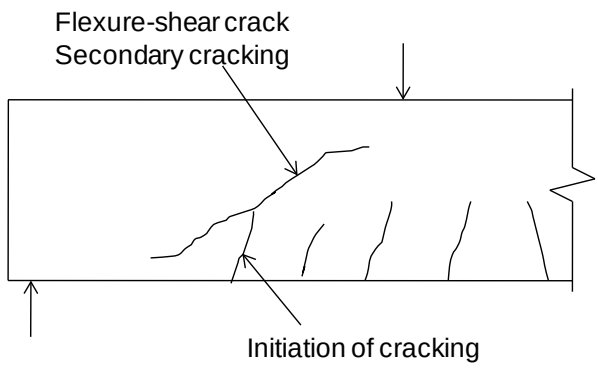

Figure 2-13. Flexure-shear cracking pattern. [Adapted from Krauthammer, T. and Shahriar, S. 1988. A Computational Method for Evaluating Modular Prefabricated Structural Element for Rapid Construction of Facilities, Barriers, and Revetments to Resist Modern Conventional Weapons Effects. ESL-TR-87-60. (Page 27, Figure 8). Engineering & Services Laboratory Air Force Engineering & Services Center, Florida.]

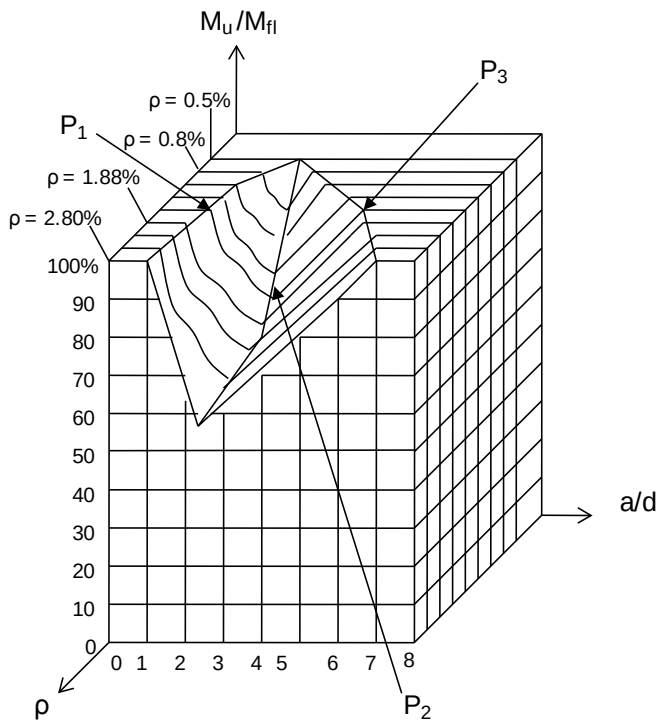

Figure 2-14. Influence of shear model – without web reinforcement. [Adapted from Krauthammer, T. and Shahriar, S. 1988. A Computational Method for Evaluating Modular Prefabricated Structural Element for Rapid Construction of Facilities, Barriers, and Revetments to Resist Modern Conventional Weapons Effects. ESL-TR-87-60. (Page 35, Figure 11). Engineering & Services Laboratory Air Force Engineering & Services Center, Florida.]

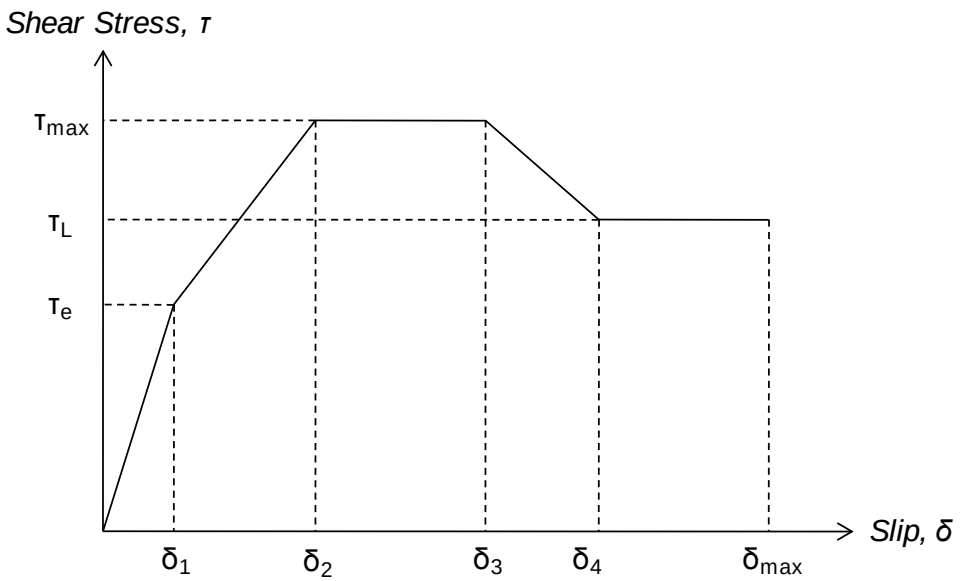

Figure 2-15. Relationship between direct shear stress and shear slip. [Adapted from Tran, B.A. 2009. Effect of short-duration-high-impulse variable axial and transverse loads on reinforced concrete column. M.S. thesis. (Page 34, Figure 2-13). University of Florida, Gainesville, Florida.]

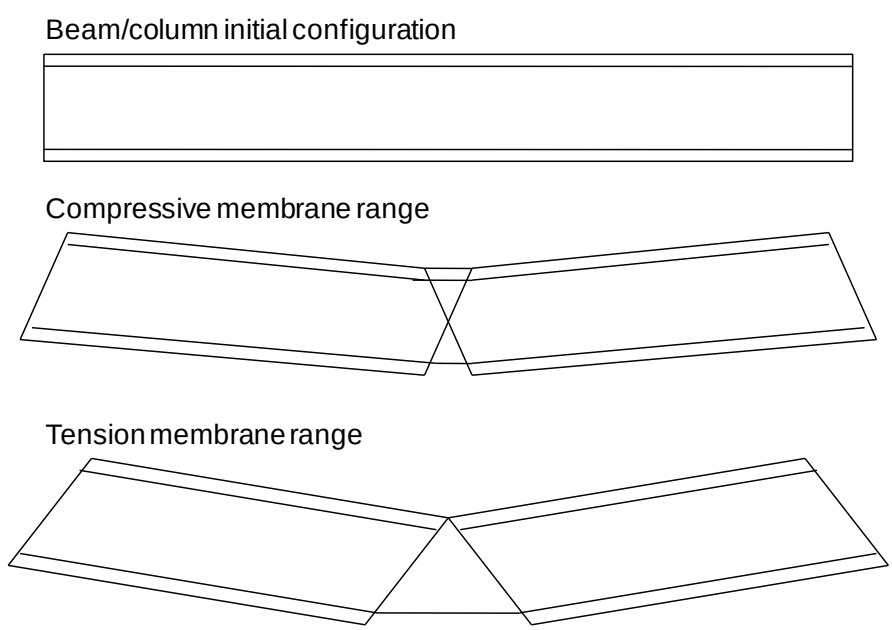

Figure 2-16. Compression and tension membrane behavior. [Adapted from Morency, D. 2010. Large deflection behavior effect in reinforced concrete columns under severe dynamic short duration load. M.S. thesis. (Page 94, Figure 2-21). University of Florida, Gainesville, Florida.]

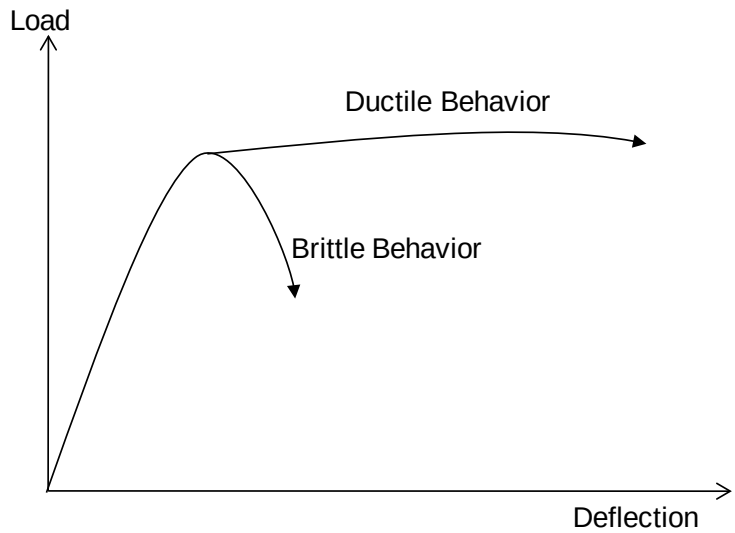

Figure 2-17. Ductile and brittle concrete behavior.

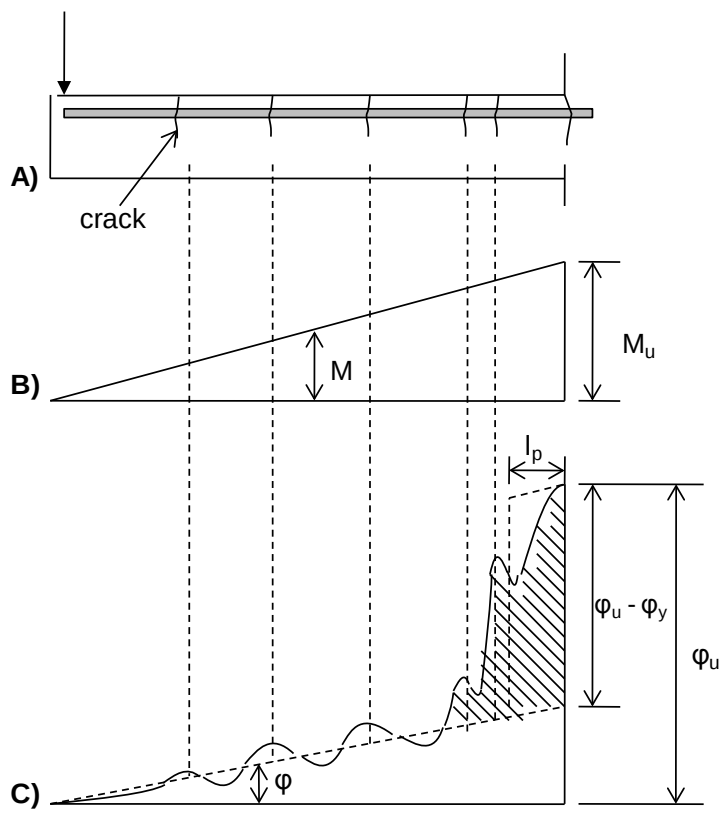

Figure 2-18. Curvature along a beam at ultimate moment. [Adapted from Park, R. and Paulay, T. 1975. Reinforced Concrete Structures. (Page 243, Figure 6.26). John Wiley & Sons Inc., New York, New York.]

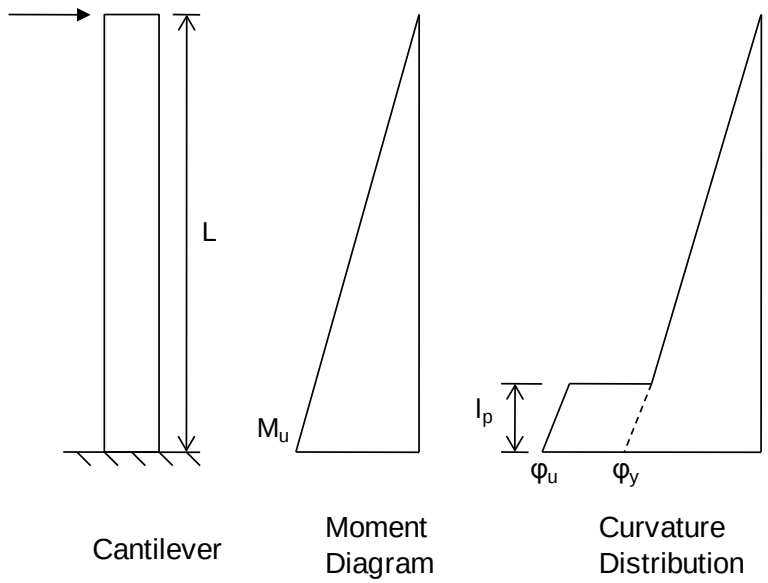

Figure 2-19. Plastic hinge of a cantilever column. [Adapted from Park, R. and Paulay, T. 1975. Reinforced Concrete Structures. (Page 245, Figure 6.28). John Wiley & Sons Inc., New York, New York.]

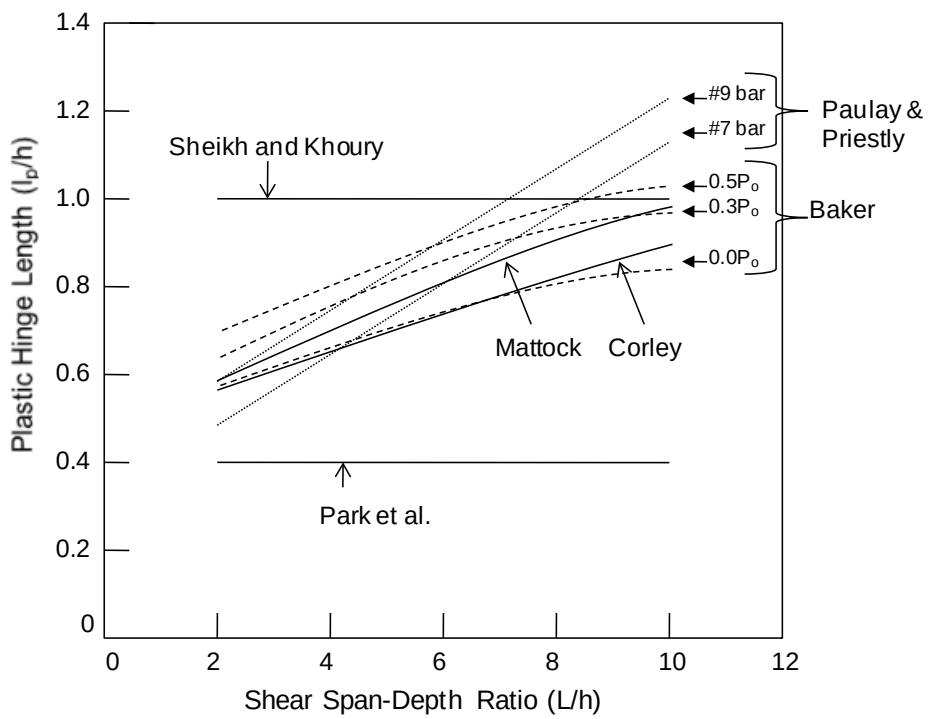

Figure 2-20. Comparison of plastic hinge length expressions. [Adapted from Bae, S. and Bayrak, O. 2008. Plastic Hinge Length of Reinforced Concrete Columns. (Page 292, Figure 2). ACI Structural Journal 105 (3).]

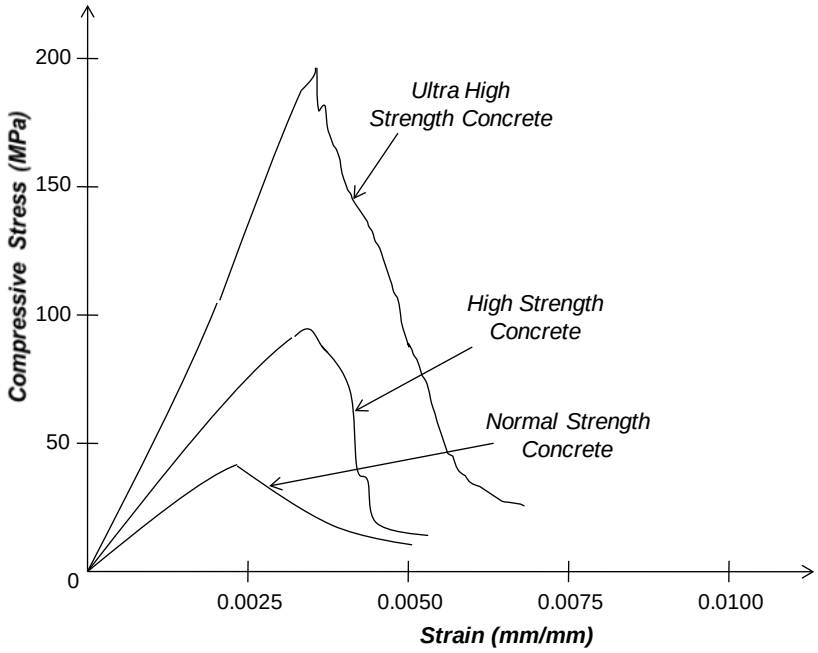

Figure 2-21. Increasing brittleness with strength. [Adapted from Shah, S.P. and Weiss, W.J. 1998. Ultra High Performance Concrete: A Look to the Future. (Figure 4). ACI Special Proceedings from the Paul Zia Symposium, Atlanta, Georgia.]

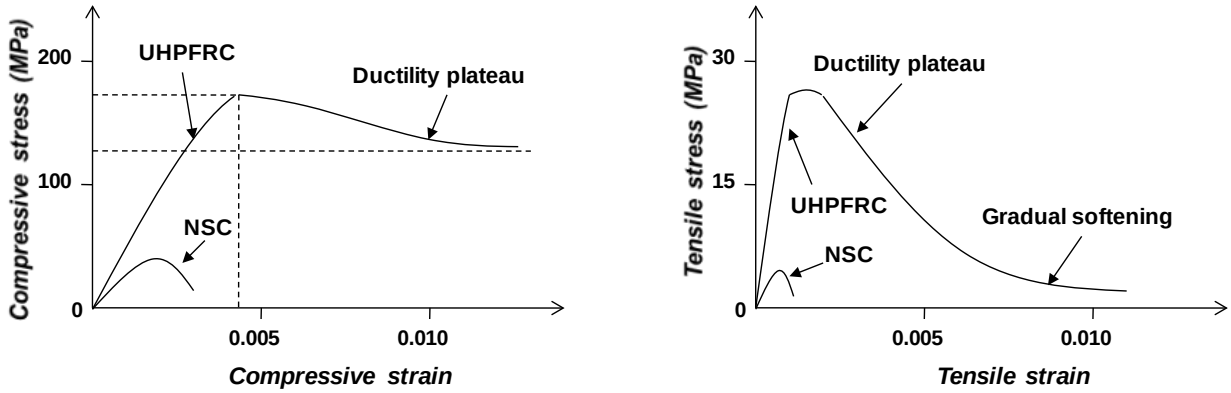

Figure 2-22. Stress-strain diagrams – normal concrete vs. UHPFRC. [Adapted from Wu, C. et al. 2009. Blast testing of ultra-high performance fibre and FRP-retrofitted concrete slabs. (Page 2061, Figure 1). Engineering Structures 31.]

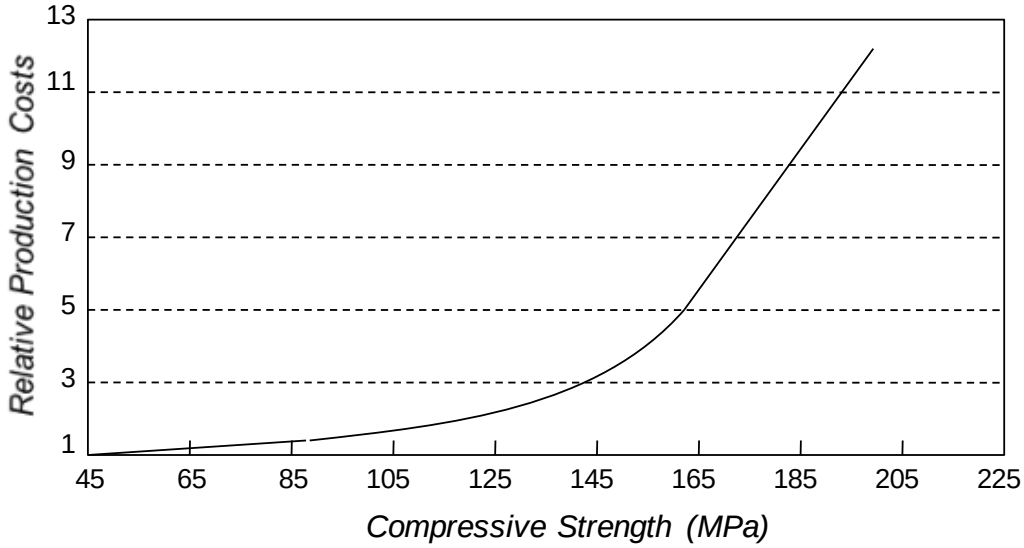

Figure 2-23. Production cost with respect to compressive strength. [Adapted from Markeset, G. 2002. Ultra High Performance Concrete is Ideal for Protective Structures. High-Performance Concrete. (Page 137, Figure 9). Performance and Quality of Concrete Structures Proceedings, Third International Conference.]

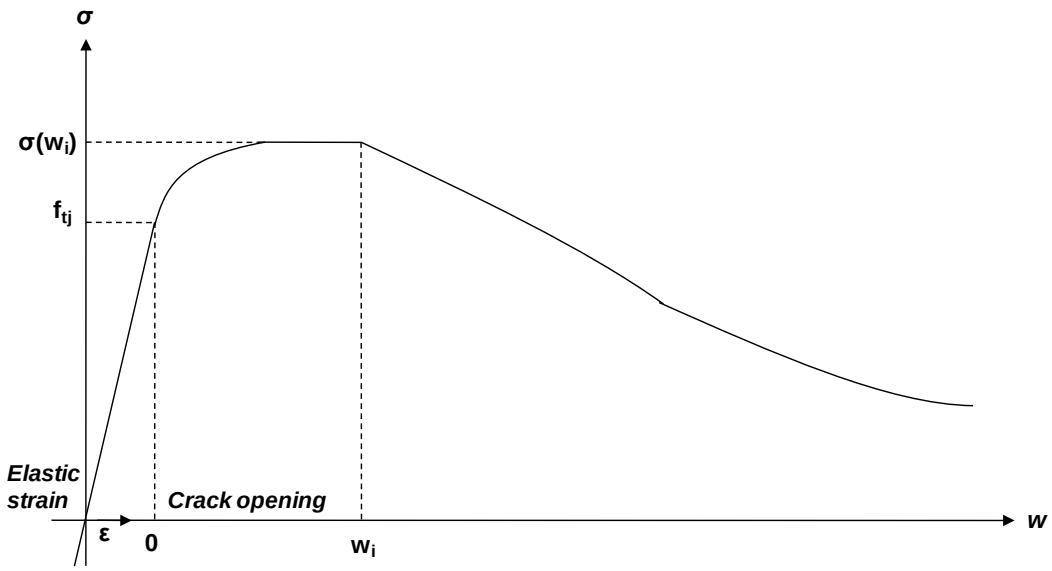

Figure 2-24. Tensile constitutive law of UHPFRC. [Adapted from Association Française de Génie Civil 2002. Bétons fibrés à ultra-hautes performances – Recommandations provisoires. (Page 17, Figure 1.2). Association Française de Génie Civil. France.]

CHAPTER 3
METHODOLOGY

3.1 Overview

The focus of this study is to examine the Dynamic Structural Analysis Suite's ability to properly model the formation of plastic hinges in concrete columns. The engineering materials of interest include both normal strength and ultra high performance concrete, and by realistically modeling their hinge and curvature behavior advanced insight may be gathered with respect to the failure mechanisms of such concrete systems. Though previous studies have sought to analyze plastic hinging in NSC columns, much of the UHPC focus has been on developing its basic functionality. The brevity of analysis available is therefore expanded by this effort, and whether UHPC exhibits similar plastic behavior to NSC is demonstrated.

This chapter elaborates on the process followed to complete the study. Section 3.2 measures DSAS V3.2.1's (Astarlioglu 2008) capabilities in terms of monitoring the hinge formation over time and describes the program adjustments made to more acutely account for the mechanism. Section 3.3 establishes the Feldman and Siess (1958) experimental beams used to verify DSAS's compatibility with material input and behavioral analyses, while section 3.4 overviews the employment of the finite element code ABAQUS/Explicit V6.10 (SIMULIA 2010) to further validate the DSAS results. Finally, section 3.5 prepares the parametric study, and section 3.6 summarizes of the implemented methodology and the prominent analytical issues to be discussed.

3.2 Plastic Hinge Development in DSAS

DSAS performs a simplified dynamic analysis of concrete columns subjected to severe and short duration loading. Aligned with the methods described in sections 2.2

and 2.3, the program considers the combined incurrence of axial and transverse loads as well as the effects of large deformation behavior on representative single-degree-of-freedom systems. Standard data for output includes the indication of flexural and/or shear failure, the deformation-time response at the critical point of interest, and the correspondent pressure-impulse diagram. Though the basic output provides the maximum response at the critical point via a SDOF analysis, the program is also capable of tracking the relationship between load and deflection of designated elements along the column's length. The record of a column's deformation ultimately allows for the rotation and curvature along its length to be monitored, and an evaluation of the displacement, rotation, and curvature output provided by the originating DSAS program follows.

To explore the ideas outlined and analyze DSAS's abilities, a standard, simply-supported reinforced concrete test beam (similar to Beam-1C discussed in section 3.3) is subjected to a varying point load at its midspan. The moment-curvature relationship of the NSC beam is contingent upon its cross-sectional properties and is provided in Figure 3-1. Dependent on this relationship, the load-deflection curve of Figure 3-2 is generated by DSAS. This curve is relative to the beam's critical location of maximum response, i.e. the point at midspan. For each data point on the load-deflection curve, DSAS dually records the displacement at nodes along the beam's span and thereby enables the creation of a deformed beam schematic. DSAS assumes the size of the elements between nodes to be half the beam's depth (*h*). With the motivation to limit and thereby expedite calculations, the fewest number of nodes and elements that can accurately account for the structural member's shape is desired. The appropriateness of

using 0.5*h* as the approximate elemental length is to be determined through a later comparison with a finer mesh.

Since the test beam's critical location corresponds to midspan, an element that expands 0.5*h* to either of its sides exists and is taken to be the plastic hinge, for a total plastic hinge length of *h*. The remainder of the beam is divided into equally sized elements of approximately 0.5*h* (a whole number of elements is established). Note that for this particular beam case, the total number of nodes, including one mid-hinge at midspan, sums to nineteen. Each node represents a point at which displacement and rotation values are reported. Although the curvature is not directly provided through DSAS, a simple calculation is performed based on the rotation change per element length.

Five points along the load-deflection curve of Figure 3-2 are highlighted and correspond to the beam's 'tracked' points. Figures 3-3 through 3-5 respectively display the deformation, rotation, and curvature across the beam span per the five designated points of Figure 3-2. The beam's shape becomes more triangular with the growth of the midspan displacement as expected, and a similar trend is observed through the sharpening of the rotation curve's slope across the plastic hinge element. Regarding Figure 3-5, the curvature is calculated as the change in curvature per element and is therefore specified at elemental midpoints. Introduced in the literature review, the curvature across a plastic hinge is theoretically idealized as constant and may be recognized by a drop to or below yield on either of its sides. From the moment-curvature relationship, the yield curvature for the beam case is approximately 0.0003 in^{-1}. The yield curvature is marked by a dotted line in Figure 3-5, and the chart demonstrates that

the yield condition is exceeded outside of the hinge element. This observation indicates the need to reevaluate the DSAS programming for hinge generation.

Given the 0.5*h* (6 inch) length of each element, the beam meshing could plausibly be further refined. It is logical that a more defined picture would be found by refining the mesh, but doing so would also increase the computational cost. For comparison, the experimental setup was run via DSAS for a nodal count of fifty-one. The alternate DSAS configuration adjusts the elemental lengths to conform to a specified number of elements and does not account for a designated hinge element. As completed for the previous mesh density, Figure 3-6 shows the beam's load-deflection relationship, while Figures 3-7 through 3-9 display the deflected shapes, rotations, and curvatures across the beam span. Due to the increase in the number of elements, Figure 3-10 is provided to show a zoomed view of the curvature. Figure 3-10 is intended to emphasize the yield curvature and more clearly illustrate the plastic hinge development.

Contrasting the two beam cases highlights the effect of increasing the number of elements along the beam. Figure 3-5 demonstrates that the concrete length surpassing the yield curvature increases as the midspan deflection increases and that the inferred hinge would exceed its length *h*. The hinge length estimated for the first beam case from the curvature output is on the order of 30 inches. This approximation is considerably rough however due to the elements themselves being large and the curvature points distantly spread apart. To focus on the second case depicted in Figures 3-9 and 3-10, the yielded area fluctuates as the midspan deformation grows, and the ultimate hinge length is approximated at 10 inches. It is clear that the number of elements present affects the clarity and insight on the beam behavior.

The second beam case (51 nodes) illustrates the need to implement a properly sized plastic hinge element in order to obtain a realistic ultimate curvature. The curvature across a hinge ought to be roughly constant, and as the critical section's element decreases in size, the rotation change across it becomes too drastic. The ultimate curvature from Figure 3-1 is approximately 0.028 in^{-1}, and given that the same moment-curvature relationship applies to the two cases, the ultimate curvature should not be exceeded as it is in Figure 3-9. A discussion on the calculation of a satisfactory plastic hinge length and the corresponding DSAS modifications made follows.

To determine the plastic hinge length typical of reinforced concrete beam-columns, the equations presented in the literature review are employed. Table 3-1 presents the proposed hinge length equations and resultant calculations for the test beam. Included are the expressions issued by Corley, Mattock, Sawyer, Paulay and Priestly, and Sheikh and Khoury (Bae and Bayrak 2008). The Bae and Bayrak (2008) expression is omitted because of its minimal estimate without the presence of a known axial load. Due to a number of studies relating hinge length to either beam height or tension steel depth, a hinge length dependent on effective depth is additionally considered. For columns, the confined concrete area is the area providing primary support against the severe loading inherent of blasts or impacts. Therefore, this effective depth of resistance is understood as the 'true' column depth. The assessment of the two DSAS cases and their comparison with the Table 3-1 expressions indicates that the effective depth equation may be a reasonable representation of hinge length. Though Corley and Mattock's expressions equate to similar values for the length, the discernable difficulty in calculating the *z* parameter (the distance from critical point to contraflexure) per

combination of boundary and loading conditions elicits a desire for simplified calculations. The effective depth provides the wanted, and a comparable result, for a decreased computational cost.

The effective depth equation is therefore chosen as the modified DSAS hinge length to better represent the concrete's behavior. To implement the derivation and use of this value, the algorithm that establishes the elemental lengths used by DSAS is slightly adjusted. Because the critical region(s) from which the plastic hinge(s) spreads is based on user-defined boundary conditions, the full algorithm considers each boundary pairing (simple-fixed, free-fixed, etc.) separately. For each boundary set of the original program, an element the length of the beam-column's depth (*h*) is centered on the critical section, whereas for the modified algorithm, an element the size of the effective depth is substituted at the critical section. The elemental length outside of the hinge region is also adjusted between the original and modified algorithms. Although the length remains initially set at 0.5*h*, it is made an adaptable parameter in order to ease the refinement process. It appears that the increase in nodes only supplemented the adherence to yield curvature outside of the hinge region for the last points on the load-deflection curve, and the larger element sizes are thereby similarly applicable.

3.3 Experimental Validation Case

To standardize the column study, beams experimented upon by Feldman and Siess (1958) are examined. The beams marked as "1-c" and "1-h" by Feldman and Siess are subsequently referred to as Beam-1C and Beam-1H. The verification of Beam-1C and Beam-1H's behaviors offers a basis for the parametric study's constitutive material models. The documented Beam-1C case is also run to configure the agreement between the DSAS analysis and the use of the finite element code

ABAQUS. Work has previously been completed to model the Feldman and Siess beams via DSAS for comparison with the experimental output (Tran 2009; Morency 2010), but this current effort confirms the latest version's compatibility and continues on to extract the beams' curvature data from DSAS.

The geometry and experimental setup for the Feldman and Siess beams are diagrammed in Figures 3-11 and 3-12, and their concrete and reinforcing steel material properties are detailed in Table 3-2. The measurements and properties of beams 1C and 1H are drawn from Table 2 of Feldman and Siess (1958). The steel layers measure 1.5 and 10 inches from the top of the beam, while the open stirrups of Beam-1C and the closed stirrups of Beam-1H maintain approximately 0.75 inches of cover. For the material properties not expressly provided, the model employs assumed standard values in DSAS such as an ultimate steel strength of 90,000 psi. An important item to note is the beams' increased depth at midspan, a column stub upon which the point load is exerted. At its current status DSAS does not allot for a varying depth along a member's span, and the results must be considered as missing the effects of the 6 inch by 12 inch column stub.

Aside from the material, boundary, and loading input, DSAS also requires the selection of beam behavioral effects, including diagonal shear, compression buckling, and strain rate. Table 3-3 compares how each of these considerations, when acting alone, affects the peak deformations of the two beams and indicates whether failure occurs. Noting Beam-1C's maximum deflection of 3.0 inches during the experiment, it is evident that diagonal shear does not play a significant role in its case while strain rate does. Beam-1H on the other hand experimentally peaked at 8.9 inches, and as

demonstrated in Table 3-3, diagonal shear is deemed to work in conjunction with the estimated strain rate.

As Figure 3-11 depicts, the beams experience a varying point load at midspan. The loadings for beams 1C and 1H, severe and short in duration, are plotted in Figures 3-13 and 3-14, respectively. Due to their impulsive nature, the application of dynamic increase factors (DIFs) to the material strengths is supported. Feldman and Siess report approximated initial strain rates in their Table 4, upon which values for the DIFs may be based; however, the internal DSAS estimation results in alternate strain rate and DIF values. Table 3-4 compares the use of either reference. The employed DIFs derive from the consideration of both strain rate determinations and are listed in Table 3-5.

The results of the Feldman and Siess investigation are detailed in Table 3-6 and compared against those of DSAS for Beam-1C and Beam-1H. Both DSAS cases account for strain rate effects, while only Beam-1H accounts for diagonal shear. Table 3-6 denotes compatibility between the experimental and analytical output and establishes DSAS's functionality. As configured, the differences between the reported maximum response of beams 1C and 1H are 0.3% and 2.3%, respectively. Also considering DSAS's ability to capture the elastic-plastic behavior of concrete beams, the difference in the permanent deformations for Beam-1C is 6.8% while that for Beam-1H is 5.6%. Although several assumptions are built into the models, including the dependence on Feldman and Siess's static tests to detail the material strengths and the variances in the ultimate steel strength and column stub, the magnitudes and ranges of deflections reported are within engineering reason and appropriate.

3.4 Finite Element Analysis

The DSAS programming is tested and validated against the finite element software ABAQUS to certify their correlation. Finite element analysis (FEA) provides a thoroughly detailed look at a structural system's operation, including and not limited to deformation and stress distribution over time. FEA is based on approximating solutions to the partial differential equations relevant of material behavior, and its accuracy can be as great as that of the data put into it (i.e. the ability to incorporate nonlinearity depends on how well the phenomena is understood). Although a finite element solution can be exceptionally refined and complex, its use incurs a cost in computational time, and this is where the expediency of DSAS becomes largely beneficial. This section details the ABAQUS validation of the Feldman and Siess Beam-1C, including the standard assumptions and practices of the coding system, in order to establish the material models employed for the parametric study's columns.

Within the ABAQUS input file of Beam-1C, the beam geometry adheres to Figure 3-11. The simple supports are configured as rollers, and the midspan plane is fixed in the axial direction to ensure symmetry restrictions. The ABAQUS schematic also lacks the existence of the beam's increased depth at midspan since the results are desired for comparison with DSAS, not the experimental data. As shown in Figure 3-11, the beam does extend 7 in. past the supports in an effort to more realistically capture the boundary conditions and stresses at work. The point load is centered at midspan with a few adjacent nodes set as rigid to avoid severe concrete discontinuity at impact, and gravity is dually enacted. Figure 3-15 illustrates the beam schematic via the ABAQUS interface. Lastly, the mesh size of 0.5 inches is a result of running trials to simultaneously capture convergence and promote minimal computation time.

The material models are entered into ABAQUS in two separate regimes: the linear-elastic and the plastic. The normal strength concrete is modeled by the modified Hognestad curve and tension stiffening as displayed in Figure 3-16, while the steel reinforcement model is an adjusted Hsu (1993) curve for steel embedded in concrete per Figure 3-17 (the curve is compared to the strain-hardening steel model of section 2.3). Though the yield point is based on the Hsu model, the remainder of the model is 'linearized' to reach the ultimate stress. Note that the material models are illustrated without the application of DIFs. Nonlinear, inelastic behavior in ABAQUS requires the specification of true stress and plastic strain experienced post yielding, and the input must be aptly adjusted. The NSC behavior is more specifically detailed by the concrete damaged plasticity (CDP) model, the parameters of which derive from previous studies (Morency 2010). The dilation angle, eccentricity, fbo/fco, K, and viscosity parameters are respectively set to 40, 0.1, 1.16, 0.6667, and 0 (SIMULIA 2010). The CDP model is designed to account for the lessening of elastic stiffness through cyclic loading in the plastic regimes, and it is therefore well-suited for the imposed dynamic load.

The Beam-1C ABAQUS output is compared in Table 3-7 against the DSAS results. Overall, correlation exists between the maximum-response data gathered. Demonstrated by the case however is ABAQUS's negligible depiction of the beam's rebound after achieving its peak deflection. Figure 3-18 displays the lack of congruency. A reasonable explanation for the discrepancy is the lack of specifics known about the concrete's damage criteria. Once again, the modeling is largely theoretical and results must be approached from this perspective. The contrast credits DSAS with the ability to more succinctly evaluate a member's elastic and plastic deformations.

The rotation and curvature data at the peak response are compared in Figures 3-19 and 3-20, respectively. Note that the depicted beam length is 120 inches while the span is 106 inches and that the ABAQUS nodal points are positioned every four inches along the tension rebar. Given the symmetry of the analysis, the rotation data was drawn from ABAQUS for half of the span and then inversely replicated for the second half-span. Excepting for the ABAQUS scattering, the graphs communicate similar behavioral descriptions, and a similar procedure for relaying deformation specifics is thereby implemented throughout the parametric study for a more in-depth analysis.

3.5 Parametric Study

The congruency shown to exist between DSAS and ABAQUS for the dynamically loaded beams provides the foundation for conducting a parametric study. The study expands to incorporate UHPC as a second investigated material model, in addition to the reinforced NSC formerly addressed. The investigation also varies the boundary and loading conditions imposed on the columns for assessment. The basic experimental procedure is now introduced with the analysis of results processed in Chapter 4.

In terms of the boundary conditions, simply-supported and fixed-end columns are the primary focus. These forms of support are common of columns situated within protective structures. Their consideration encompasses a broader scope of conditions (fixed-free, simple-fixed, etc.) as they represent the least and most complex hinge behaviors of a single span column. For a simply-supported column, a single plastic hinge is expected to develop at a critical location (analogous to that of the maximum moment) along the column span, as shown by the validating case. For a fixed-end column, three plastic hinges are expected to evolve in sequence of maximum moment magnitude: two at the supports and one at a critical location along its length.

Various instances of blast and axial loads are also imposed on the four column types (combinations of NSC, UHPC, simple supports, and fixed supports). The blast pressures are assumed to be uniformly distributed across the column span and linearly decrease through time as per the triangular loading of Figure 2-7. Table 3-8 provides a sample of the blast parameters imposed for the trial runs, including the reflected pressures and impulses to which the columns are subjected and the resultant positive duration times for proper configuration. The blast pressure and impulse magnitudes are intended to correlate with the work performed by Morency (2010) and derive from the blast parameter curves proposed by the Unified Facilities Criteria (2008). The study primarily focuses on the set of blasts run in the absence of axial load, while additional trial trials are placed under axial loads to vary between 750 and 1750 kips for the NSC column and 1750 and 5750 kips for the UHPC column.

The parametric study aims to evaluate the appropriateness of DSAS's analysis. Since the plastic hinge is represented by a single element, a constant curvature is inherently imposed across it. However, the region outside of the hinge is not expected to substantially exceed the yield curvature and requires examination. The range of blast pressures is intended to mark different points along the column's load-deflection curve, thereby promoting various deformation and curvature stages and the creation of evolution diagrams. Finally, the employed hinge length calculation is analyzed and any necessary recommendations for its correction are made.

3.6 Summary

The methodology followed for the analysis of the plastic hinge formation in normal strength concrete and ultra high performance concrete columns has been presented throughout this chapter. The verification of DSAS's and ABAQUS's compatibility with

the experimental data of Feldman and Siess for Beam-1C and Beam-1H establishes a basis for the parametric study. With the acceptance of the material model for normal reinforced concrete, the next chapter develops the UHPC material model and narrows on the effects held by varying boundary conditions and combinations of blast and axial loads on the hinge formation. The parametric study's analysis also conveys the modeling assumptions made and their respective impact.

Table 3-1. Plastic hinge length expressions and calculations for the test beam.

Expression	Equation	Length (in)
Corley	$0.5d + 0.2(z/\sqrt{d})$	8.4
Mattock	$0.5d + 0.05z$	7.7
Sawyer	$0.25d + 0.075z$	6.6
Paulay and Priestly	$0.08L + 0.15d_b f_y$	14.7
Sheikh and Khoury	$1.0h$	12.0
Effective Depth	$d – d'$	8.5

Table 3-2. Beam-1C and Beam-1H material properties.

Property	Beam-1C	Beam-1H
Concrete		
f'_c (psi)	6000	5775
E_c (ksi)	4000	4450
f_t (psi)	733	935
Steel		
f_y (psi)	46080	47170
E_s (ksi)	29520	34900
ε_y (in/in)	0.0016	0.0014
ε_o (in/in)	0.0144	0.0150

Table 3-3. DSAS peak responses per the inclusion of behavioral effects.

Effect	Beam-1C (in)	Beam-1H (in)
None	7.40	7.65_{Fail}
Diagonal Shear	9.42_{Fail}	8.65_{Fail}
Compression Buckling	6.69_{Fail}	6.74_{Fail}
Estimated Strain Rate	2.83	3.93
Diagonal Shear & Estimated Strain Rate	6.61	8.70

Table 3-4. Strain rate effect on DSAS output.

Effect	Maximum deflection - 1C (in)	Final deflection - 1C (in)	Maximum deflection - 1H (in)	Final deflection - 1H (in)
None	7.40	5.52	8.65_{Fail}	8.65
DSAS Strain Rate Estimate (1.43 in/in)	2.83	2.18	8.70	7.92
Feldman & Siess Strain Rate Estimate (0.3 in/in)	3.47	2.82	9.08_{Fail}	9.08

Table 3-5. Dynamic increase factors for beams 1C and 1H.

Beam	Concrete in compression, f'_c	Concrete in tension, f'_t	Yield steel, strength, f_y	Ultimate steel strength, f_u
1C	1.3	2.5	1.2	1.2
1H	1.3	3.0	1.2	1.2

Table 3-6. Comparison of experimental and DSAS output for beams1C and 1H.

Beam	Exp. maximum deflection (in)	DSAS maximum deflection (in)	Exp. permanent deflection (in)	DSAS permanent deflection (in)
1C	3.0	3.01	2.2	2.35
1H	8.9	8.70	7.5	7.92

Table 3-7. Comparison of DSAS and ABAQUS output for Beam-1C.

Deflection	DSAS (in)	ABAQUS (in)	% Difference
Maximum	3.01	3.15	4.4 %
Final	2.35	2.96	20.6 %

Table 3-8. Sample of parametric study blast trials.

Trial No.	Reflected pressure (psi)	Reflected impulse (psi-ms)	Duration time (ms)
1	1777	1134	1.276
2	2922	1875	1.283
3	3602	2369	1.315
4	4208	2844	1.352
5	4757	3305	1.390

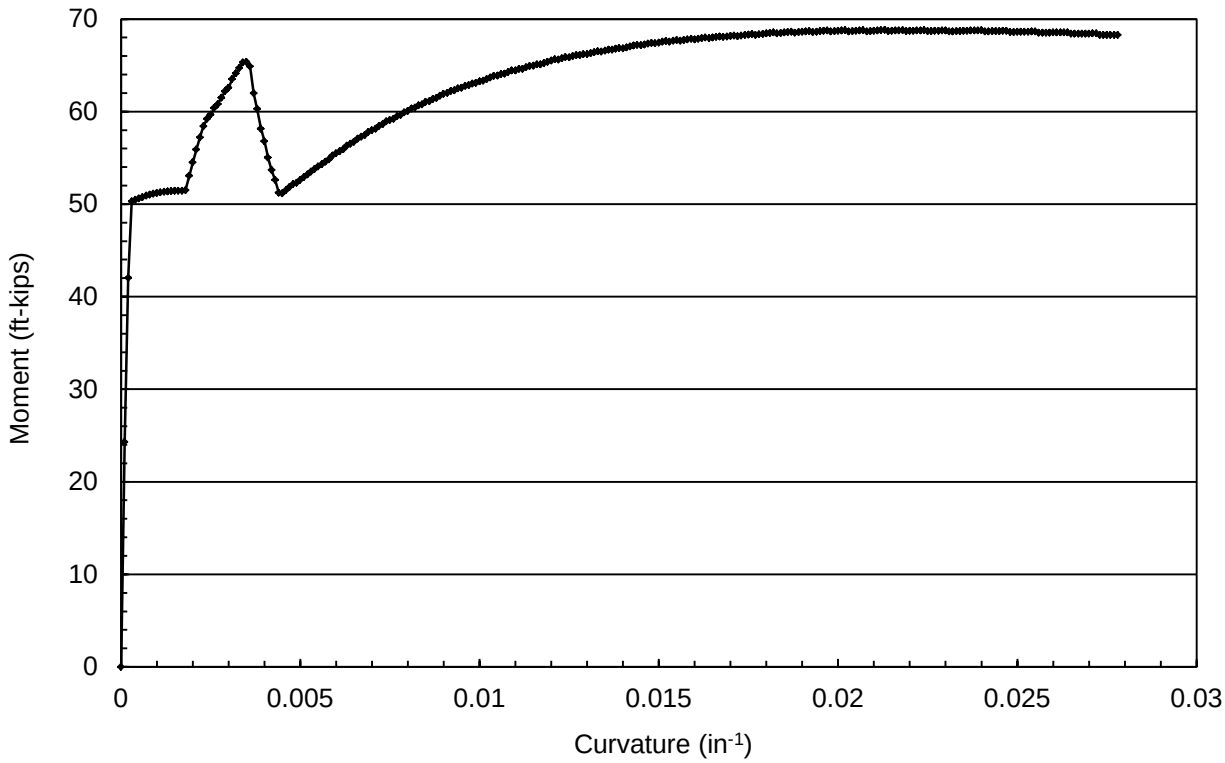

Figure 3-1. Moment-curvature diagram for test beam.

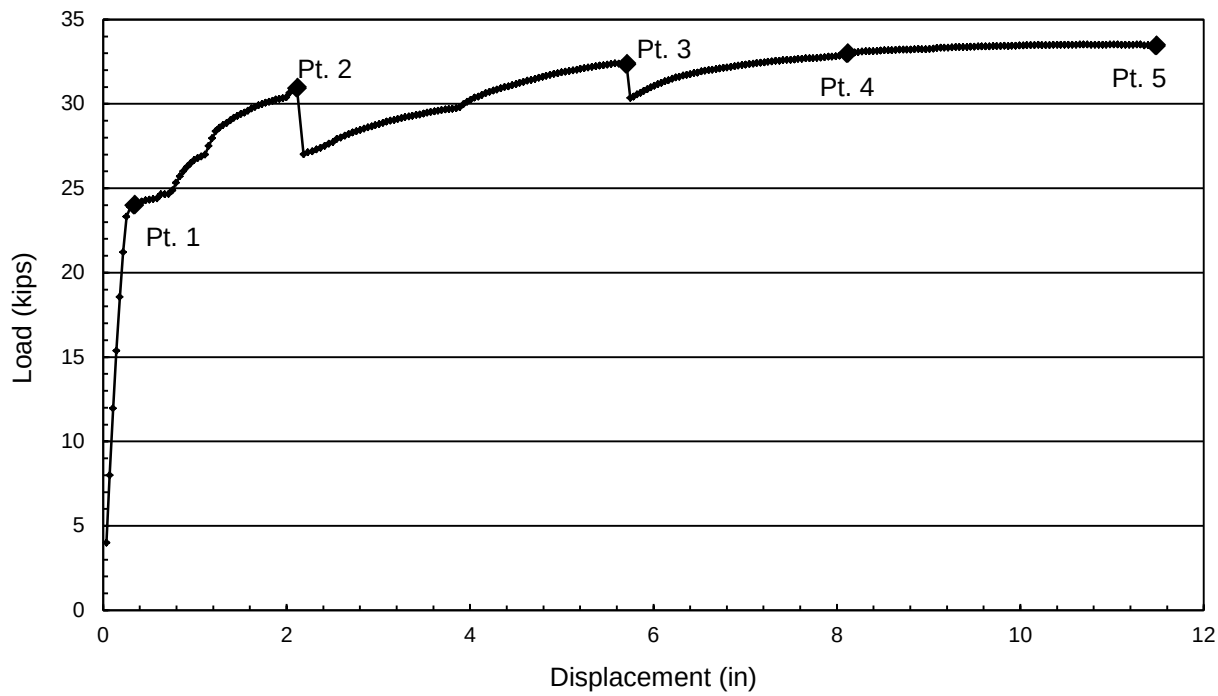

Figure 3-2. Load-deflection curve for test beam with 19 nodes.

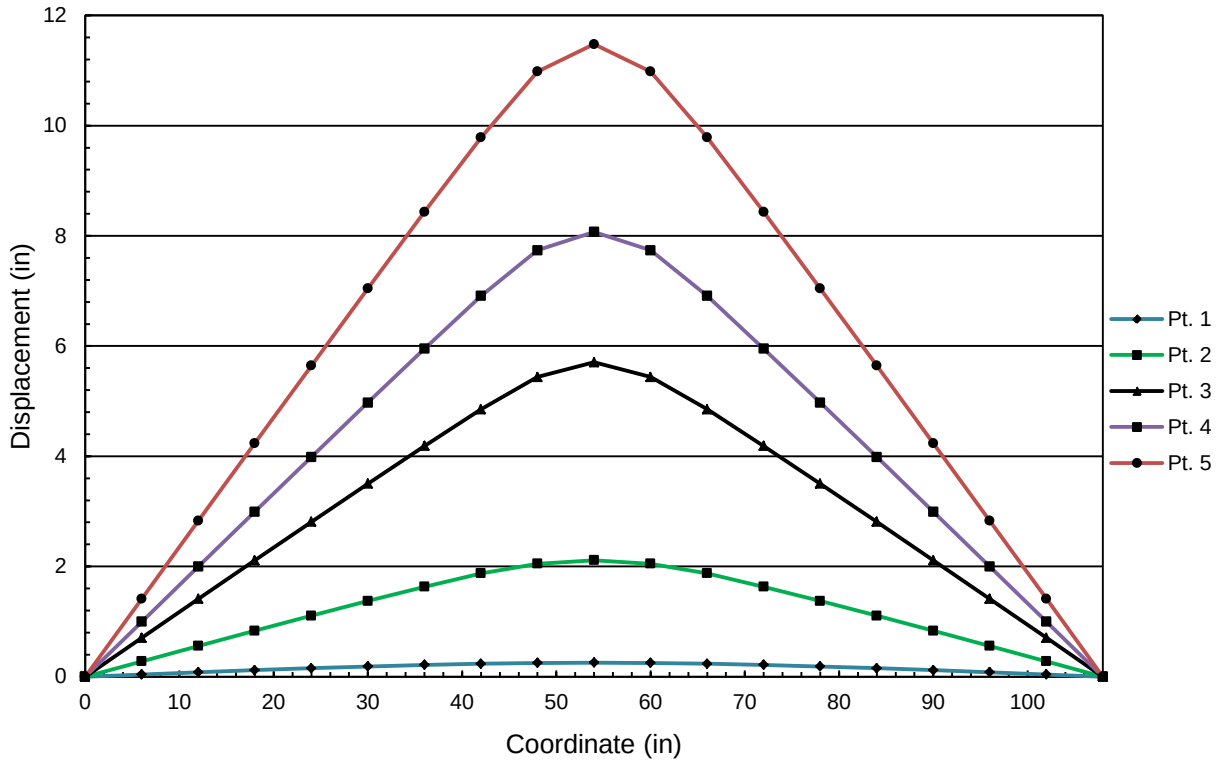

Figure 3-3. Progressive deformed shape of test beam with 19 nodes.

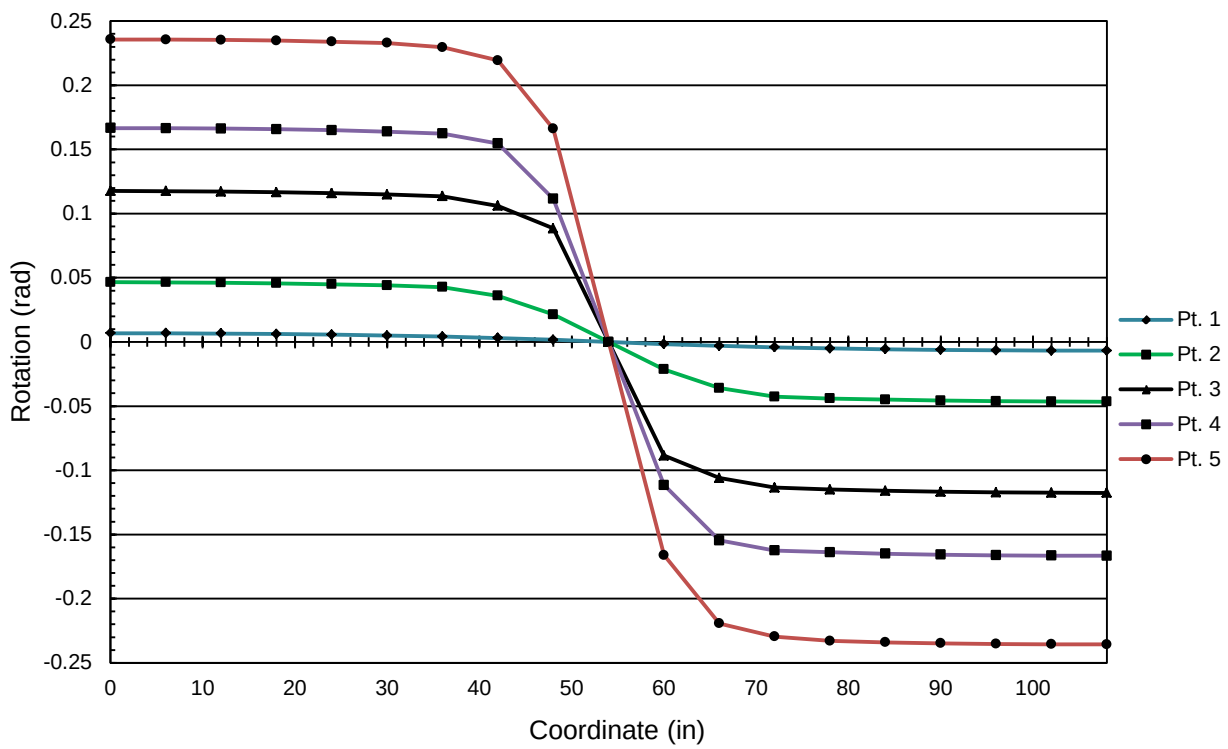

Figure 3-4. Progressive rotation of test beam with 19 nodes.

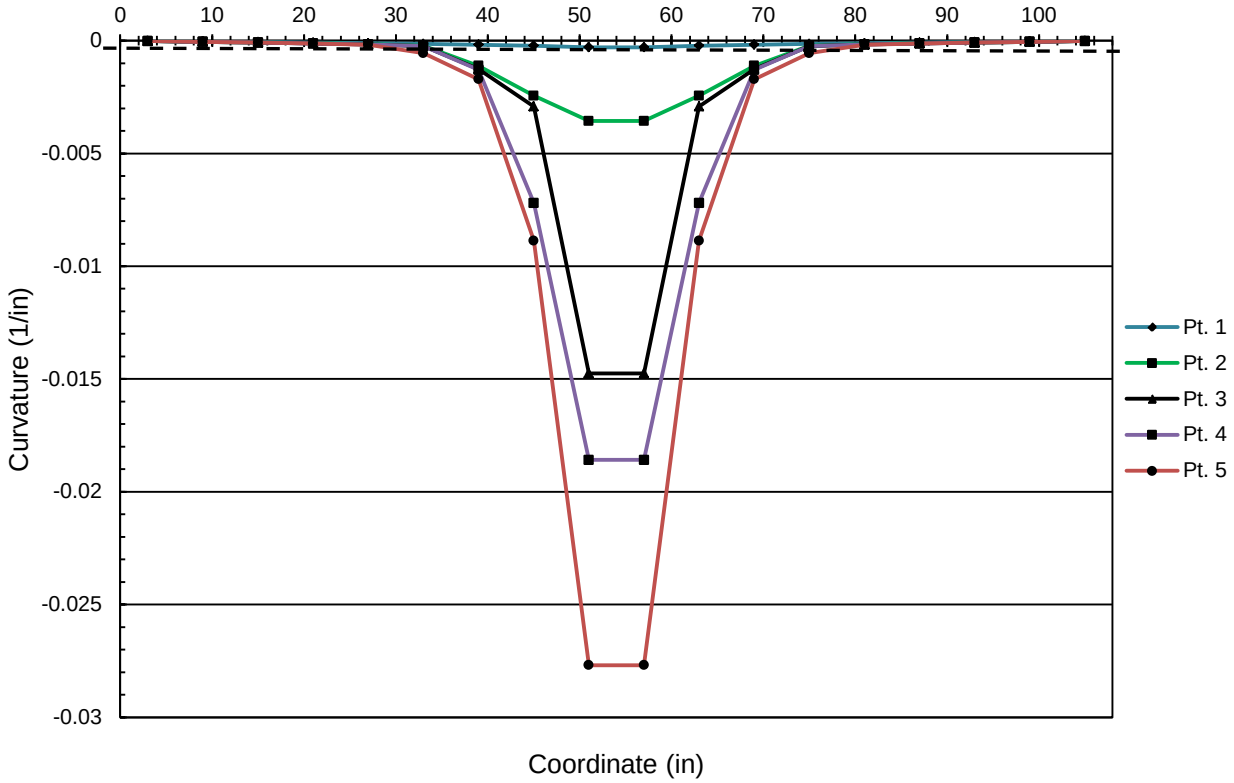

Figure 3-5. Progressive curvature of test beam with 19 nodes.

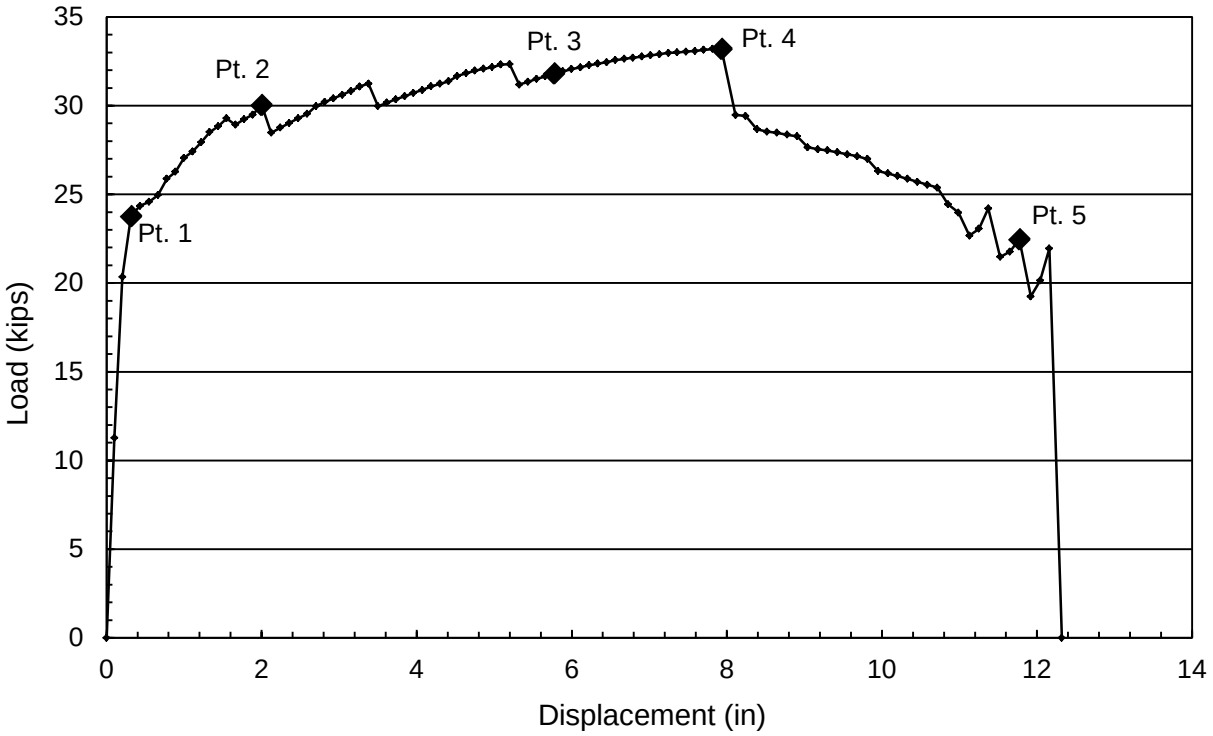

Figure 3-6. Load-deflection curve for test beam with 51 nodes.

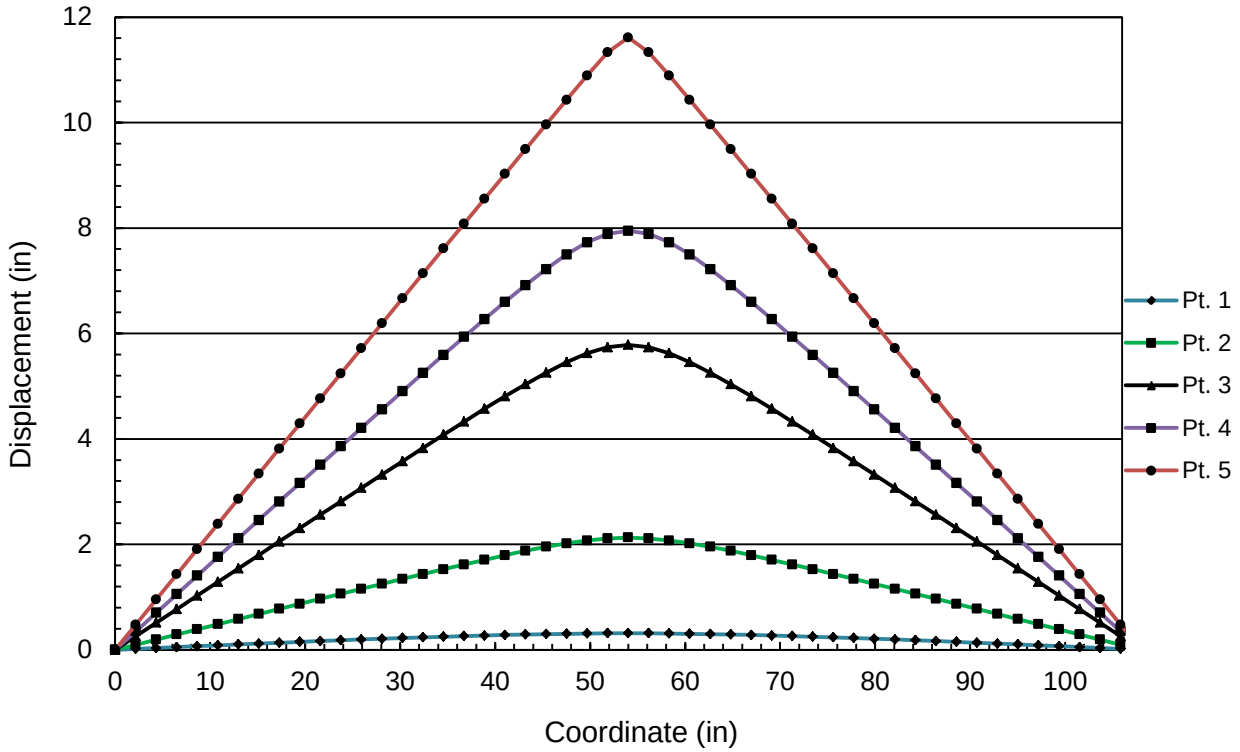

Figure 3-7. Progressive deformed shape of test beam with 51 nodes.

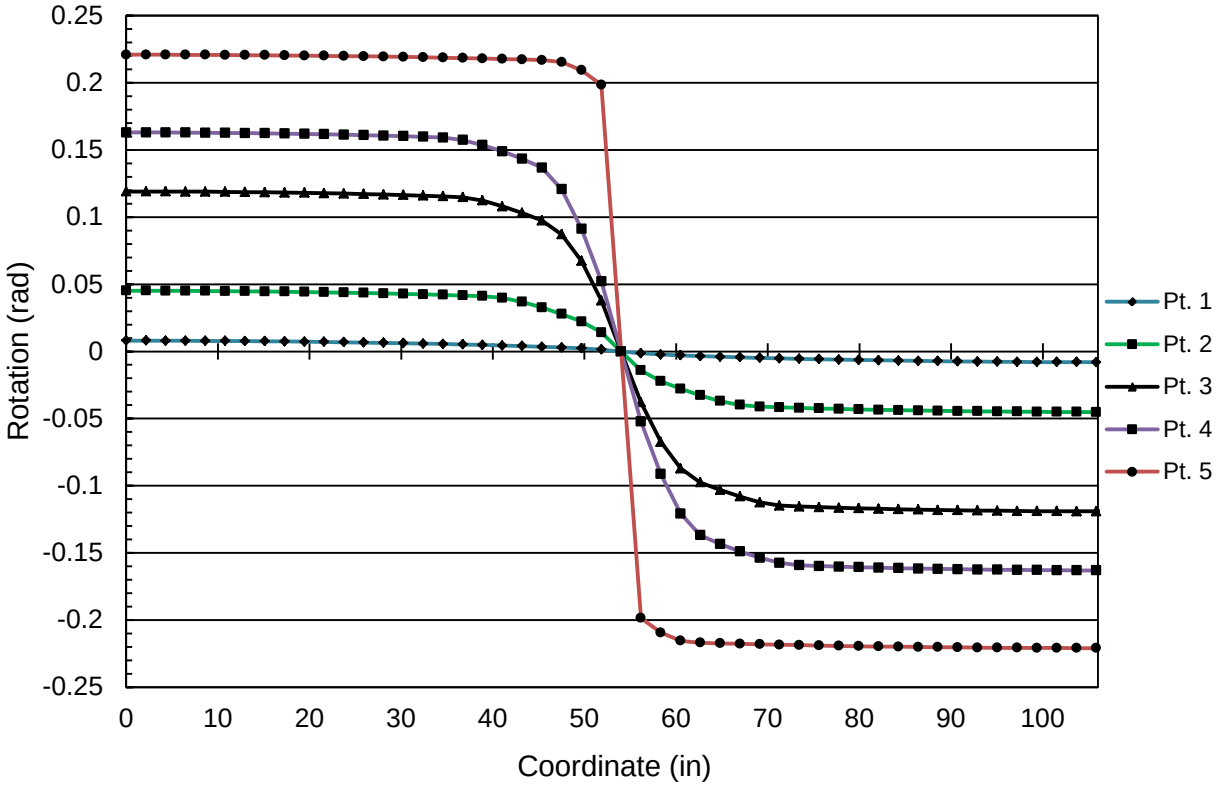

Figure 3-8. Progressive rotation of test beam with 51 nodes.

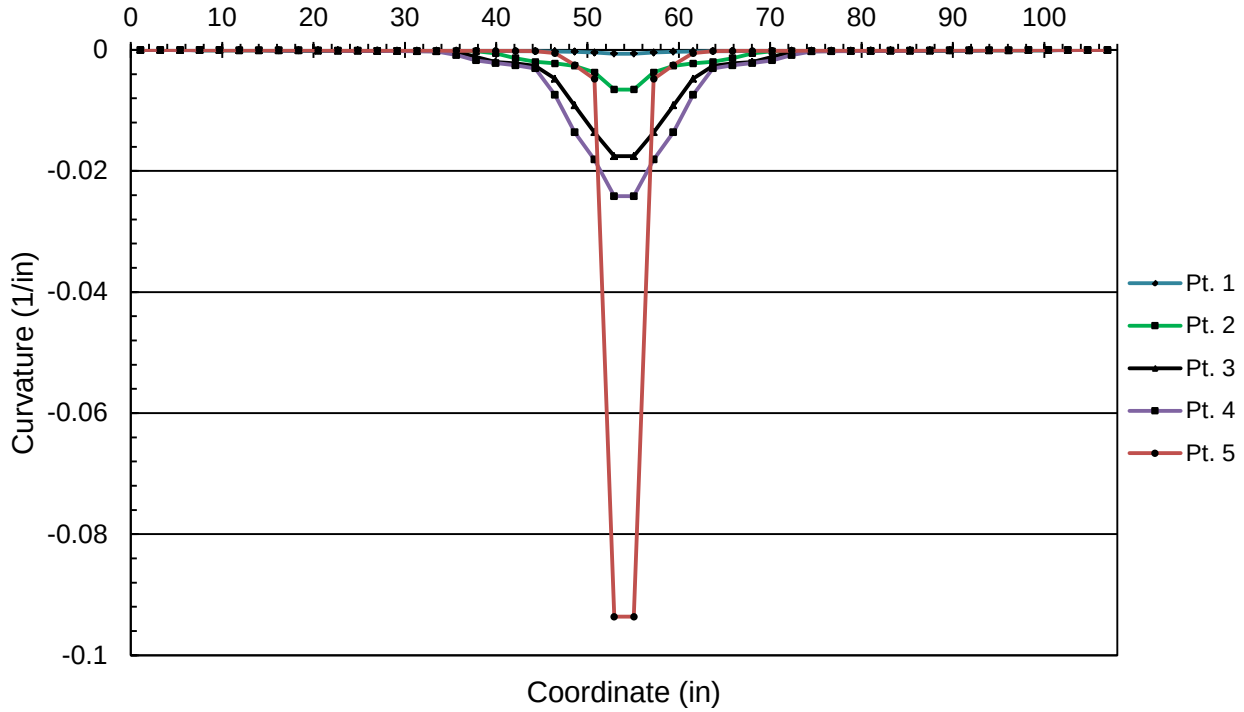

Figure 3-9. Progressive curvature of test beam with 51 nodes.

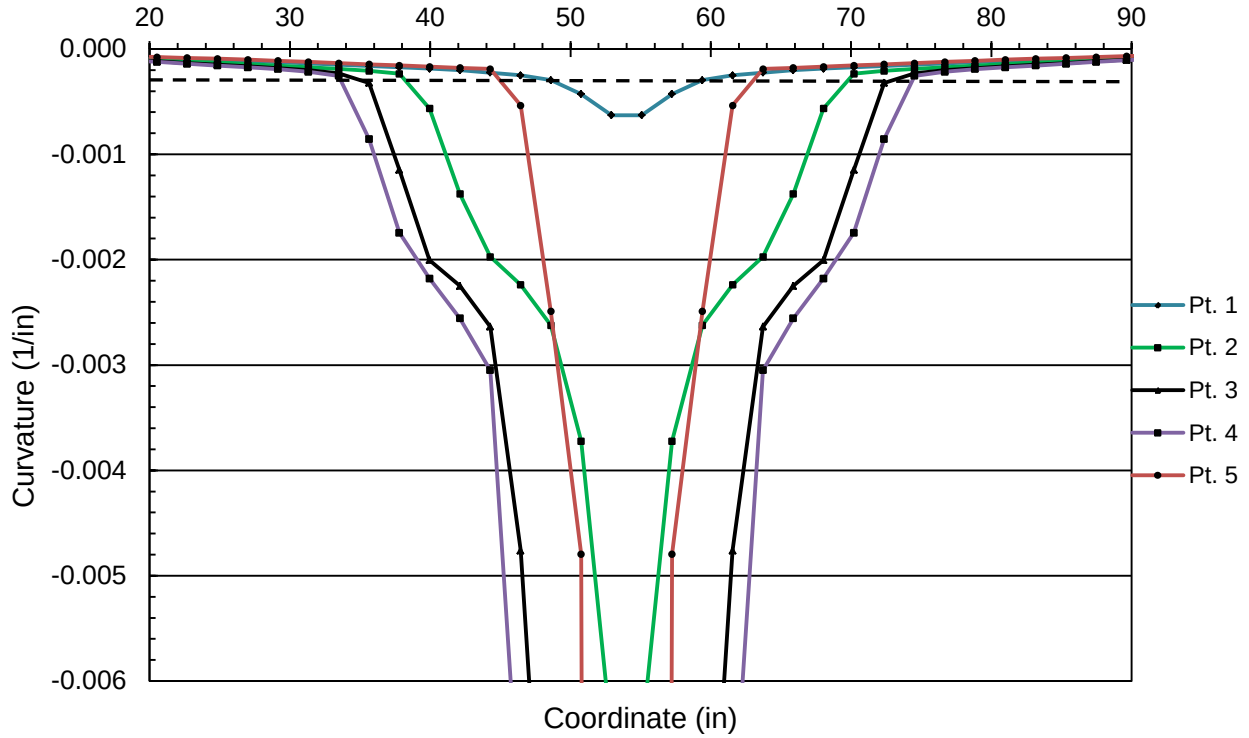

Figure 3-10. Zoomed progressive curvature of test beam with 51 nodes.

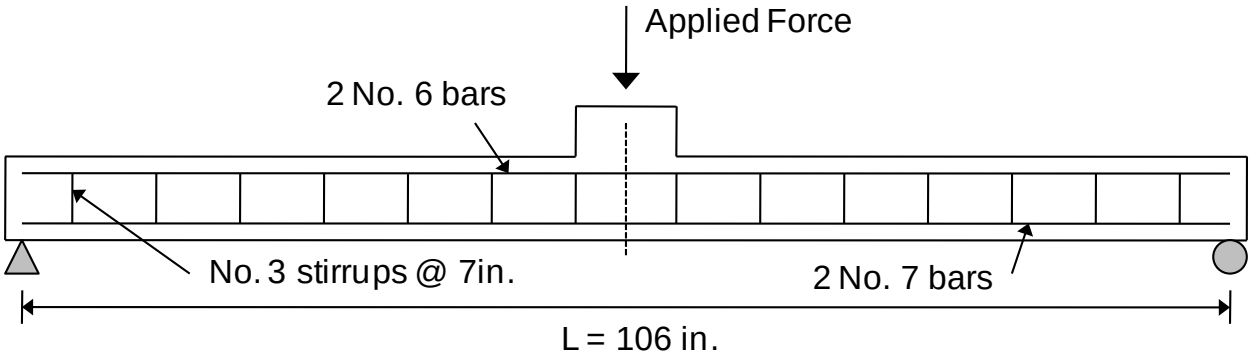

Figure 3-11. Experimental setup for beams 1C and 1H.

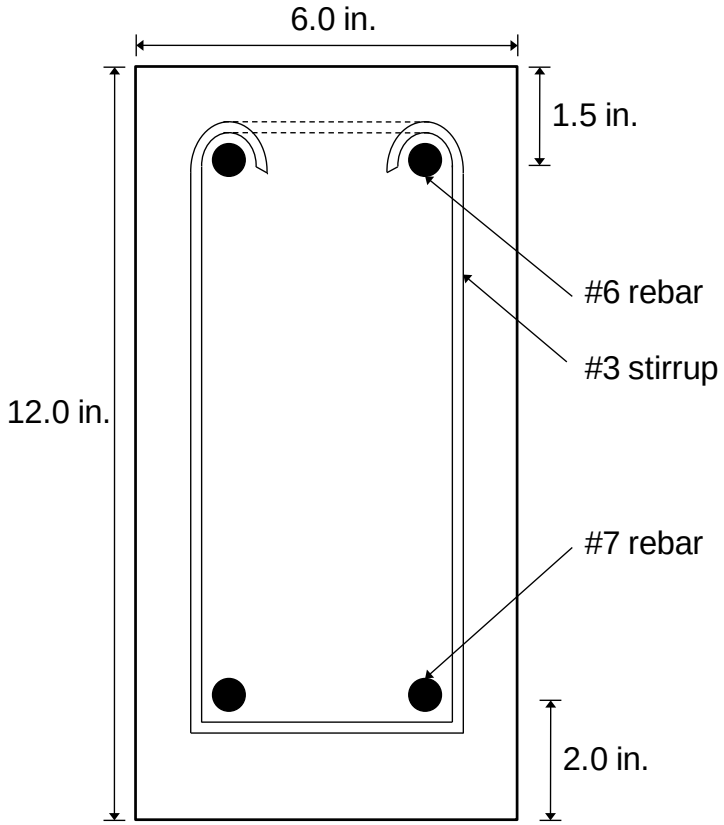

Figure 3-12. Cross-section of beam (Beam-1C has open stirrups; Beam-1H, closed).

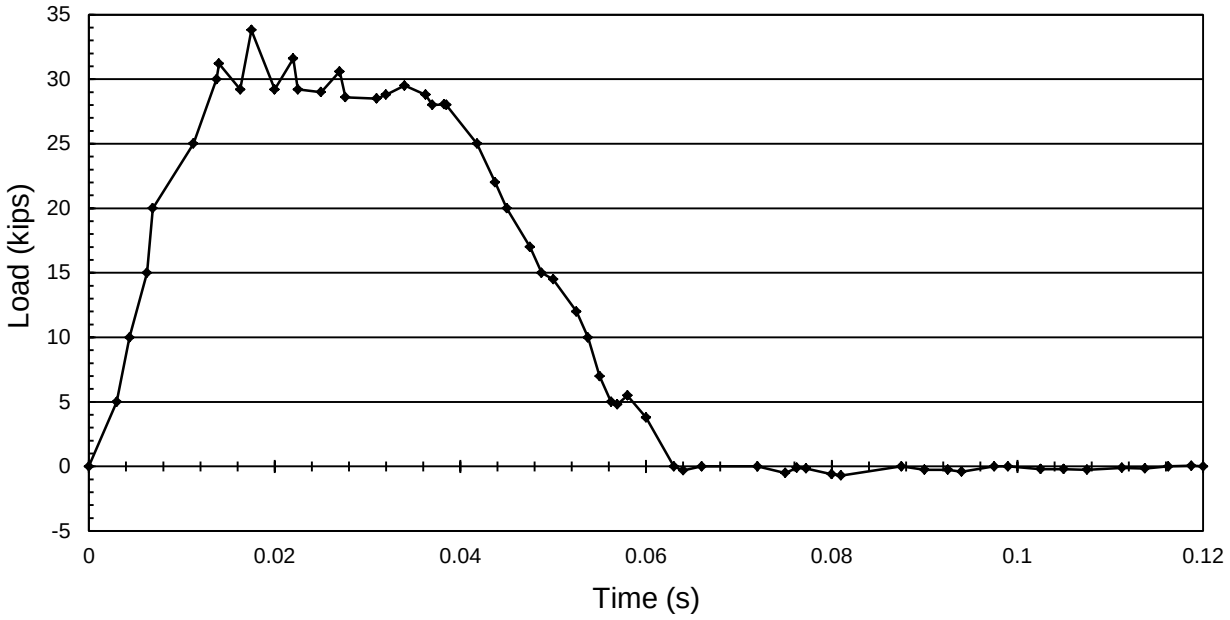

Figure 3-13. Dynamic loading of Beam-1C.

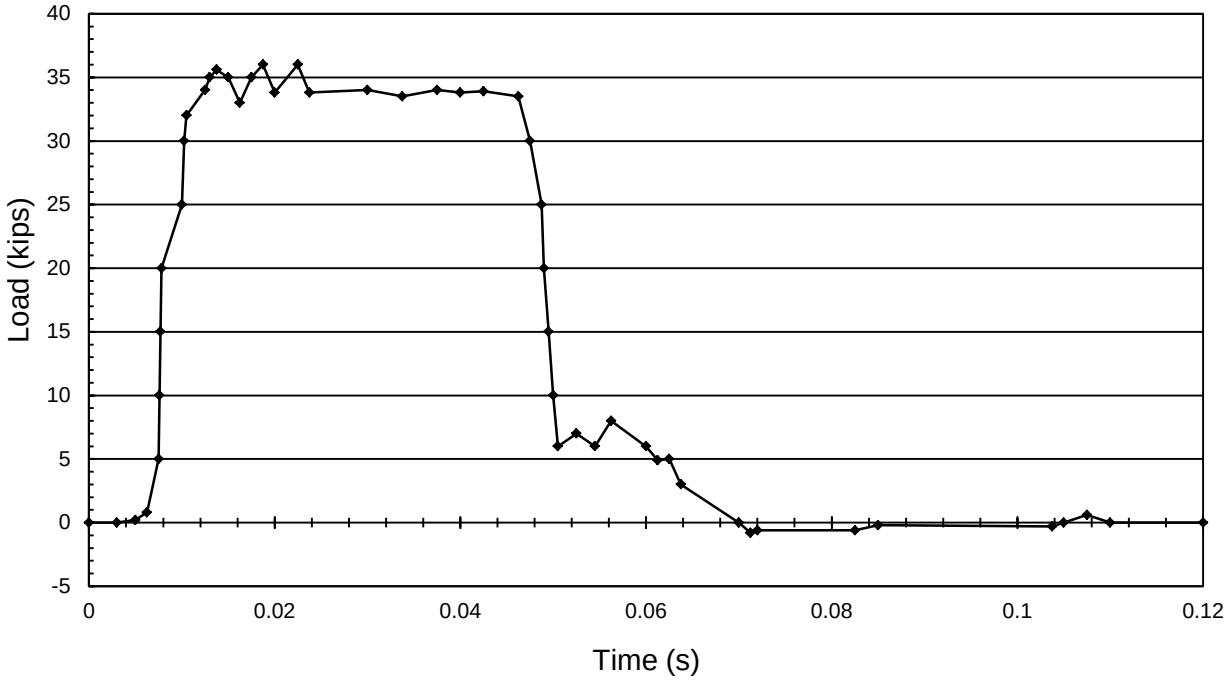

Figure 3-14. Dynamic loading of Beam-1H.

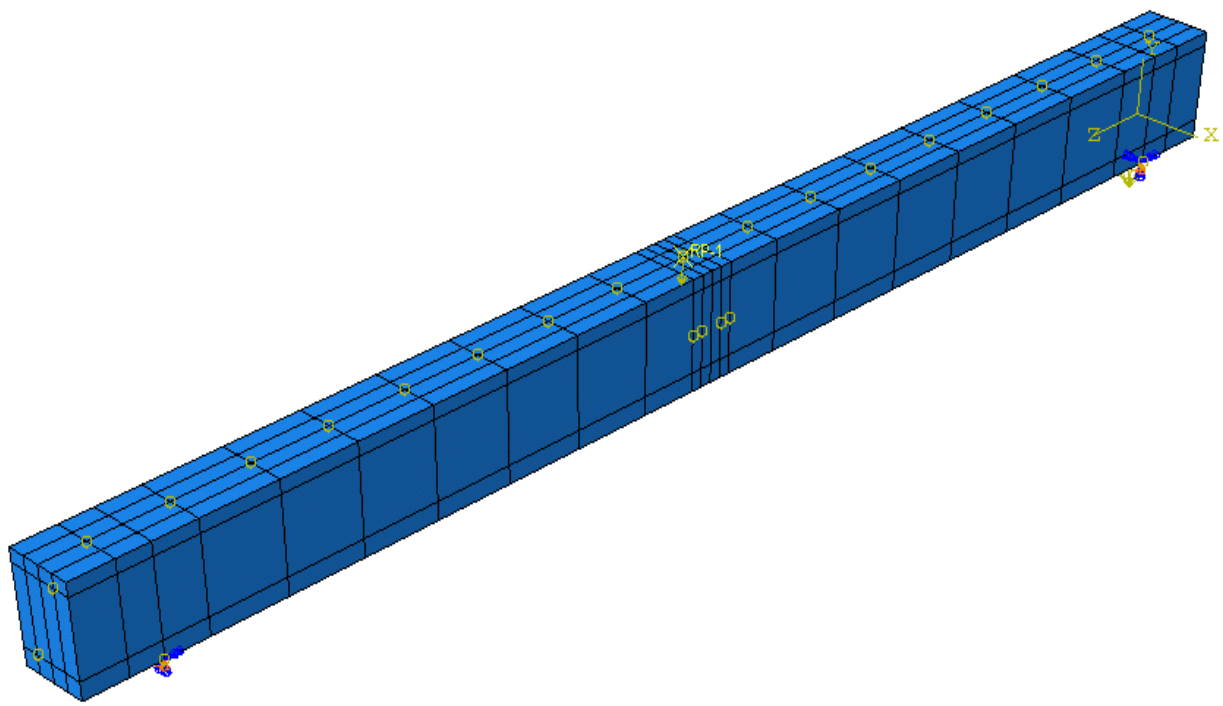

Figure 3-15. ABAQUS interface and Beam-1C schematic.

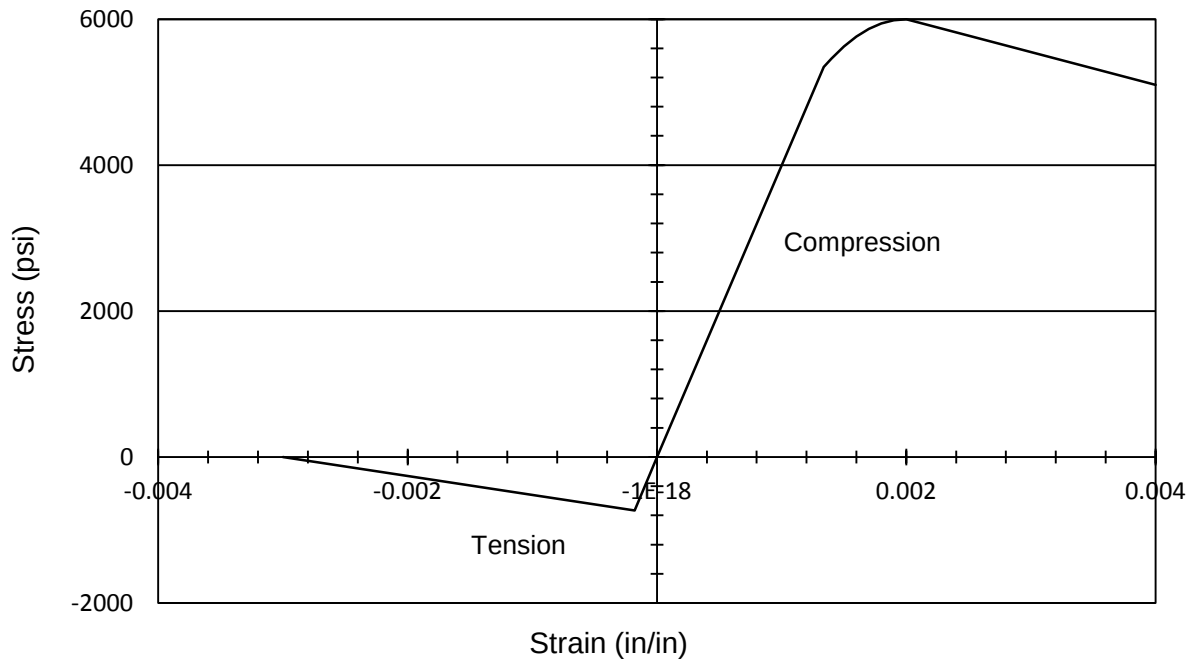

Figure 3-16. Modified Hognestad curve for Beam-1C's normal strength concrete.

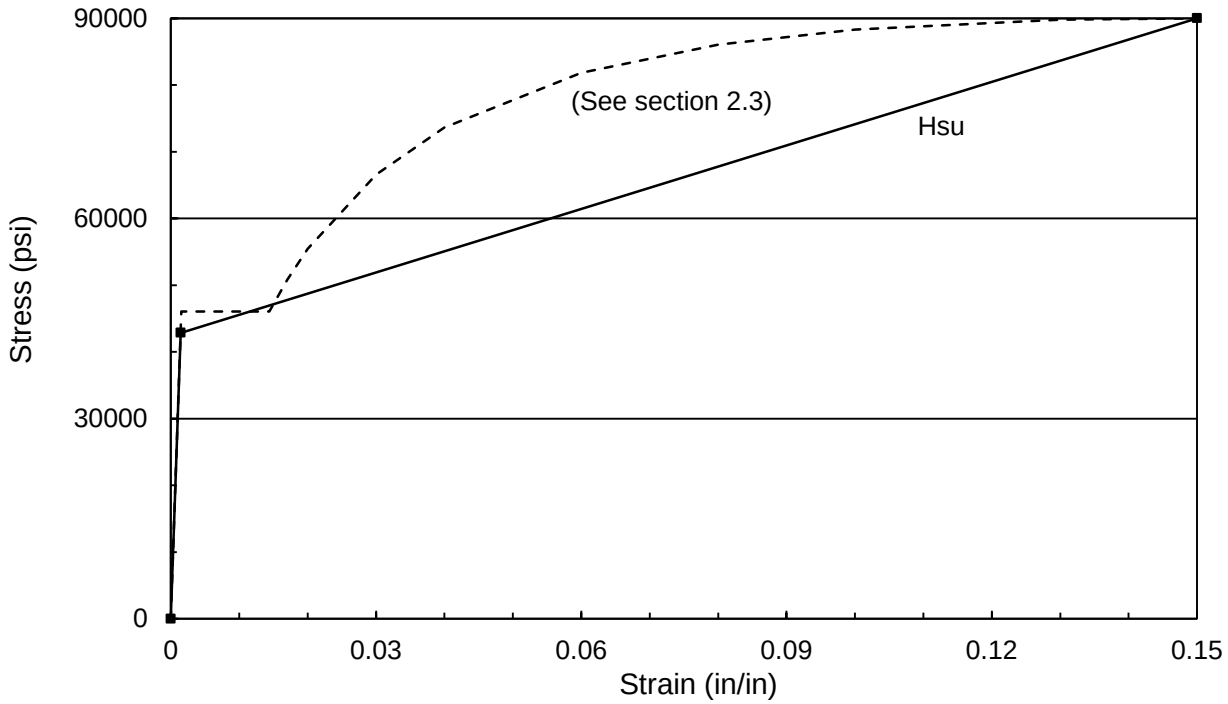

Figure 3-17. Beam-1C steel material model.

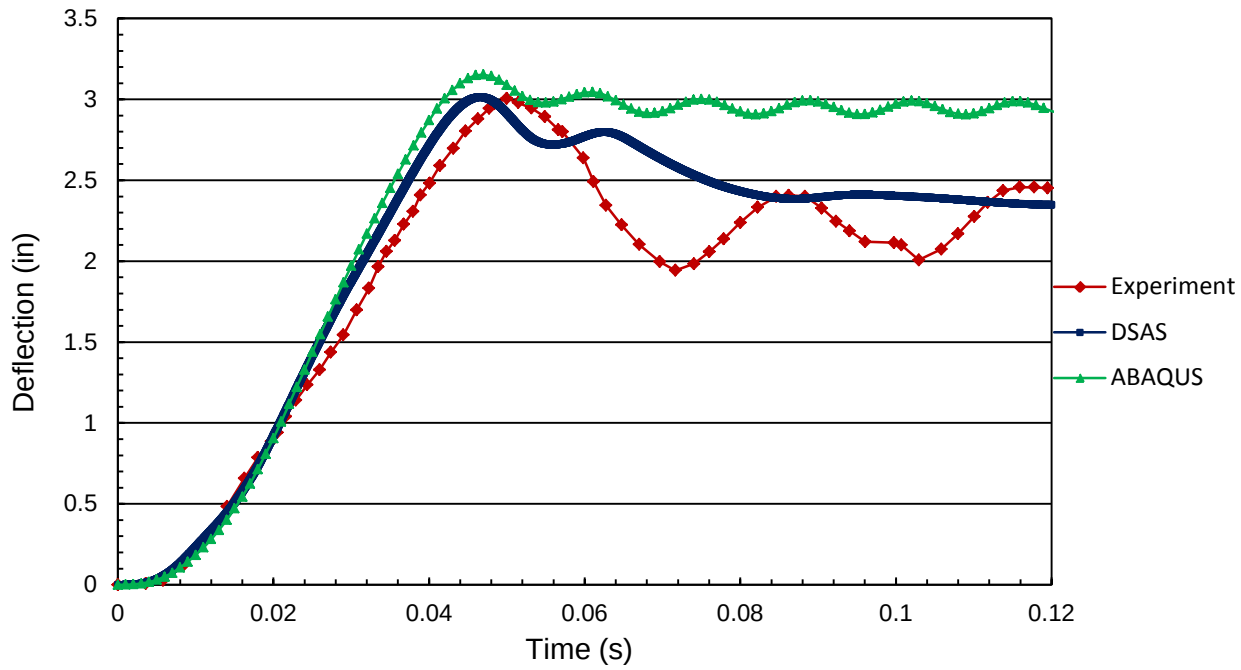

Figure 3-18. Comparison of Beam-1C's response.

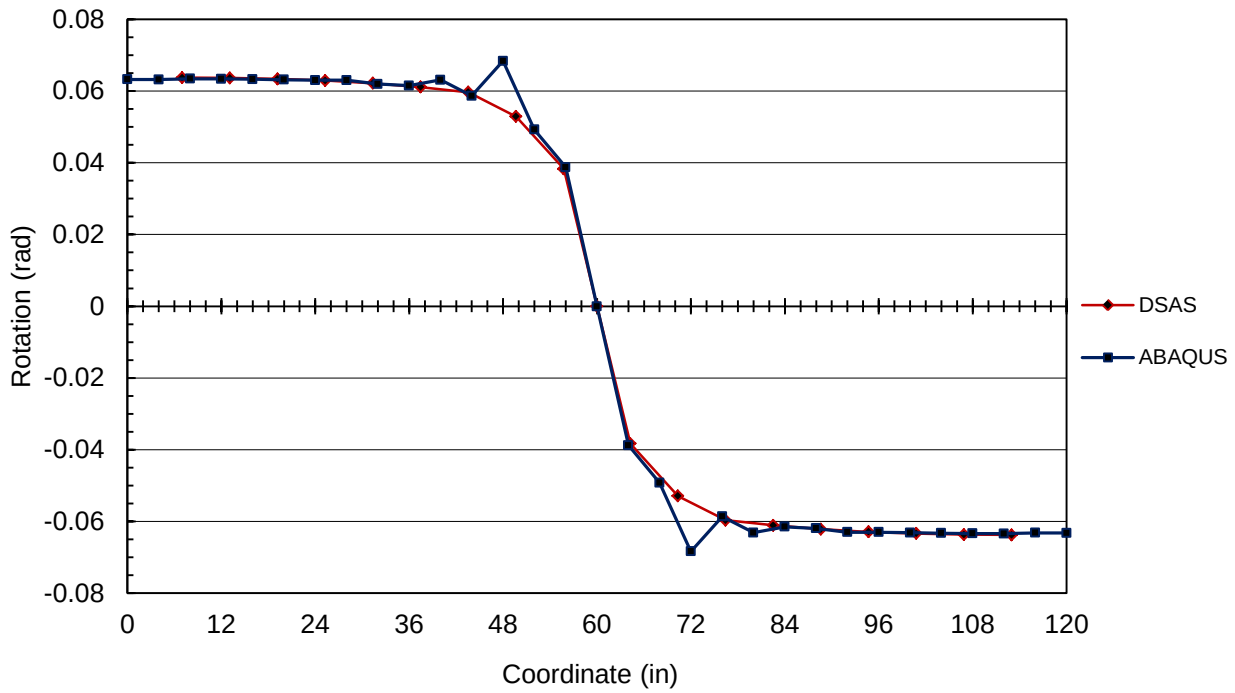

Figure 3-19. Beam-1C rotation at peak response.

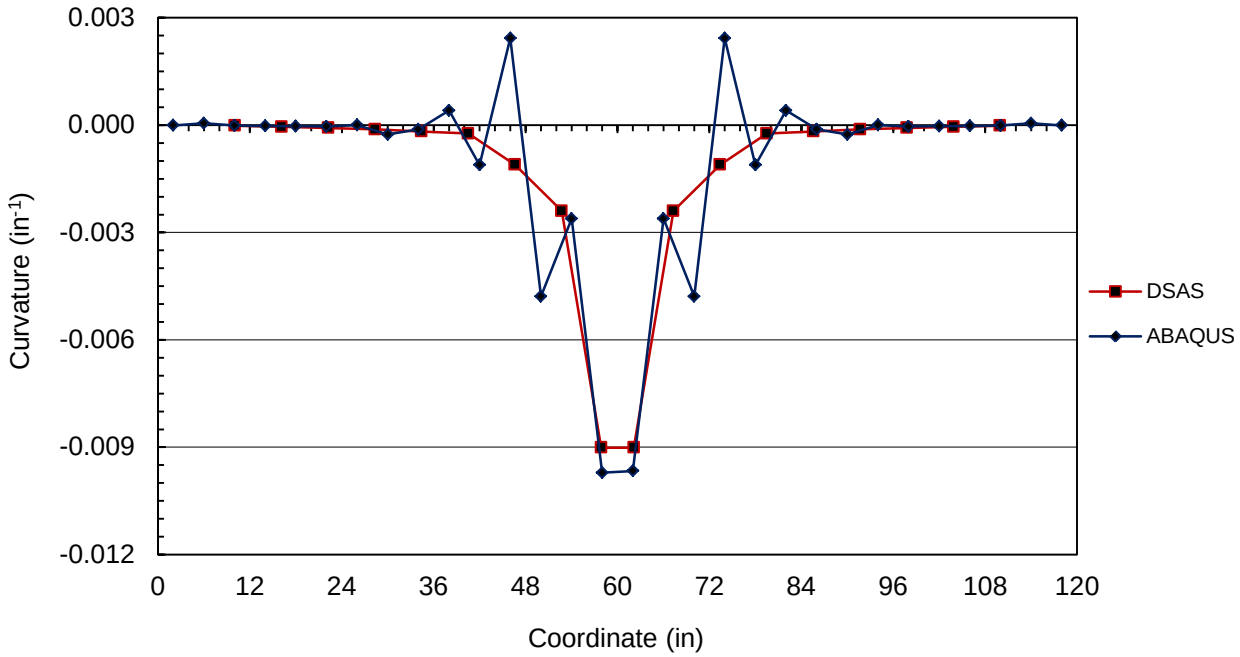

Figure 3-20. Beam-1C curvature at peak response.

CHAPTER 4
ANALYSIS

4.1 Overview

Following the demonstration of DSAS's ability to realistically model the response of reinforced concrete members subjected to severe dynamic loads, the study narrows its focus onto concrete columns. Just as for the previous Beam-1C work, DSAS V3.2.1 (Astarlioglu 2008) and ABAQUS/Explicit V6.10 (SIMULIA 2010) are the analysis programs used to complete the parametric study outlined in section 3.5. Although the two programs have been comparatively validated from a maximum deformation standpoint, the curvature schemes they project are now more critically evaluated. The presented analysis is theoretical and seeks to establish a reasonable method for processing the inelastic behavior of NSC and UHPC. Furthermore, in contrast to the extensive documentation of NSC's behavior is the lack of an equally well-defined UHPC model, and the study implements an experimental model derived from multiple proposals. The ongoing characterization of UHPC and the various mixture proportions and construction techniques that may be used for its creation leave the proposed UHPC constitutive models subject to a degree of variability.

This chapter serves to study the formation of plastic hinges in normal strength and ultra high performance concrete columns and to compare the two materials' inelastic and large deformation characteristics. Section 4.2 establishes the NSC column's geometric and material properties and addresses the evolution of its deformation and curvature under a series of increasing blast loads for both simple and fixed boundary conditions. Section 4.3 introduces the UHPC constitutive material model employed and conducts the same column inspection of UHPC as for the NSC, and section 4.4

processes the comparison and contrast of the two concrete types. Section 4.5 then develops a number of additional studies to supplement the background and relevance of the parametric study. For instance, the appropriateness of the plastic hinge length calculation implemented in DSAS as well as the effects of diagonal shear and tension membrane behaviors are considered. Finally, section 4.6 briefly summarizes the key outcomes of the performed analyses.

4.2 Normal Strength Concrete Column

First examined is a normal strength, reinforced concrete column subjected to the Table 3-8 series of blast loads. Figure 4-1 illustrates the column's 16 inch, square cross-section with eight #7 reinforcing bars confined by #3 ties spaced at 12 inches. The column spans 12 feet and overhangs the supports by 6 inches (used for the ABAQUS modeling) as depicted in Figure 4-2. The concrete and steel properties are drawn from those of Beam-1C listed in Table 3-2. Note that adherence to the ACI318-08 (American Concrete Institute 2008) code is maintained for the structural integrity of a column constructed under precast conditions. The overall column geometry and blast loads also resemble those employed by Morency's (2010) investigation in order to expand the breadth of data gathered for potential comparison.

The moment-curvature diagram (from DSAS) for the NSC column is presented in Figure 4-3. As a characteristic of the member cross-section, the moment-curvature diagram is unaffected by the combination of boundary and uniform loading conditions implemented. The displayed curve includes the consideration of diagonal shear as well as tension membrane behavior, and the observed yield and ultimate curvatures are approximately 0.0005 in^{-1} and 0.03 in^{-1}, respectively. The curvatures induced on a NSC

column with simple supports are subsequently detailed, followed by the alteration of the boundary conditions to fixed supports.

To model the column in ABAQUS, the load's time-step is set to invoke the explicit mode for dynamic analysis. The concrete is created as a homogeneous solid while the steel reinforcement is generated by beam elements, and the dynamic increase factors applied to the material strengths are appropriated based on DSAS's estimated strain rate per trial. The employed DIFs are catalogued in Table 4-1 for reference. By analysis, a mesh density of one inch was ultimately deemed computationally efficient.

4.2.1 Simply Supported NSC Column

For this study, the simple-support condition is defined by pin and roller boundary conditions. The simply supported NSC column described is subjected to each of five blasts (labeled trials NS1 through NS5), and the DSAS maximum response results are listed in Table 4-2. The column deflections range between 2.7 and 12.7 inches, well into the large deformation regime. The deflected shape and curvature data drawn from the DSAS output are based on the load-deflection curve of Figure 4-4, which is respective to the point of maximum response, or the midspan point. The progressions of the column's deformation, rotation, and curvature as the blast pressure increases are displayed in Figures 4-5 through 4-7, respectively.

The column's effective depth equates to 13 inches, and this value is employed by DSAS as the plastic hinge length. Since the maximum moment generated by a uniform pressure load occurs at midspan, it is also the expected hinge location. Figure 4-7 chronicles the spread of the curvature over the series of blasts. The NS1 blast serves to push the column past yielding, and at this point, the length of the column's span surpassing the yield curvature is nearly 50 inches (25 inches to either side of midspan)

which substantially violates the predicted plastic hinge length. Based on the NS1 and NS2 curves, it may be plausible that DSAS errs in perceiving the proper curvature across the beam, the mesh is too rough to represent the behavior, or the plastic hinge does not expressly generate as theorized. However, because even the NS1 blast significantly exceeds yield, the column curvatures for small deformations are examined.

In Figure 4-8, the four charted points represent the midspan's deflection increasing from 0.96 to 1.12 inches (deformations just post-yield). The curvature is shown to lock at a distance of 15 inches to either side of midspan as the curvature across the hinge element rises. This behavior reflects that expected of a plastic hinge, and although the designated hinge still exceeds the predicted 13 inches, it is possible that the hinge spreads this distance on either side of midspan or that, again, the mesh may be too large to properly perceive the tightened change in rotation about midspan.

Now transitioning back to the large deformation curvature patterns represented in Figure 4-7, although yield is exceeded for the NS4 and NS5 trials, there exists an obvious jump in curvature upon reaching 0.003 in^{-1}. If this area is to be characterized as the plastic hinge, its length is roughly equal to the one present at post-yield (Figure 4-8). The trend observed may also be related back to the cross-sections's moment-curvature, where an increase in the supportable moment is demonstrated after the initial yielding plateau (approximately at 0.002 in^{-1}). In order to decipher whether this regeneration of the 'later' hinge is appropriate, the ABAQUS results are consulted.

Table 4-2 lists the ABAQUS peak responses alongside those from DSAS for the blast trials. The compatibility of the results varies in accuracy; the occurrence of which is discussed in section 4.4. Figure 4-9 provides an ABAQUS illustration of the NSC

column after subjection to the 2922 psi blast load, and Figure 4-10 chronicles the ABAQUS deflected shape for the NS1, NS2, and NS3 cases. While the NS4 and NS5 cases resemble exaggerated deflected shapes of NS3, they are not shown for simplicity and clarity of the figure. Note that the deformations presented correspond to the final state of the mid-depth rebar and not the peak response. For the lower blast pressures, the column deforms as expected and assumes a somewhat triangular shape. For the NS3 and non-plotted NS4 and NS5 cases however, the column is shown to deflect under a severe impact with high rotations nearer to the boundaries. To inspect the hinge formation of the more triangular deformed shape, the rotations of trials NS1 and NS2 are observed in Figure 4-11. The ABAQUS output is from a collection of nodes along the column's rebar spaced at one inch and demonstrates an incurred variability. Shifting of the critical section slightly away from the midspan point is observed because of the allowance of axial deformation and the enactment of gravity. Due to the simple supports, small vertical deformations misalign the nodal references. The small, incremental node approach to curvature results in the NS1 curvature plot of Figure 4-12 with a rough estimate plot accompanying it (derived from manually smoothing the rotation curve). Given the difficulty in deciphering the ABAQUS curvature from its plot, the hinge length is estimated on the rotation curve. A near-constant change in rotation occurs 12 inches to either side of midspan which reiterates the extended hinge length observed in DSAS. Unlike DSAS however, the ABAQUS curve shows a greater adherence to the yield curvature.

4.2.2 Fixed NSC Column

By fixing the column's supports, three plastic hinges are expected to form as opposed to a single one at the critical location. Due to the moment distribution induced

by a uniform pressure load, a hinge first forms at each boundary and then a third hinge generates at midspan (the location of maximum moment along the column span). To conceptualize this occurrence, the response data of cases NF1 through NF5 are extracted from DSAS and ABAQUS. Table 4-3 compares the peak midspan deflections recorded by the analytical programs.

The load-deflection curve of the fixed column is shown in Figure 4-4 for differentiation with that for the simply supported column. At a certain point, the fixed support curve is observed to realign with the simple support curve, plausibly due to the loss of rotation stiffness at the supports. The progressions of deformation, rotation, and curvature for trials NF1 to NF5 are displayed in Figures 4-13 through 4-15. Indicated by the sharp changes in rotation in Figure 4-14 and the peaking curvatures of Figure 4-15, it is evident that three hinges are present as expected. Outside of the hinge elements located at the supports, the curvature abides to yield. The dictated hinge length of 13 inches may even be larger than necessary to represent the plasticity at the fixed ends. The midspan plastic hinge behaves similarly to its simple support counterpart. A significant spread of the column's mid-section deviates from the yield curvature; however, the prominent change in rotation occurs over a more compressed distance. The shorter hinge length (as compared with that at midspan for the simple NSC column) supports the introduction of the *z* parameter (distance from the critical section to the point of contraflexure) to plastic hinge length expressions.

Figures 4-16 through 4-18 respectively further the inspection of deformation, rotation, and curvature by diagramming the ABAQUS data for trials NF1, NF2, and NF3. The larger pressure loads demonstrate the same impact effect of a sharp increase in

deflection nearer to the boundaries, and this response leaves trial NF1 to best illustrate the hinge indicators. Visualized at the supports of trial NF1 in Figure 4-17, the change in rotation transpires over approximately 7 inches, thereby highlighting the potential overestimation of the hinge length at this section in DSAS. At midspan, the yielded portion of the column is maintained within 12 inches to either of its side, and this observation again supports that the hinge spreads one length in each direction from the critical points.

4.2.3 Axial Loads

Realistically, columns serve to support axial loads; transverse, flexure inducing loads via blasting or impact are incidental. To reflect upon how the inclusion of an axial load impacts the peak response of the addressed columns, varying forces are implemented in combination with a few of the simple and fixed column blast loads. The selected axial loads are 750, 1250, and 1750 kips, with the latter being just shy of the column's maximum allowable compressive force. The spread of the axial magnitudes is intended to reasonably capture the fluctuation in column behavior between no axial load and the ultimate load.

Table 4-4 looks at the result of adding an axial load to three of the blasts, namely the 1777 psi, 3608 psi, and 4757 psi cases. The 750 and 1250 kip loads contribute to the columns' deformation resistance, while the 1750 kip load incurs further damage. To compare the boundary conditions in turn, the simple column proves more subjective to the lower loads while the fixed column is more affected by the 1750 kip load.

4.3 Ultra High Performance Concrete Column

To compare ultra high performance concrete with the normal strength concrete, a column setup similar to that shown in Figures 4-1 and 4-2 is modeled. Aside from the

alteration in the material concrete, the only difference between the NSC and UHPC columns is the UHPC's lack of transverse ties. The common use and addition of steel fibers to the UHPC's mixture is intended to provide enough strength to reduce or eliminate the need of transverse reinforcement.

The UHPC material model is based on the compilation of strength models proposed by various research excursions, including Acker and Behloul (2004), Habel et al. (2004), Spasojevic et al. (2008), and Fehling et al. (2004). The constitutive model employed by this study is recognized as the standard in DSAS and is shown in Figure 4-19. In the compressive regime, the strength is model by three linear segments: an elastic region, a level plateau, and a decrease in strength to the ultimate strain. The UHPC dually exhibits impressive strength in tension and displays ductility well into a tension stiffening region. The strength properties are reiterated in Table 4-5 alongside an outline of the rebar properties drawn from the NSC study. Dynamic increase factors are only applied to the steel's material model, and the factors used correspond to those listed in Table 4-1. For ABAQUS and its consideration of the CDP model, the dilatation angle has been inversely related to the compressive strength of concrete, and it is therefore decreased from the value employed to model the NSC. A dilation angle of 35 degrees was determined to best represent the UHPC durability, and all other CDP parameters remain the same as for the NSC.

The result of the UHPC column's cross-sectional configuration is diagrammed in Figure 4-20 as the moment-curvature diagram. This relationship may be compared to that for the NSC column related in Figure 4-3. From Figure 4-20 it is noted that the yield curvature is approximately 0.0005 in^{-1}, while the ultimate curvature is nearly 0.015 in^{-1}.

4.3.1 Simply Supported UHPC Column

The described UHPC column is first situated with simple supports (a pin and roller mechanism) and subjected to the blast load sequence. The resultant peak deflections of trials US1 through US5 are detailed in Table 4-6, including both the DSAS and ABAQUS output. Based on the moment-curvature relationship and stiffness imposed by the boundary conditions, the load-deflection curve in Figure 4-21 is assembled. The deformation, rotation, and curvature charts respectively included in Figures 4-22 through 4-24 delineate the first four blast trials, while trial US5 is absent due to DSAS's load-deflection curve's cutoff at about 9.8 inches. The evolution of the plastic hinge remains evident in Figure 4-24, even lacking the depiction of trial US5. The ultimate hinge is shown to extend 14 inches to either side of midspan, and the curvature outside of the hinge element clearly increases from zero toward the yield curvature.

The ABAQUS files for the simply supported UHPC column illustrate a deviating behavior from the norm. Figures 4-25, 4-26, and 4-27 contain the deflected shape, rotation, and curvature schematics, respectively. The critical section is shown to be misplaced from midspan by nearly 5 inches with uncharacteristic rotations occurring for most trials along the bottom half of the span. The boundary conditions were established as simple, but since axial deformations are permitted and the bottom support allows the freer rotation, the data is offset. Also, the enactment of gravity is expected to somewhat exaggerate the axial deformation effect. Still, spread of the hinge is demonstrated about the span's critical section. The curvature diagram for US1 supports the DSAS hinge estimate by illustrating the spike in curvature to occur between 12 inches on either side of the critical point, while the remainder of the span maintains unyielded curvature.

4.3.2 Fixed UHPC Column

Upon fixing the column's boundary conditions, the response behavior is examined for the formation of three distinct hinges. The DSAS output is a function of the load-deflection curve drawn in Figure 4-21, and the respective deflected shapes, rotations, and curvatures for the blast loaded UHPC column (trials UF1 through UF5) are pronounced in Figures 4-28, 4-29, and 4-30, respectively. On the evolution of curvature graph (Figure 4-30) the hinged sections are clearly defined. The hinge at midspan is observed to grow from 12 inches to 28 inches (or to 14 inch span lengths on either of its sides) and matches the reported simple support behavior. Meanwhile, the elemental hinge at the support provides a sufficient length for the significant change in curvature to occur. Also observed for the fixed NSC column, the boundary hinge may be shorter than projected by the 13.0 inch element.

The comparison of peak responses attained from both DSAS and ABAQUS are listed in Table 4-7. The ABAQUS data expresses the severe mid-column impaction of trials UF2 through UF5 by the chronicled deformations of Figure 4-31. Prominently focusing on trial UF1, the Figure 4-32 rotation curve proves to be fairly smooth and results in the perceivable hinge lengths designated in Figure 4-33. The UF1 curvature plot shows a 6 inch hinge alongside each of the supports and a third 24 inch hinge equally spread at midspan.

4.3.3 Axial Loads

The employed UHPC has nearly four times the compressive strength of the NSC tested, and the axial load supportable by the UHPC column is thereby approximately quadruple that of the NSC column. In contrast to axial loads ranging between 750 and 1750 kips, the UHPC blast trials are coupled with axial loads on the order of 1750,

3750, and 5750 kips. Table 4-8 serves to demonstrate the axial load effect under these specified conditions. The column behaves similarly by either boundary condition; the two smaller axial loads aid in significantly decreasing the peak response, while the 5750 kip load forces slightly greater deformations on the column.

4.4 Contrast of Concrete Types

The dynamic analysis of normal strength and ultra high performance concrete columns with both simple and fixed boundary conditions has been presented in sections 4.2 and 4.3 and are now compared against one another. First, Figure 4-34 demonstrates the difference in the concretes' constitutive models. UHPC's compressive strength is about four times that of NSC and boasts nearly double the ultimate strain. In tension the UHPC is again superior to NSC, in part due to the typical employment of fiber reinforcement. The ductility of the fiber reinforced UHPC is also evidenced by its tensile ultimate strain. For the given geometry, a comparison of the NSC and UHPC columns' moment-curvature diagrams may be made between Figures 4-3 and 4-20. The two materials possess a similar yield curvature, but the UHPC has double the moment capacity at that instance.

Before comparing the maximum response data of the NSC and UHPC columns collected, the perspectives from which the analyses were completed must be understood. For example, diagonal shear and tension membrane behaviors were applied (in DSAS) to both concrete types; the specific effects of which are discussed in section 4.5. As demonstrated by the Feldman and Siess (1958) beam cases, the estimate of diagonal shear may or may not be applicable to each column under the NSC model. Also, whether the same model for the shear reduction factor extends to the heightened properties of UHPC is not verified. The consideration of tension membrane

action is more easily translated to the UHPC case, on the other hand, because of its basis on the longitudinal reinforcement's operation after the concrete cracks. Finally, in order to judge the peak responses off of one another, it is recognized that the UHPC column has no transverse reinforcement or DIFs applied to its concrete strength. While the steel fiber enhancement of UHPC is built into its material model and has been demonstrated to diminish the need for transverse reinforcement, the UHPC column is nevertheless without the confinement applied to the NSC column. Though UHPC has shown a relationship between dynamic strength and strain rate experimentally (Rebentrost and Wight 2009), studies equivalent to those of NSC to determine and specify a consistent DIF relationship have not yet been established. The UHPC column is therefore subjected to the blasts loads without the inclusion of dynamic increase factors, unlike the NSC column.

The DSAS comparison between the simple and fixed NSC and UHPC columns' peak responses is detailed in Table 4-9, while that for ABAQUS appears in Table 4-10. Per DSAS, the use of UHPC on average generates a 16% reduction in deflection for the case of simple supports and a 25% reduction for fixed boundaries. Should DIFs be applied to the UHPC, or should it be determined that diagonal shear is less effective in the UHPC column, the already significant reductions might exceptionally increase.

The formation of plastic hinges varies in representation between DSAS and ABAQUS. Granted that the computational arrangement of DSAS would not generate the fluctuations observed from the ABAQUS one-inch nodes, but even excepting for this variability, the impacted shape ABAQUS configures for the blasts larger than 1777 psi deviates from the shape proposed by DSAS. DSAS proves that after yielding the

column becomes more triangular in nature, linearly shaped between the hinge regions. The deformation in ABAQUS, however, virtually introduces additional hinge-like segments between the support and midspan for large blast pressures or possibly extends the support hinge to a much larger length.

With respect to differences in the plastic hinge formation of NSC versus UHPC, ABAQUS demonstrates no observable discrepancy, while DSAS elicits one important distinction. It was repeatedly shown that the support hinge in fixed columns has a length of or less than the effective depth. ABAQUS supports that the length may be nearly half the effective depth, as most 1777 psi cases promote a 6 inch hinge. At midspan the hinge area consistently extends between 12 and 14 inches toward either boundary. These hinge lengths apply to NSC and UHPC alike. The materials notably differ in their surpassing of yield curvature along the column span outside of the hinge region. UHPC displays a behavior that theory supports: a plastic hinge is noted by a rise in curvature from yield to ultimate. The NSC violates this principle by DSAS calculations, however, as the yielded segment of the column is nearly half of the span.

4.5 Supplemental Behavior Study

A great number of factors affect the flexural behavior of columns subjected to severe dynamic loads. For instance, it was specified that both diagonal shear and tension membrane behavior were considered in the DSAS response calculations of the test columns. In order to more effectively characterize the demonstrated deformations, additional topics under the branch of inelastic concrete behavior are addressed. First, the appropriateness of the selected plastic hinge length formulation with respect to the proposed hinge length expressions is evaluated, and then the individual effects of shear and large deformations are examined by way of DSAS.

4.5.1 Plastic Hinge Length

The preceding discussion of simply supported and fixed NSC and UHPC columns assumed a plastic hinge length equal to the column's effective depth in DSAS. Although this estimation proved to be reasonable for the distance of severe rotation changes to each side of a critical section, as based on the ABAQUS diagrams, it has not yet be gauged against the proposed expressions of Corley, Mattock, etc. (Bae and Bayrak 2008). A brief comparative analysis of the assumed length is therefore conducted against the analytical findings specified in the literature.

The proposed plastic hinge length expressions of section 2.4 employ factors such as section depth, rebar depth, rebar diameter, steel yield strength, and distance from the critical section to the point of contraflexure in their calculations. The result of using other applicable equations for predicting the hinge length of this study's test column is found in the second column of Table 4-11. While the effective depth of 13.0 inches ranges within the spread of the other expressions, it also corresponds well with the others' average. To determine the degree to which the effective depth remains within an appropriate range under different circumstances, Table 4-11 also details the outcome of altering various parameters of the control test column. The parameter changes include lengthening the column (to 14 feet), providing greater rebar cover (to 3 inches), and compacting the column depth (to 12 inches). Overall, several of the hinge length equations depend upon similar factors, i.e. functions of the column's depth, and allow the effective depth to correspond well with the changes in column geometry.

4.5.2 Shear Considerations

Two forms of shear behavior act within concrete columns that are, and must be appropriately treated as, separate facets: diagonal and direct shear.

Diagonal shear works in conjunction with flexure and has been observed to weaken the resistance of concrete members. Referenced in section 2.3, diagonal shear supplements crack propagation to produce an inarguable effect on the failure criteria of beam and column members. An estimate of this effect is proposed by Krauthammer and Shahriar (1988) via a shear reduction factor. The SRF is applied to a member's moment capacity, effectively shifting the moment-curvature diagram downwards. The factor is based on the reinforcement and shear span to depth ratios, and since the longitudinal reinforcement remains unchanged through the various NSC and UHPC column trials, the SRF remains constant. In each of the presented cases the SRF employed is 0.77, and the Table 4-12 exemplifies the effect held by this factor on the column's peak response.

Direct shear operates as a separate failure mode, juxtaposed to the flexural failure focused upon in the study. Direct shear is noted by cracking perpendicular to a member's axis, typical in areas of high concentrated shear force, i.e. under the supports or point loads. DSAS considers the incurrence of direct shear and its peak behavior for several of the blast trials presented in Table 4-13. It is observed that for all trials, except the UHPC subjected to a 1777 psi pressure, direct shear failure is indicated.

4.5.3 Tension Membrane Behavior

After a structural member sufficiently cracks to dissipate the strength contribution of the concrete, the steel reinforcement begins to act as a tension membrane. The study formerly conducted by Morency (2010) chronicled the adaption of DSAS to account for tension membrane action in reinforced concrete columns under severe dynamic loads. Table 4-14 now compares the effects of including the tension membrane strength in computations for the NSC and UHPC columns. For the simply supported spans, as the

deformation grows the counteraction of the membrane logically increases as well. The ductility and durability of UHPC is also observed by the lesser effect held by the membrane action compared with its impact on the NSC columns. For fixed columns, the membrane does not enact for the smaller blast loads, but it begins to contribute greater support as the blasts more severely increase the column deformation.

4.6 Summary

An analytical study of the severe deformation of normal strength and ultra high performance concrete columns has been presented. The primary focus was to demonstrate the theory of plastic hinge formation through the computational DSAS V3.2.1 and ABAQUS V6-10 programs. Sections 4.2 and 4.3 evaluated the behaviors of NSC and UHPC columns respectively, exploring the single and multiple hinge generations inherent of simply supported and fixed columns. A thorough comparison of the two concrete types then proceeded in section 4.4, followed by the reemphasis of particular inelastic behaviors, including the calculation of a column's plastic hinge length, in section 4.5.

Table 4-1. Dynamic increase factors for the NSC column.

Blast trial	Concrete in compression, f'_c	Concrete in tension, f_t	Reinforcing steel, f_y and f_u
1	1.29	2.64	1.20
2	1.31	2.82	1.21
3	1.32	2.90	1.22
4	1.32	2.97	1.22
5	1.33	3.03	1.23

Table 4-2. Simply supported NSC column response.

Trial	Uniform pressure (psi)	DSAS (in)	ABAQUS (in)	Percent difference (%)
NS1	1777	2.69	2.20	22.2
NS2	2922	5.72	5.72	0.0
NS3	3602	8.03	8.79	8.6
NS4	4208	10.35	13.71	24.5
NS5	4757	12.64	19.15	34.0

Table 4-3. Fixed support NSC column response.

Trial	Uniform pressure (psi)	DSAS (in)	ABAQUS (in)	Percent difference (%)
NF1	1777	1.82	1.09	67.0
NF2	2922	4.28	3.70	15.7
NF3	3602	6.50	6.72	3.3
NF4	4208	9.16	10.79	15.1
NF5	4757	11.84	15.30	22.6

Table 4-4. NSC response to combinations of blast and axial loads.

Trial	Uniform pressure (psi)	0 kip (in)	750 kip (in)	1250 kip (in)	1750 kip (in)
NS1	1777	2.69	1.59	1.76	3.15
NS3	3602	8.03	5.55	6.22	8.65
NS5	4757	12.64	9.37	9.89	13.24
NF1	1777	1.82	1.43	1.76	3.15
NF3	3602	6.50	5.68	6.13	8.68
NF5	4757	11.84	9.88	10.25	13.34

Table 4-5. DSAS input of UHPC's properties.

Concrete properties	Values	Steel properties	Values
Compression		Comp/Tension	
E_c (ksi)	5950	E_s (ksi)	29520
$\varepsilon_{y,c1}$ (in/in)	0.004	ε_y (in/in)	0.00156
ε_{c2} (in/in)	0.006	f_y (psi)	0.0144
f_{max} (psi)	23800	ε_{sh} (in/in)	90000
ε_u (in/in)	0.01	ε_u (in/in)	0.15
f_u (psi)	20300	f_u (psi)	0.15
Tension			
ε_y (in/in)	0.0003		
f_y (psi)	1300		
ε_2 (in/in)	0.0015		
f_2 (psi)	1600		
ε_3 (in/in)	0.0055		
f_3 (psi)	362		
ε_u (in/in)	0.0125		

Table 4-6. Simply supported UHPC column response.

Trial	Uniform pressure (psi)	DSAS (in)	ABAQUS (in)	Percent difference (%)
US1	1777	2.24	1.97	13.7
US2	2922	4.70	4.96	5.2
US3	3602	6.78	7.93	14.5
US4	4208	8.89	10.87	18.2
US5	4757	11.09	17.73	37.5

Table 4-7. Fixed support UHPC column response.

Trial	Uniform pressure (psi)	DSAS (in)	ABAQUS (in)	Percent difference (%)
UF1	1777	1.42	0.79	80.0
UF2	2922	3.22	1.93	66.8
UF3	3602	4.78	4.37	9.4
UF4	4208	6.69	8.40	20.4
UF5	4757	9.29	12.08	23.1

Table 4-8. UHPC response to combinations of blast and axial loads.

Trial	Uniform pressure (psi)	0 kip (in)	1750 kip (in)	3750 kip (in)	5750 kip (in)
US1	1777	2.24	1.08	1.00	2.29
US3	3602	6.78	3.12	3.05	7.20
US5	4757	11.09	7.00	5.33	11.66
UF1	1777	1.42	0.55	0.73	2.22
UF3	3602	4.78	2.72	2.89	7.29
UF5	4757	9.29	5.25	5.40	11.83

Table 4-9. Comparison of NSC and UHPC test columns – DSAS peak response.

Blast trial	Simple NSC (in)	Simple UHPC (in)	Fixed NSC (in)	Fixed UHPC (in)
1	2.69	2.24	1.82	1.42
2	5.72	4.70	4.28	3.22
3	8.03	6.78	6.50	4.78
4	10.35	8.89	9.16	6.69
5	12.64	11.09	11.84	9.29

Table 4-10. Comparison of NSC and UHPC test columns – ABAQUS peak response.

Blast trial	Simple NSC (in)	Simple UHPC (in)	Fixed NSC (in)	Fixed UHPC (in)
1	2.20	1.97	1.09	0.79
2	5.72	4.96	3.70	1.93
3	8.79	7.93	6.72	4.37
4	13.71	10.87	10.79	8.40
5	19.15	17.73	15.30	12.08

Table 4-11. Effect on plastic hinge length expressions.

Expression	Control: NSC column	Increase span to 14 feet	Increase rebar cover to 3 in.	Decrease column depth to 12 in.
Corley	11.0	11.7	10.5	9.7
Mattock	10.9	11.5	10.1	8.9
Sawyer	9.0	9.9	8.7	8.0
Paulay & Priestly	17.6	19.5	17.6	17.6
Sheikh & Khoury	16.0	16.0	16.0	12.0
Average (of above)	*12.9*	*13.7*	*12.6*	*11.2*
Effective Depth	13.0	13.0	10.0	9.0

Table 4-12. Effect of diagonal shear.

Trial	With SRF (in)	Without SRF (in)	Trial	With SRF (in)	Without SRF (in)
NS1	2.69	2.17	US1	2.24	1.77
NS4	10.35	9.10	US4	8.89	7.59
NF1	1.82	1.40	UF1	1.42	1.12
NF4	9.16	7.20	UF4	6.69	5.84

Table 4-13. Direct shear response.

Column type	1777 psi (in)	2922 psi (in)	3608 psi (in)	4208 psi (in)	4757 psi (in)
Simple NSC	0.45_{Fail}	0.44_{Fail}	0.44_{Fail}	0.42_{Fail}	0.43_{Fail}
Fixed NSC	0.45_{Fail}	0.44_{Fail}	0.44_{Fail}	0.43_{Fail}	0.43_{Fail}
Simple UHPC	0.67	1.05_{Fail}	1.05_{Fail}	1.05_{Fail}	1.05_{Fail}
Fixed UHPC	0.67	1.05_{Fail}	1.05_{Fail}	1.04_{Fail}	1.05_{Fail}

Table 4-14. Effect of tension membrane behavior.

Normal Strength Concrete			Ultra High Performance Concrete		
Trial	Consider TM (in)	Without TM (in)	Trial	Consider TM (in)	Without TM (in)
NS1	2.69	3.61	US1	2.24	2.55
NS2	5.72	8.24	US2	4.70	5.80
NS3	8.03	12.44	US3	6.78	8.70
NS4	10.35	17.30	US4	8.89	10.34_{Fail}
NS5	12.64	22.74	US5	11.09	13.74_{Fail}
NF1	1.82	1.40	UF1	1.42	1.42
NF2	4.28	4.28	UF2	3.22	3.22
NF3	6.50	6.50	UF3	4.78	4.78
NF4	9.16	9.08	UF4	6.69	6.97
NF5	11.84	12.06	UF5	9.29	11.12

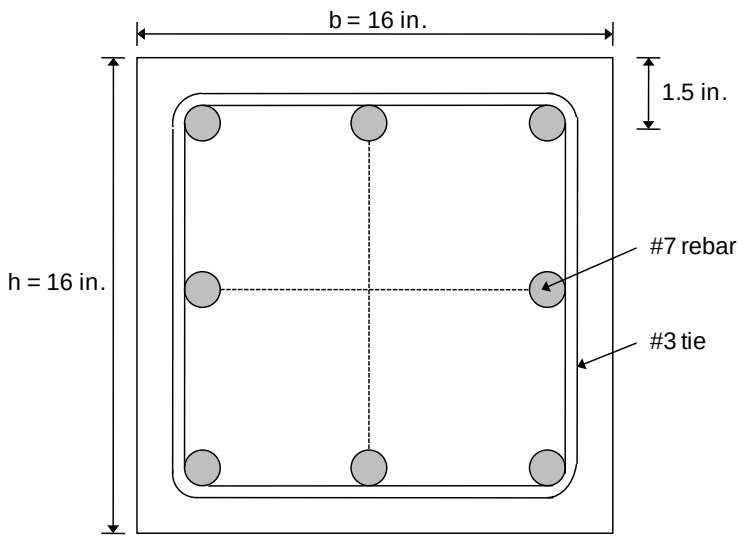

Figure 4-1. Cross-section of test column.

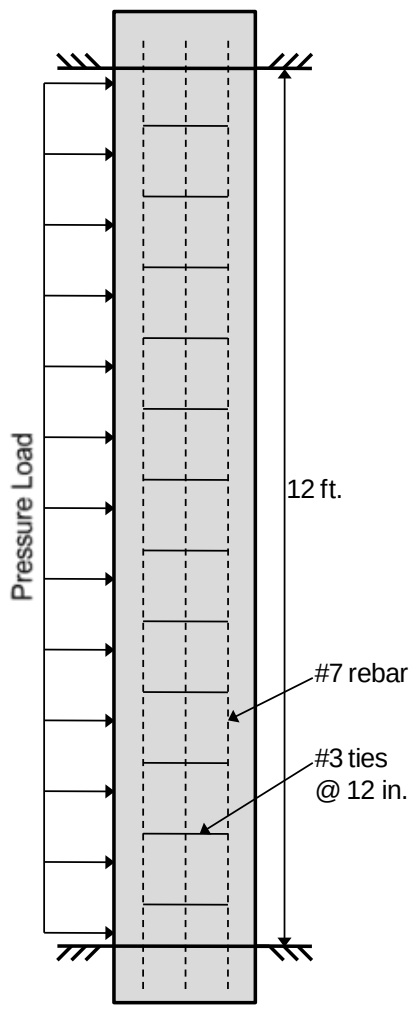

Figure 4-2. Schematic of test column span.

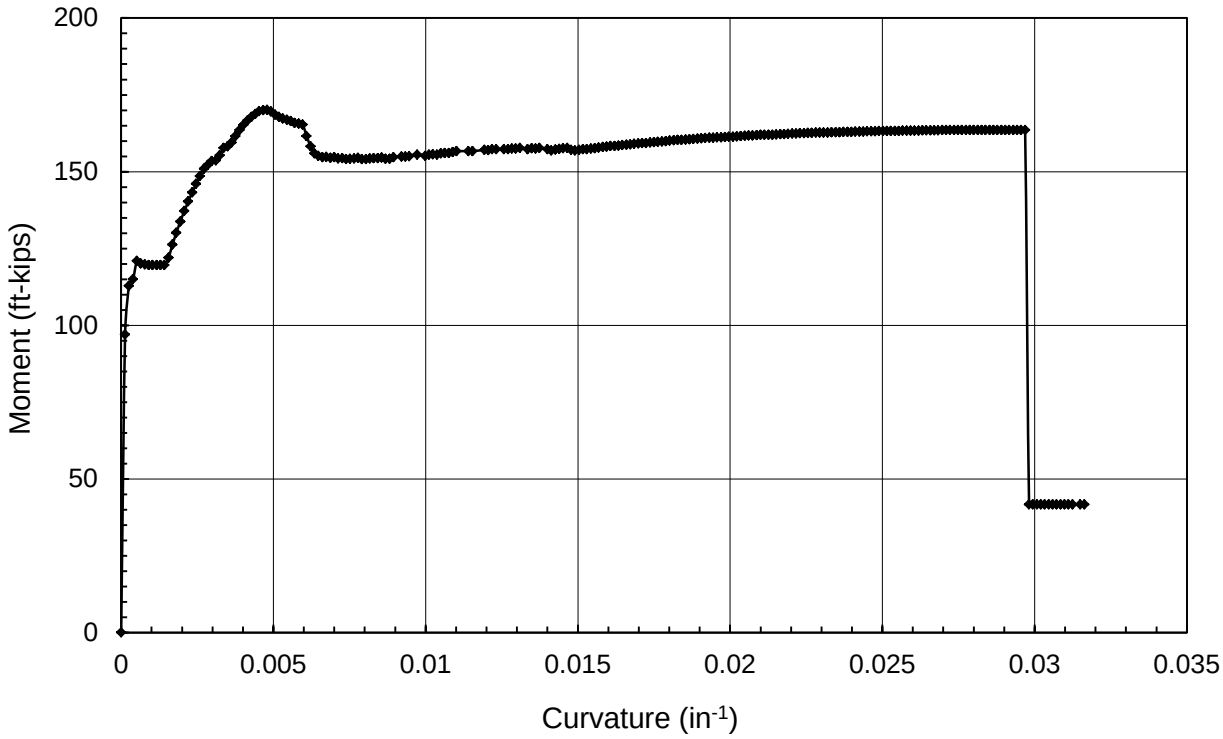

Figure 4-3. Moment-curvature of NSC column.

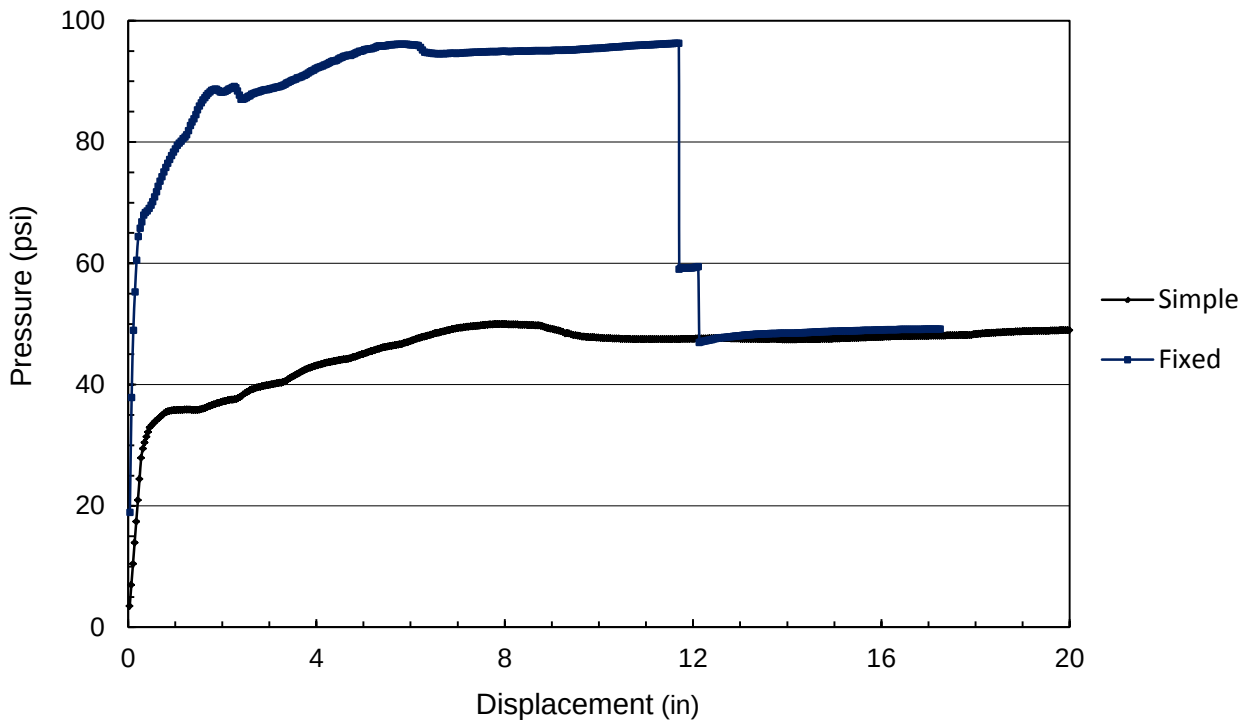

Figure 4-4. Load-deflection curves of NSC column.

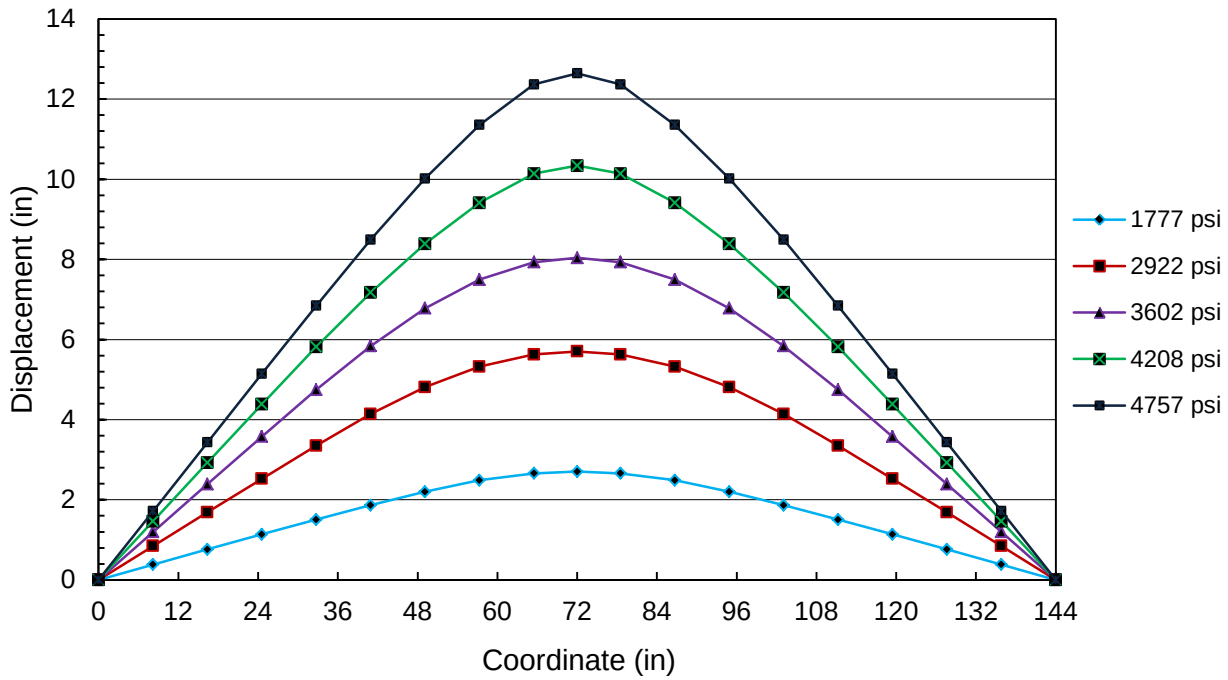

Figure 4-5. Progression of deformation of simply supported NSC column.

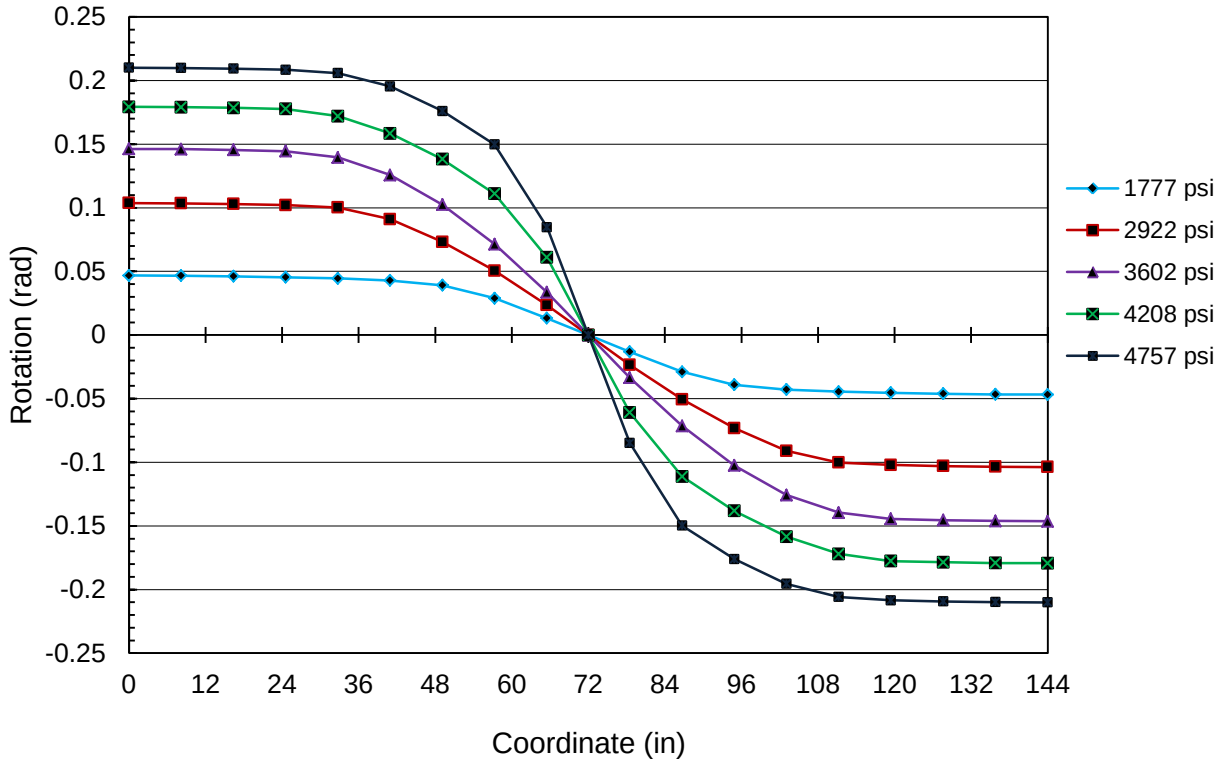

Figure 4-6. Progression of rotation of simply supported NSC column.

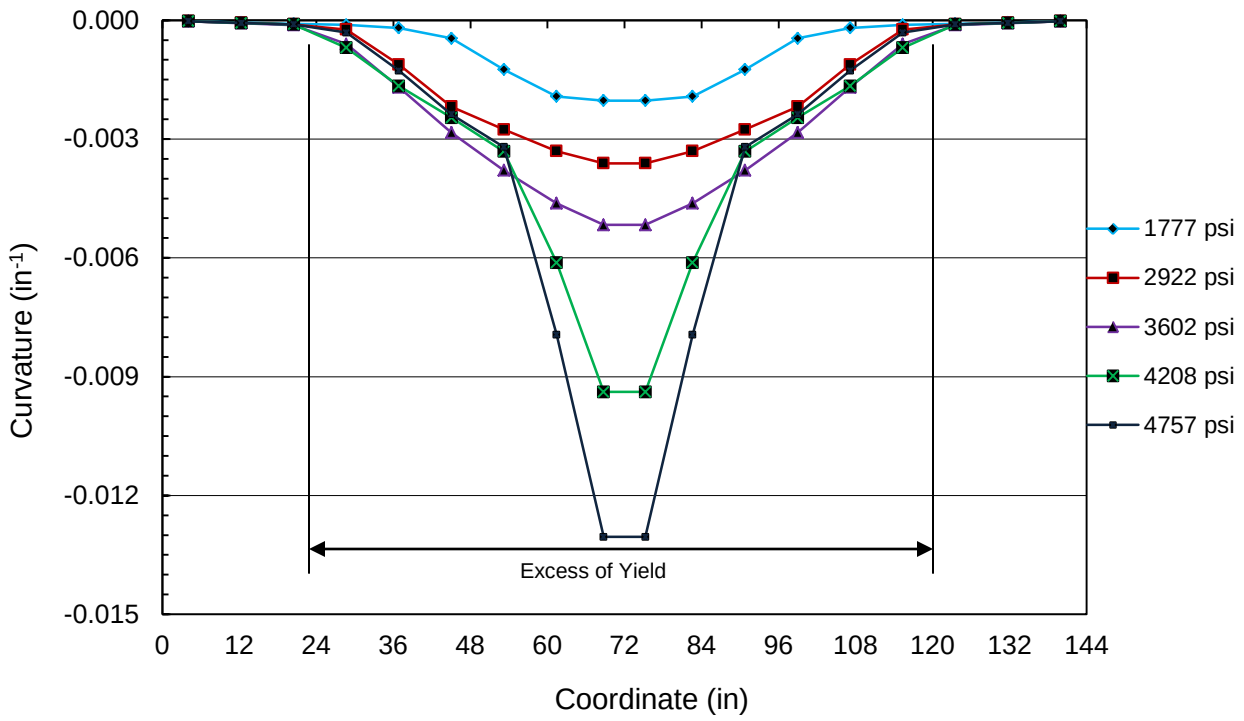

Figure 4-7. Progression of curvature of NSC simply supported column.

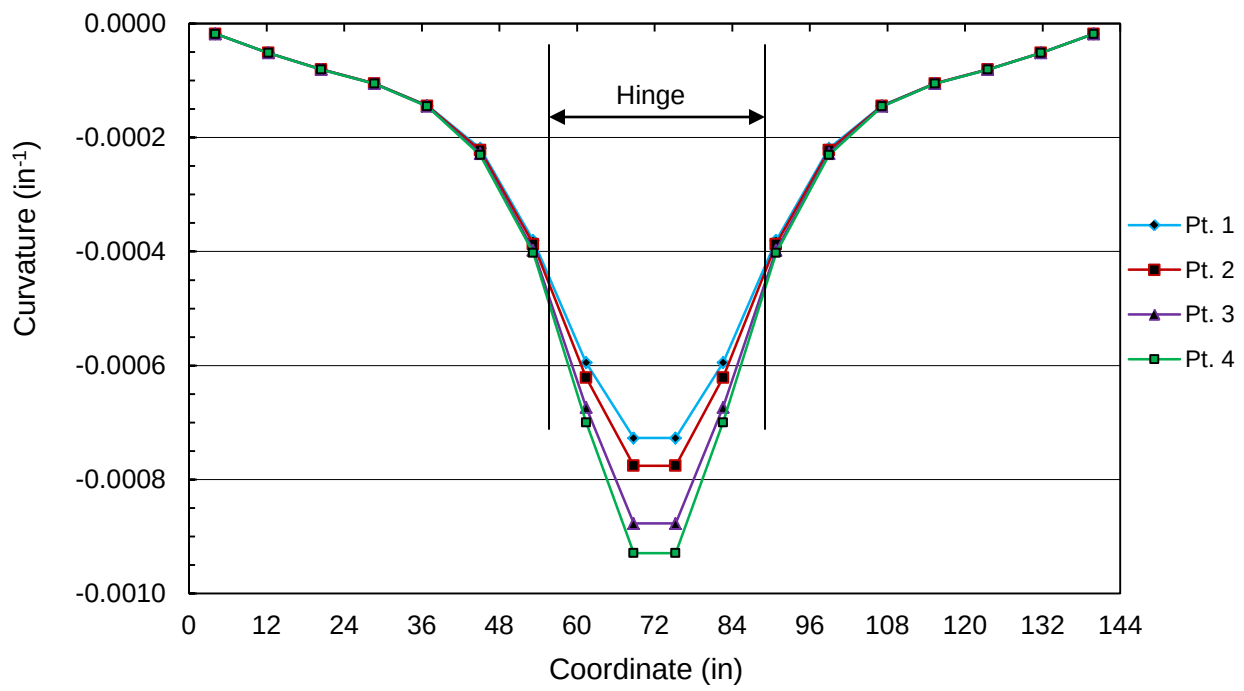

Figure 4-8. Curvature of simply supported NSC column post-yield.

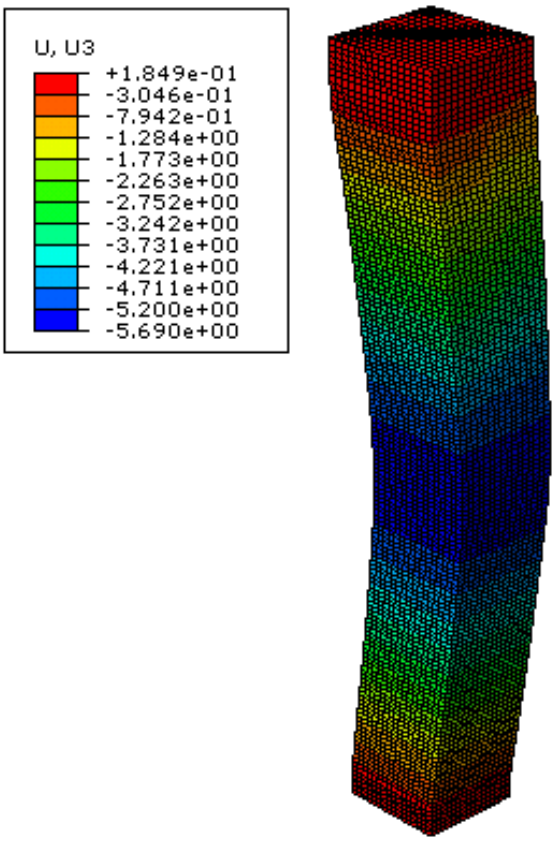

Figure 4-9. Example of ultimate deformation via ABAQUS (trial NS2).

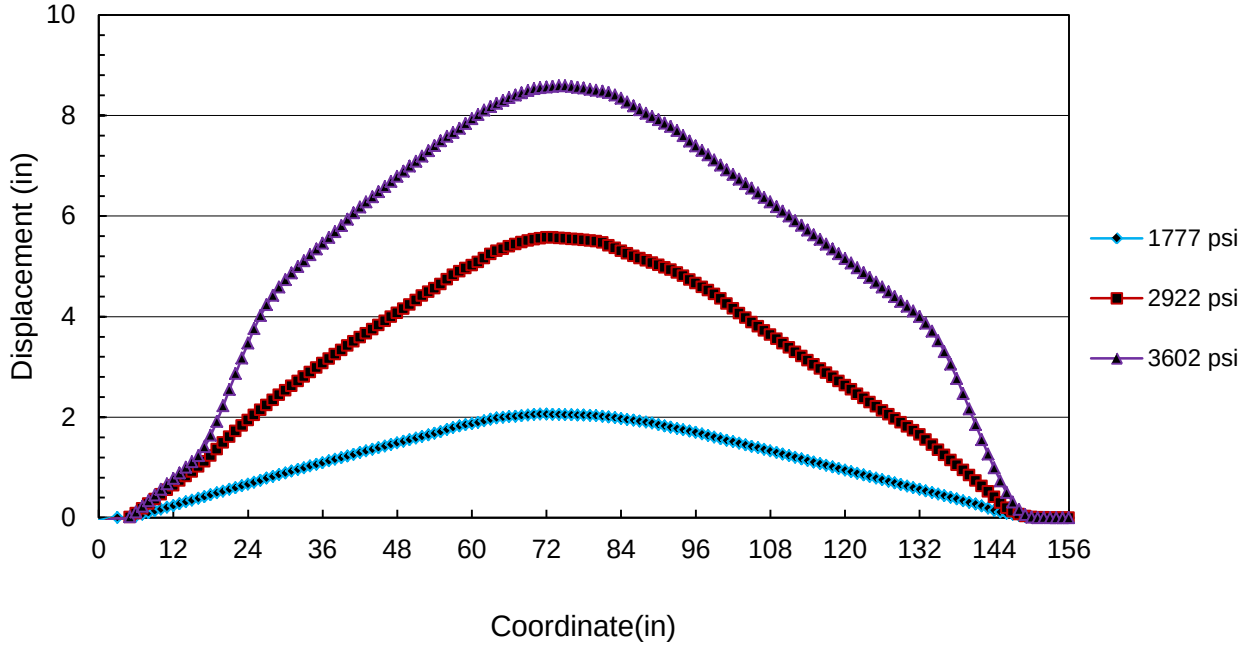

Figure 4-10. ABAQUS deflected shapes for simply supported NSC column.

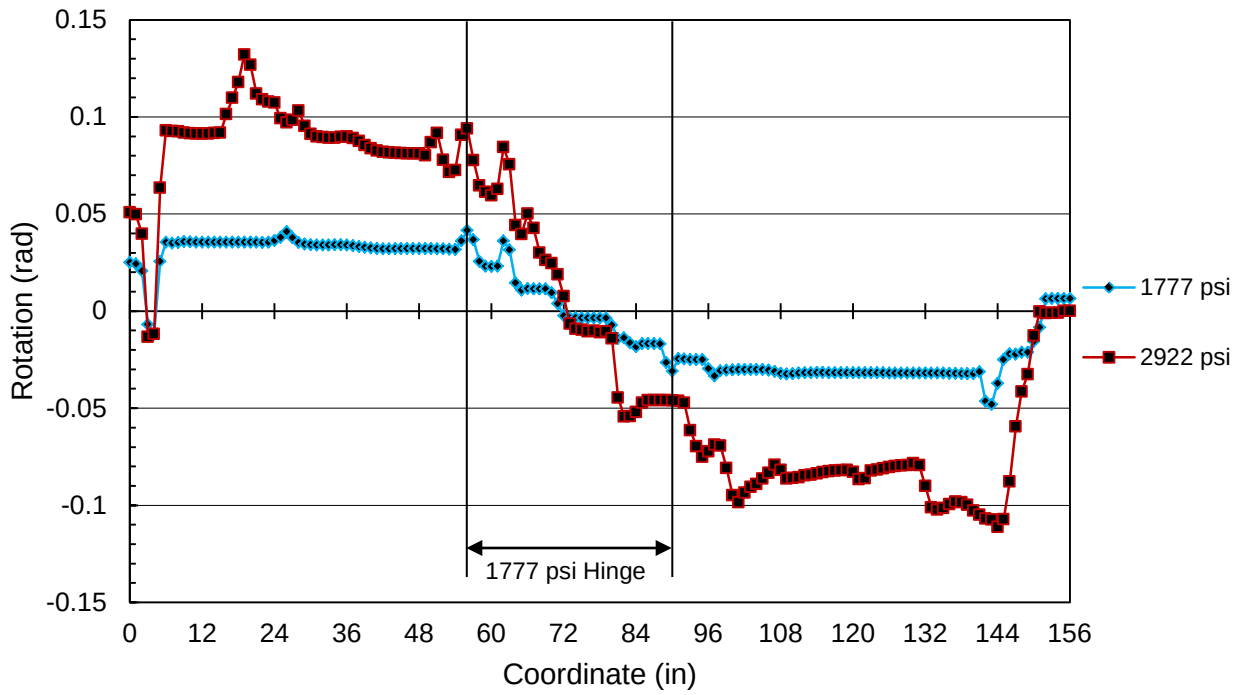

Figure 4-11. ABAQUS rotations for simply supported NSC column.

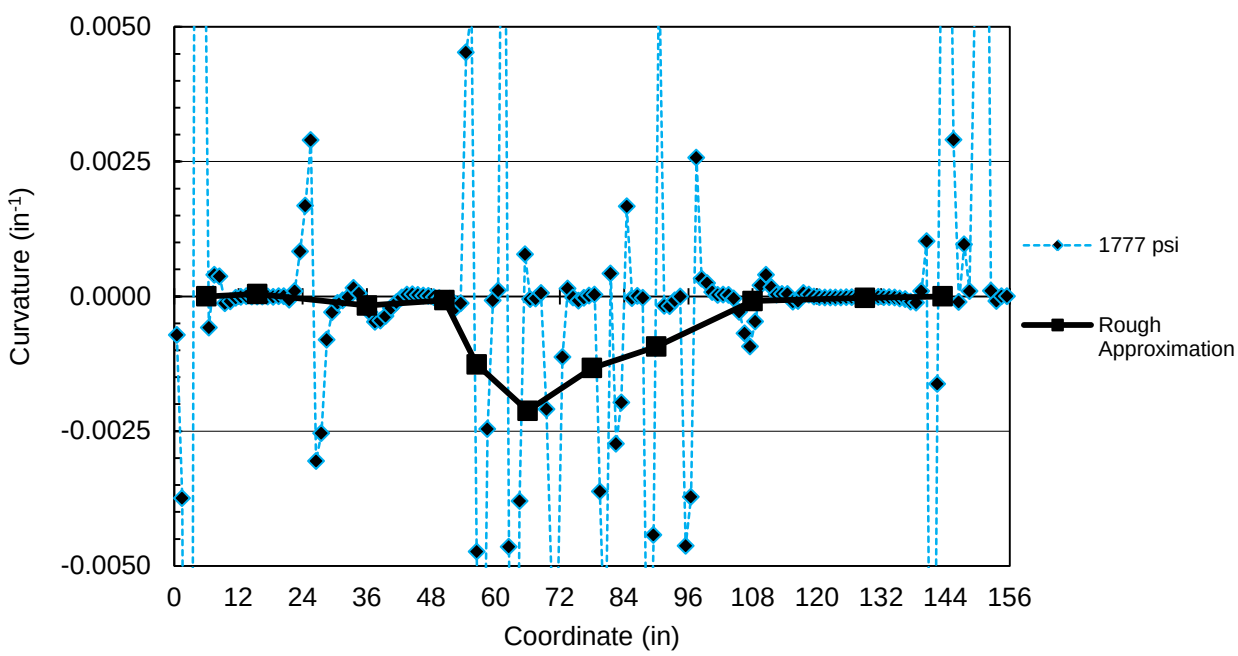

Figure 4-12. ABAQUS curvature for simply supported NSC column.

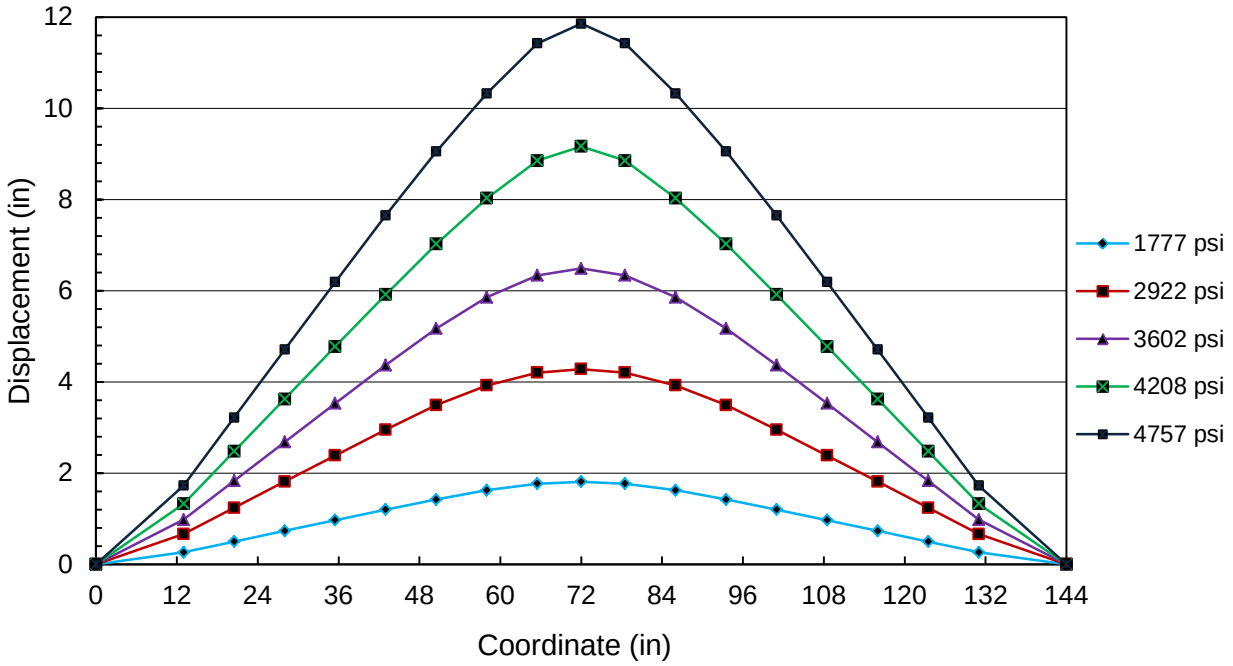

Figure 4-13. Progression of deformation of fixed NSC column.

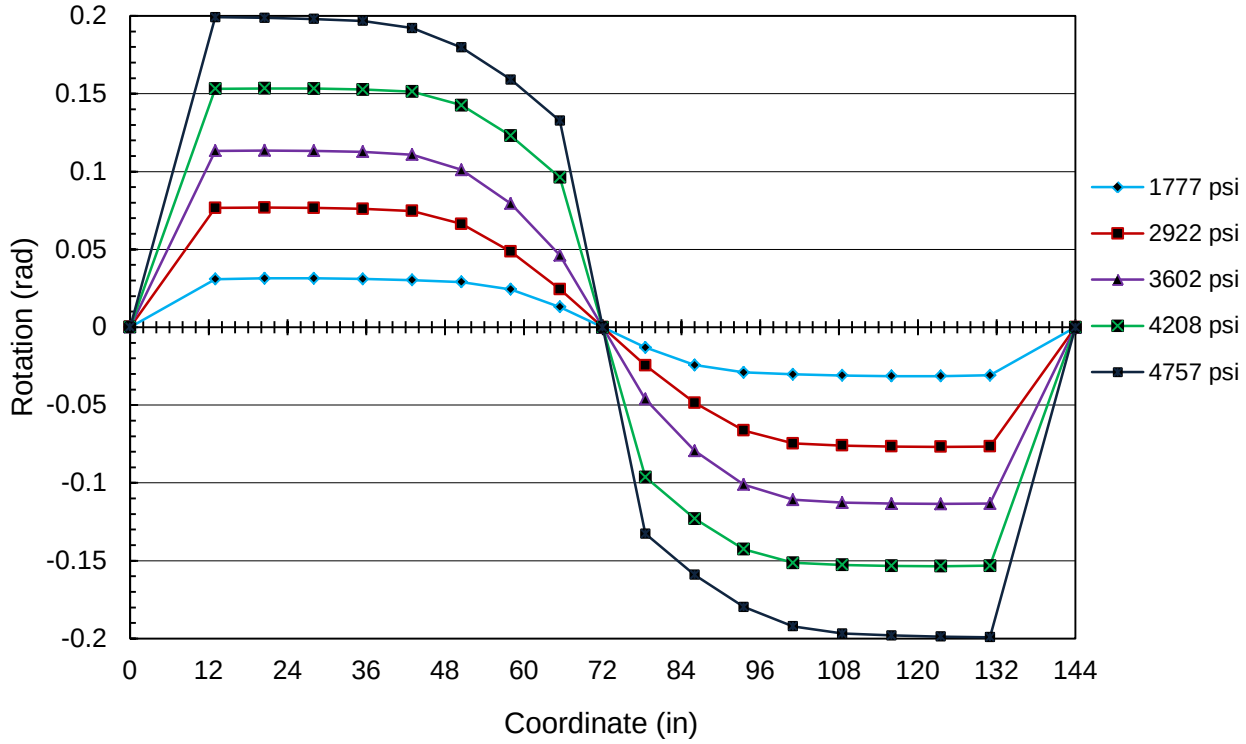

Figure 4-14. Progression of rotation of fixed NSC column.

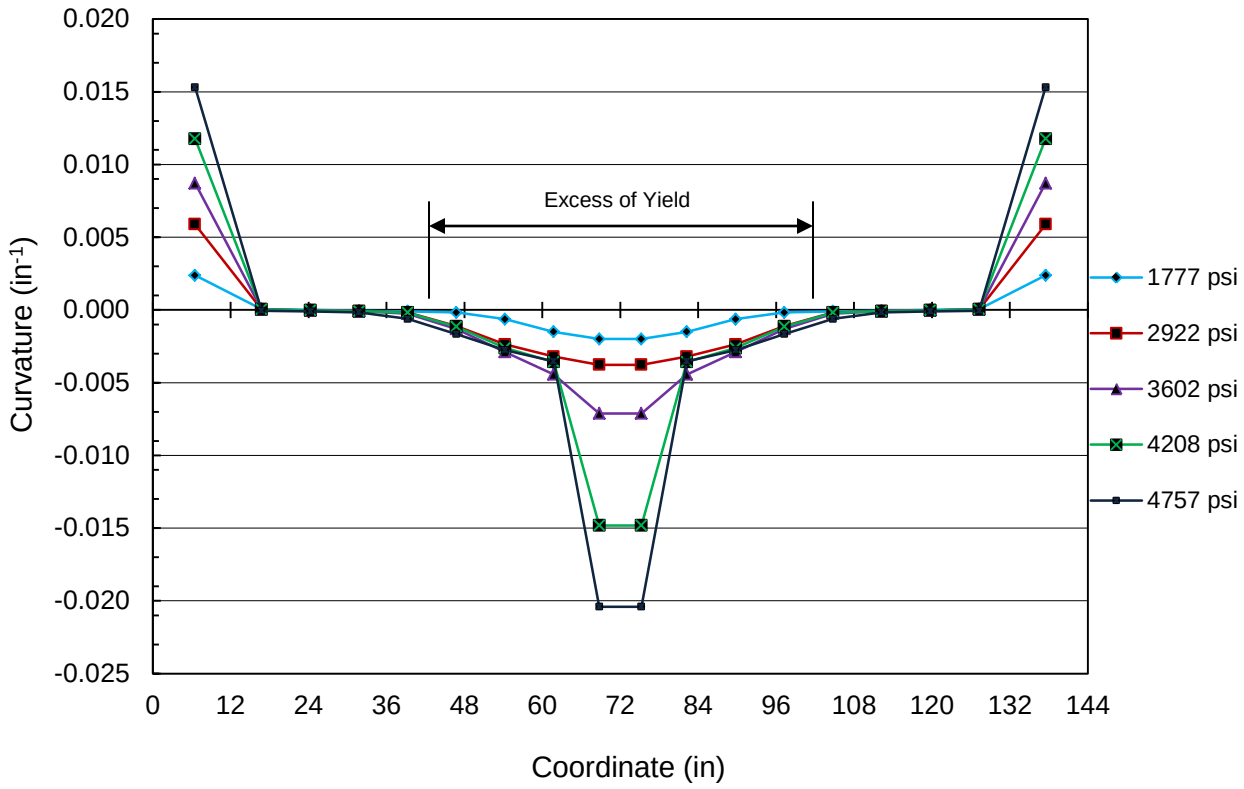

Figure 4-15. Progression of curvature of fixed NSC column.

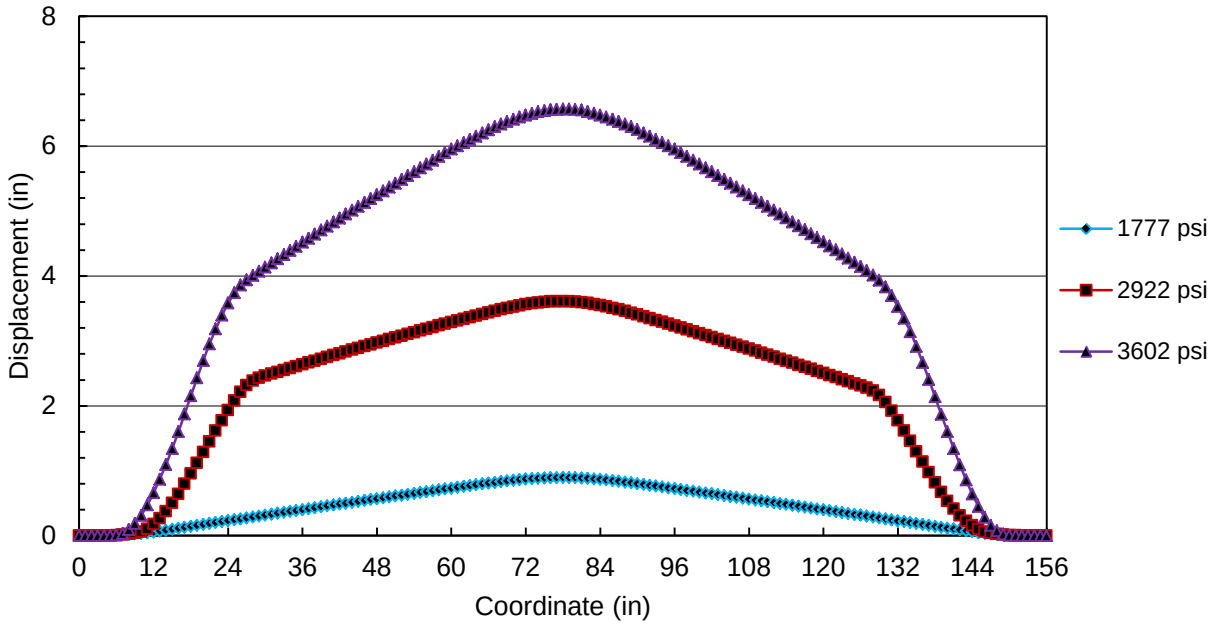

Figure 4-16. ABAQUS deflected shapes for fixed NSC column.

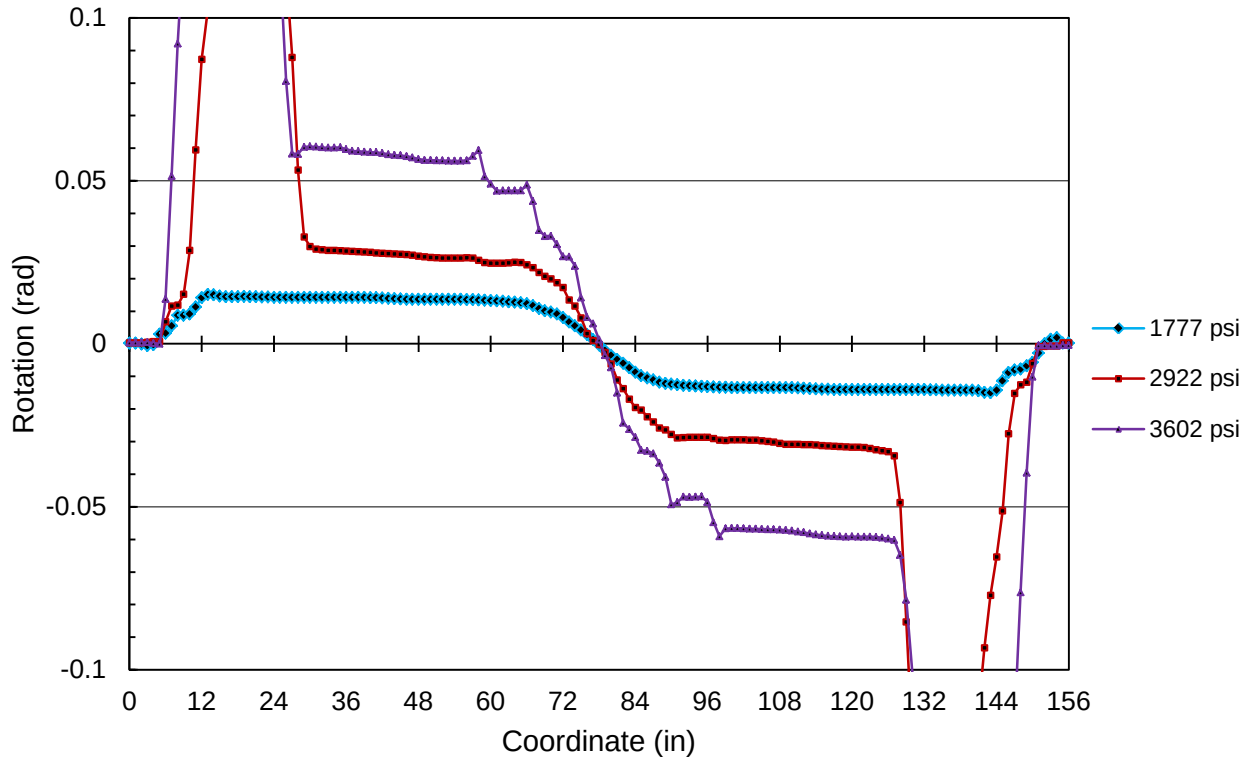

Figure 4-17. ABAQUS rotations for fixed NSC column.

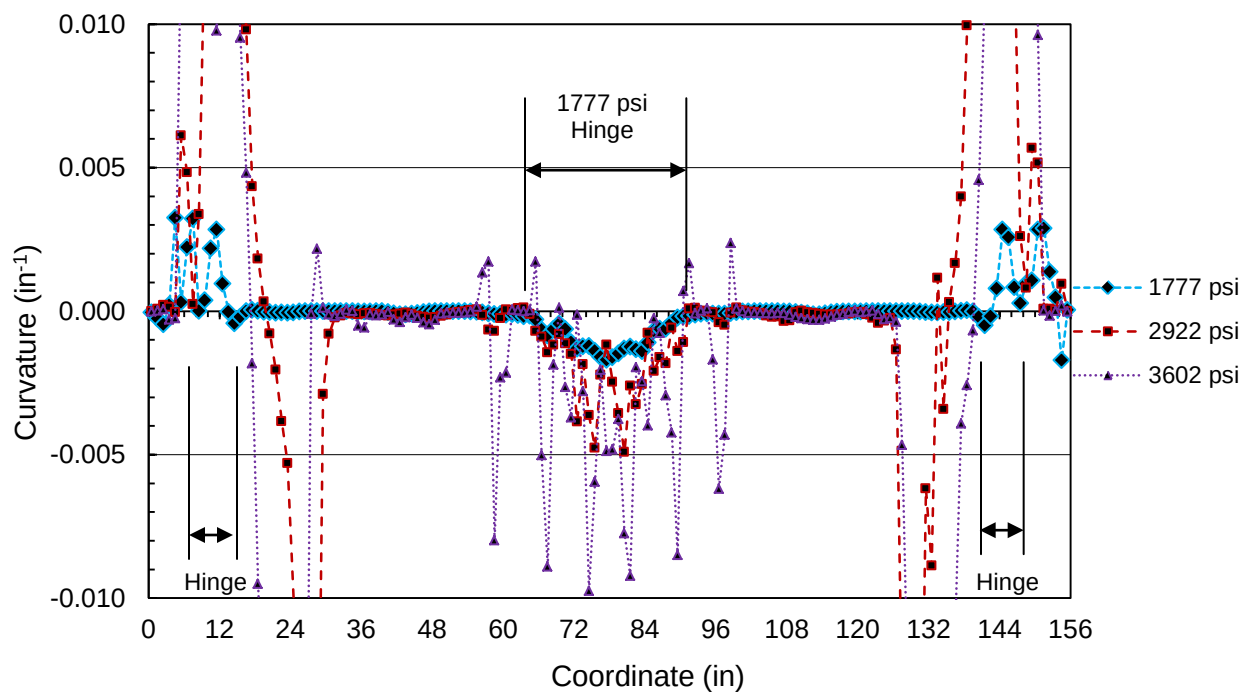

Figure 4-18. ABAQUS curvatures for fixed NSC column.

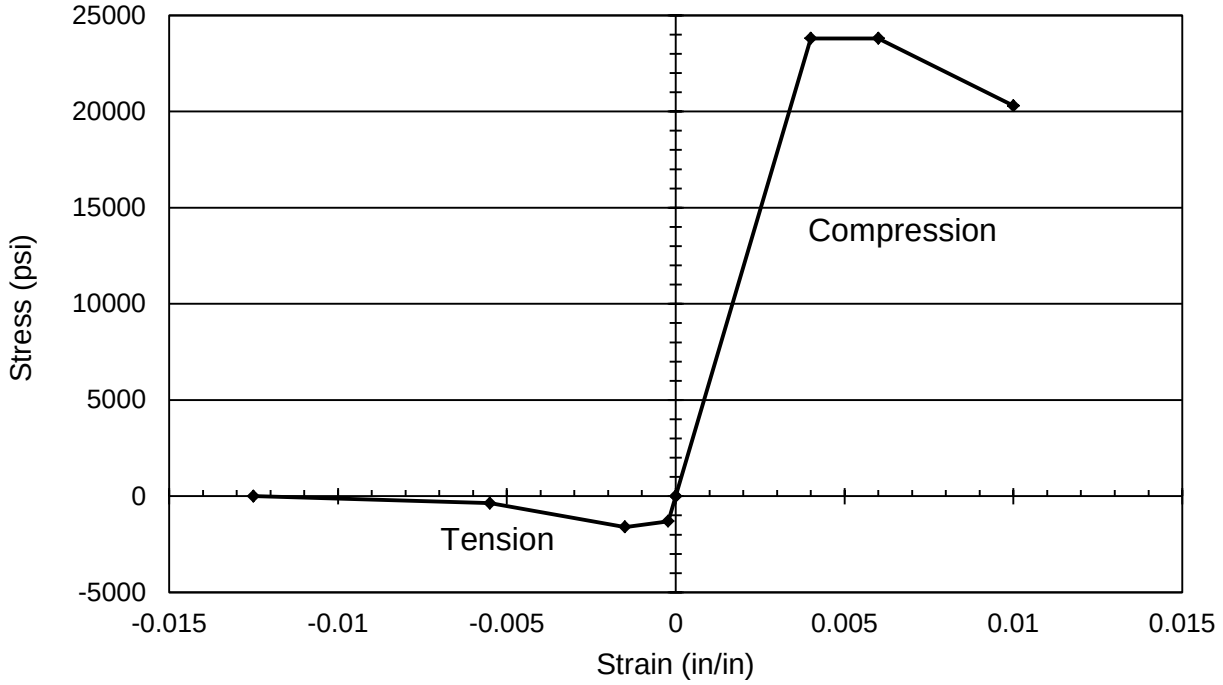

Figure 4-19. UHPC material model.

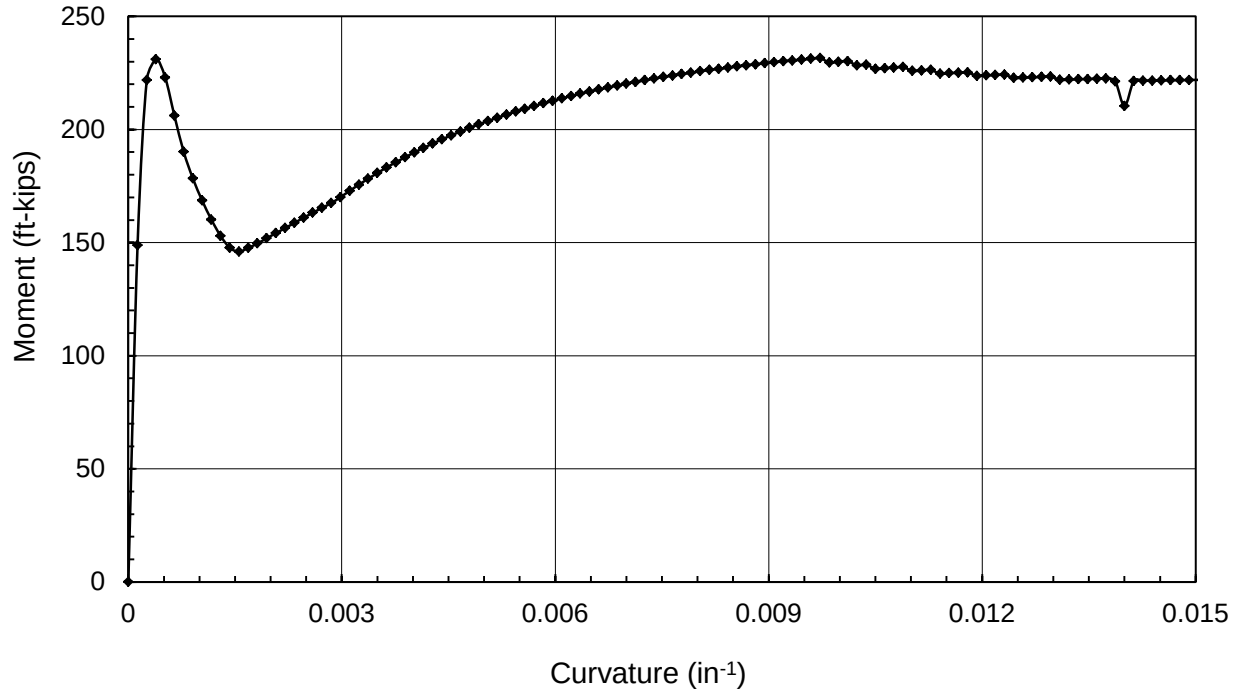

Figure 4-20. Moment-curvature diagram for UHPC column.

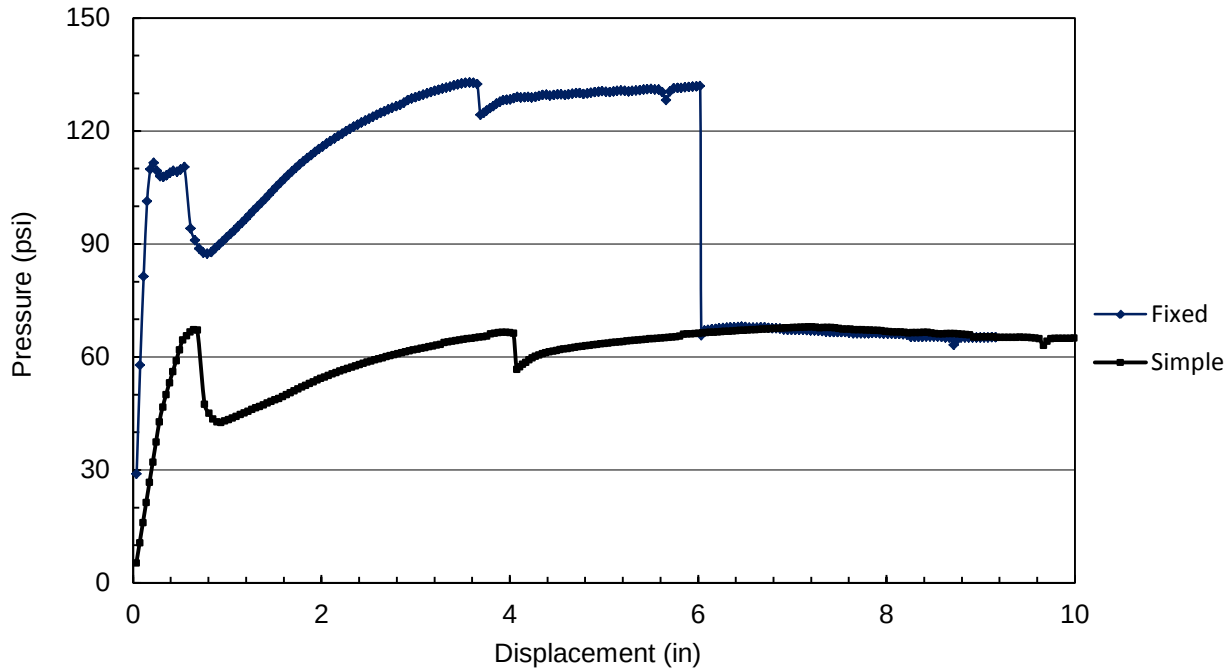

Figure 4-21. Load-deflection curves of UHPC column.

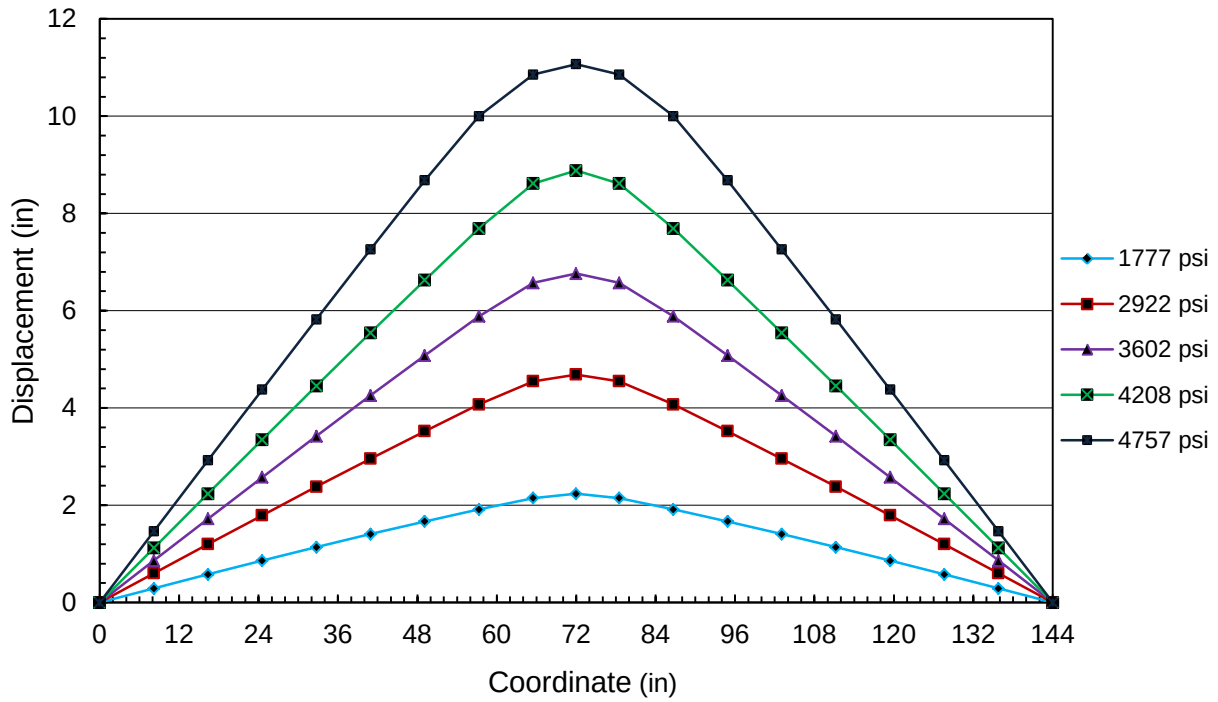

Figure 4-22. Progression of deformation of simply supported UHPC column.

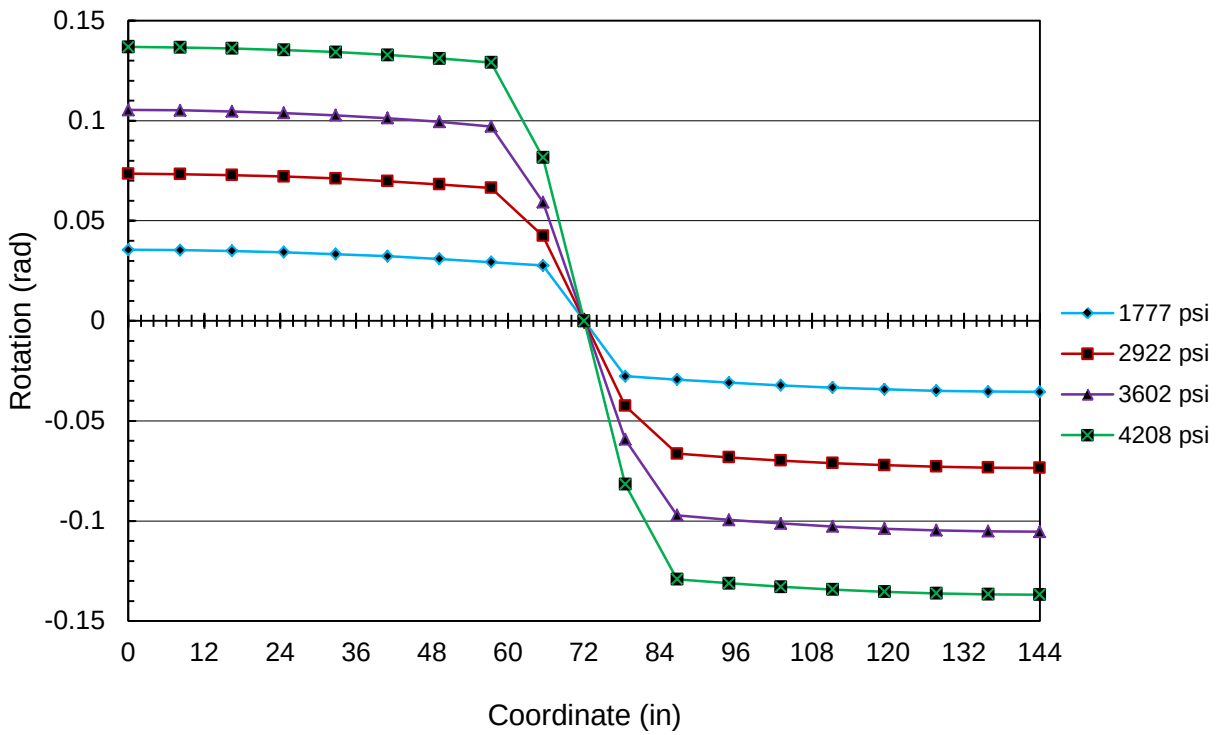

Figure 4-23. Progression of rotation of simply supported UHPC column.

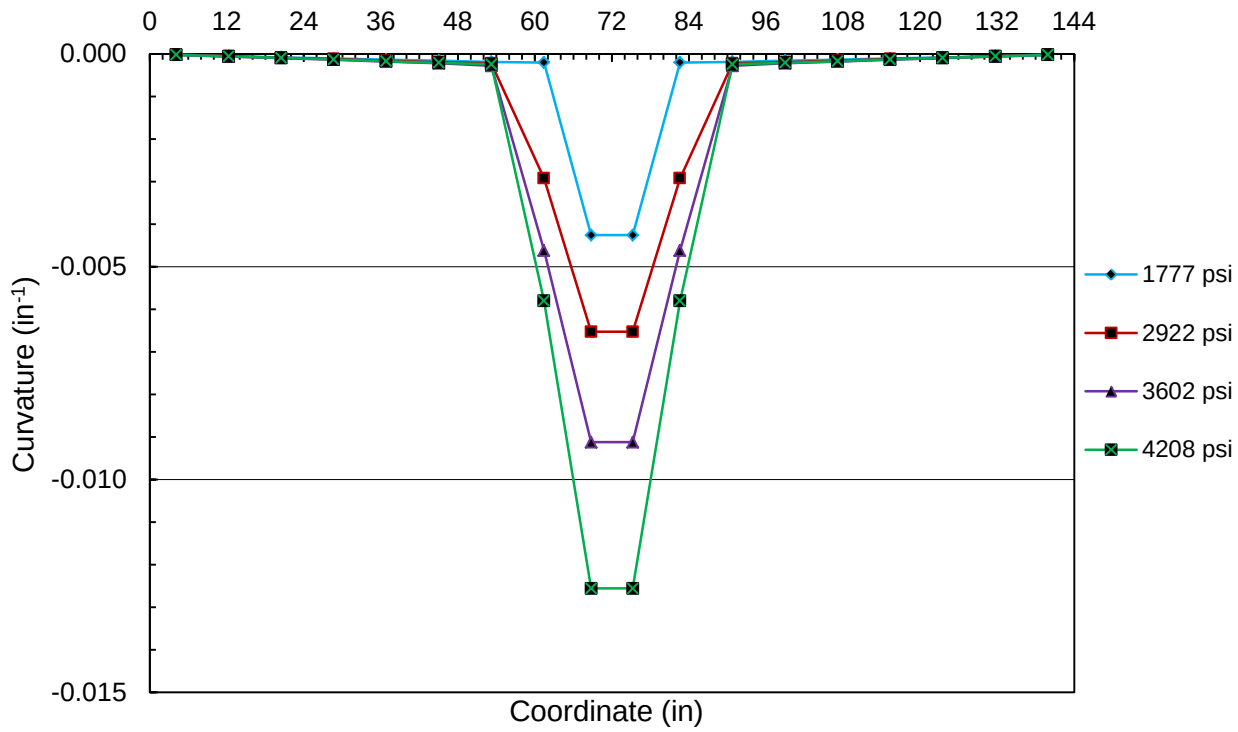

Figure 4-24. Progression of curvature of simply supported UHPC column.

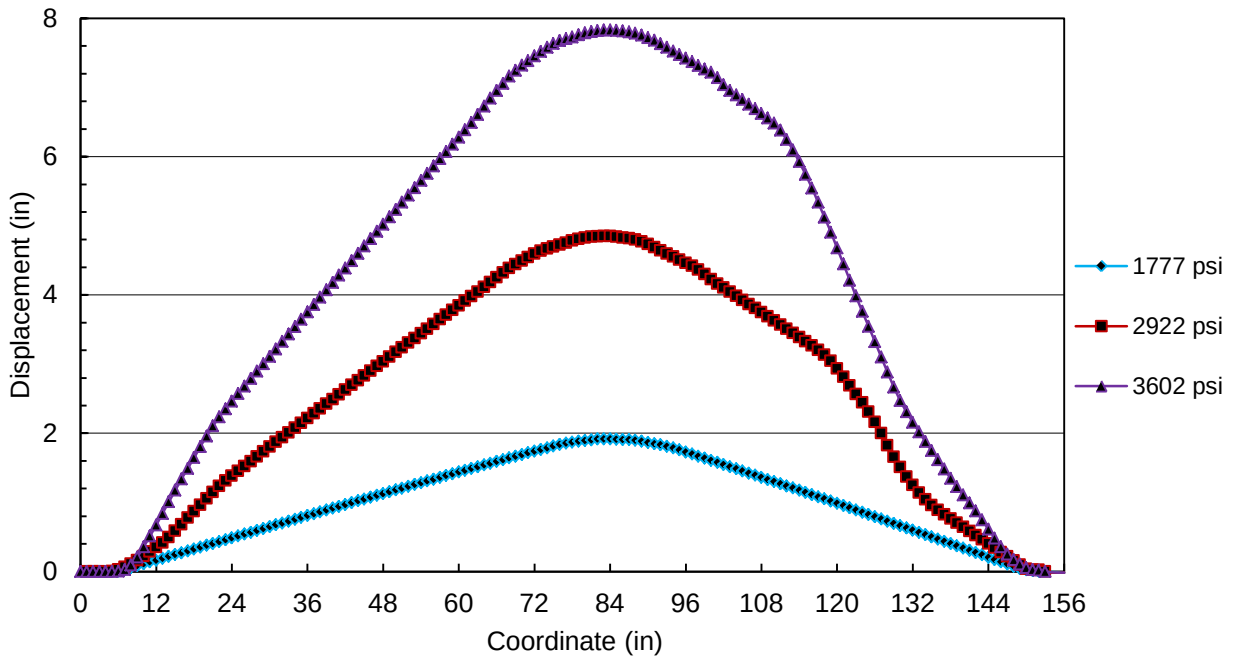

Figure 4-25. ABAQUS deflected shapes of simply supported UHPC column.

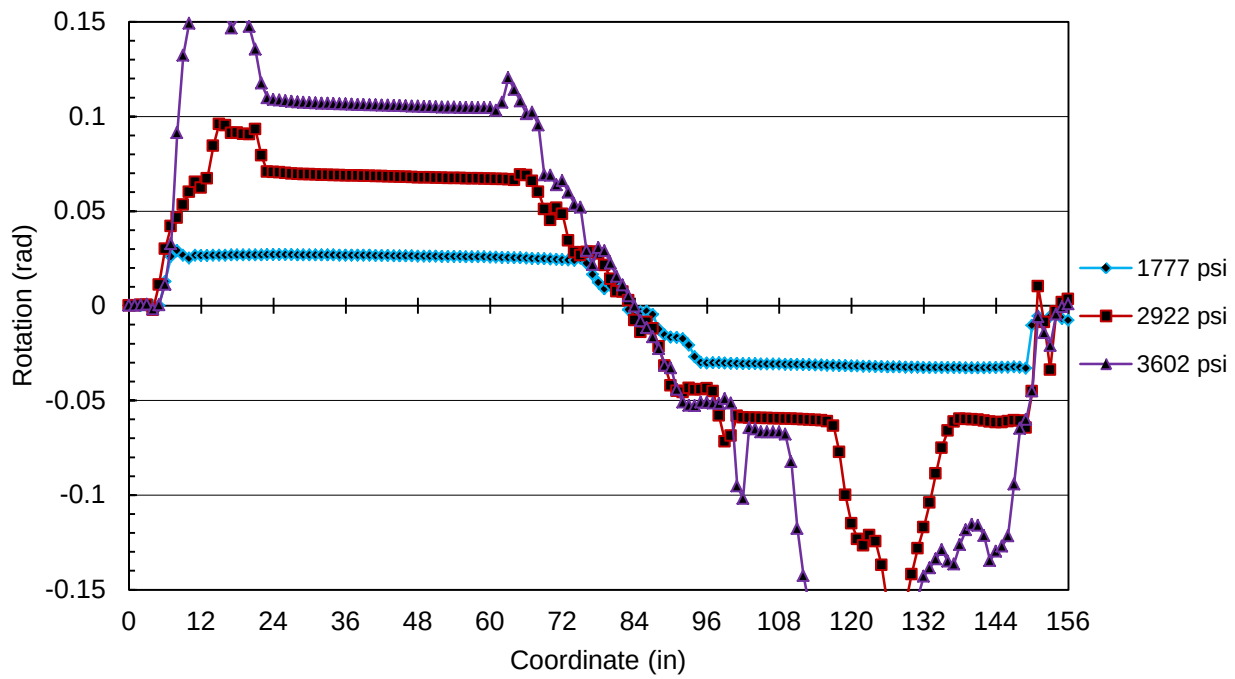

Figure 4-26. ABAQUS rotations of simply supported UHPC column.

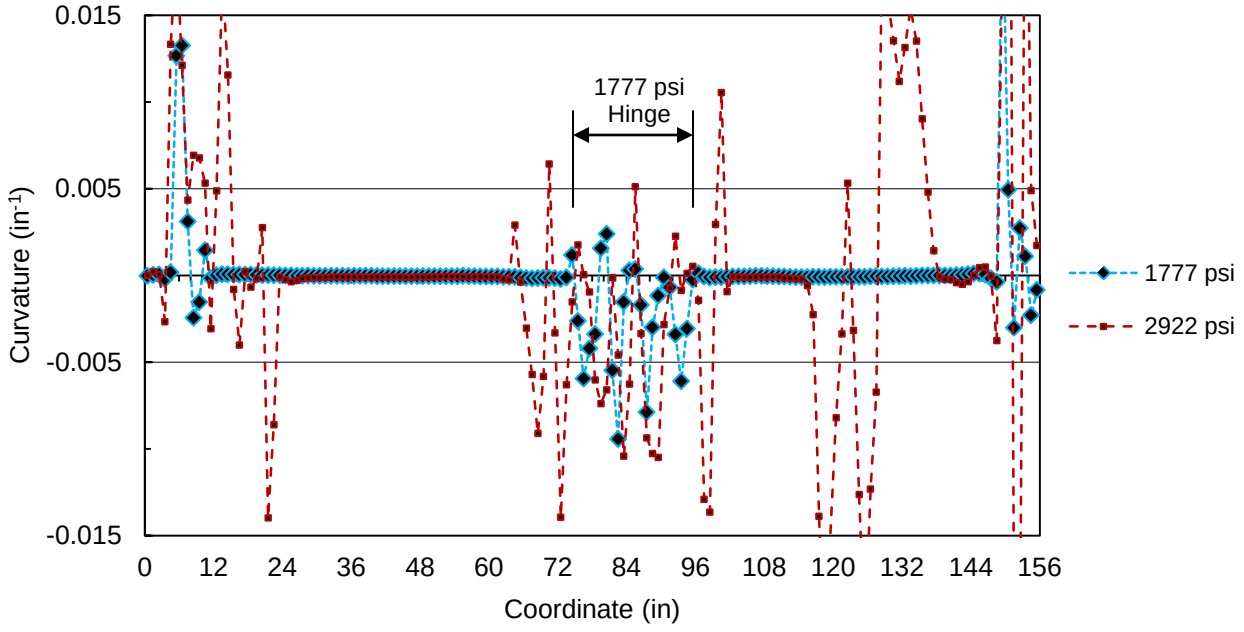

Figure 4-27. ABAQUS curvatures of simply supported UHPC column.

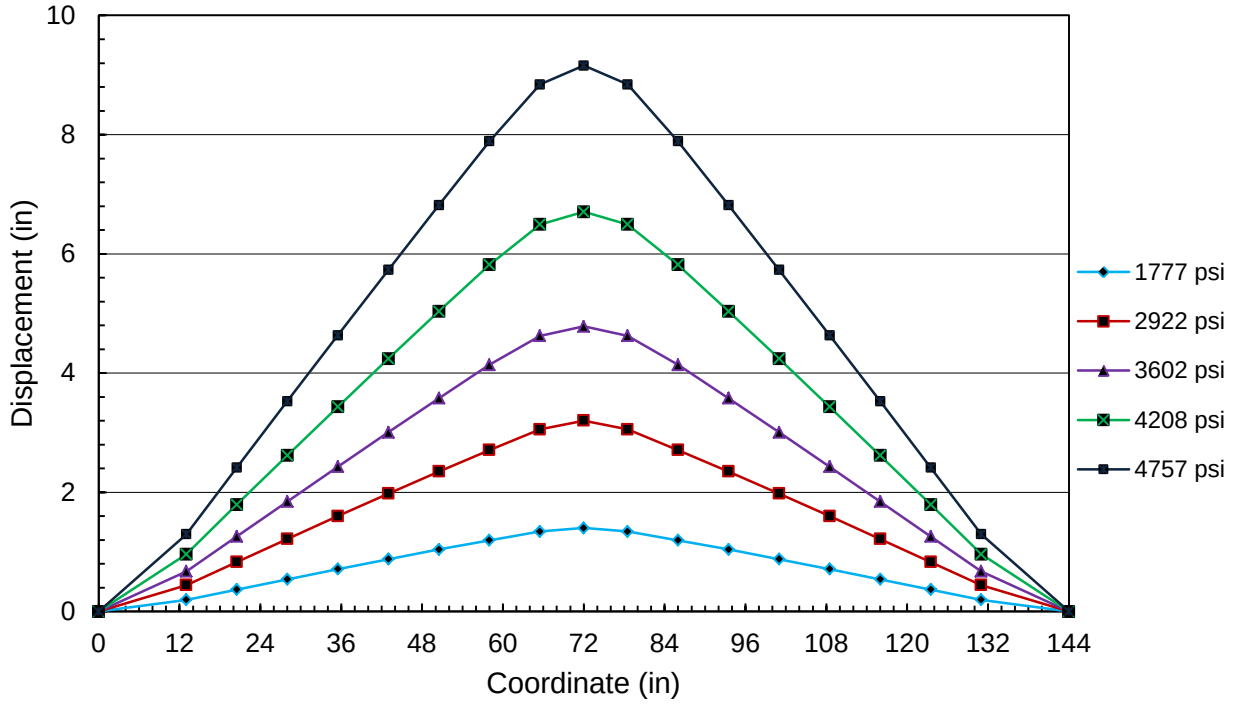

Figure 4-28. Progression of deformation of fixed UHPC column.

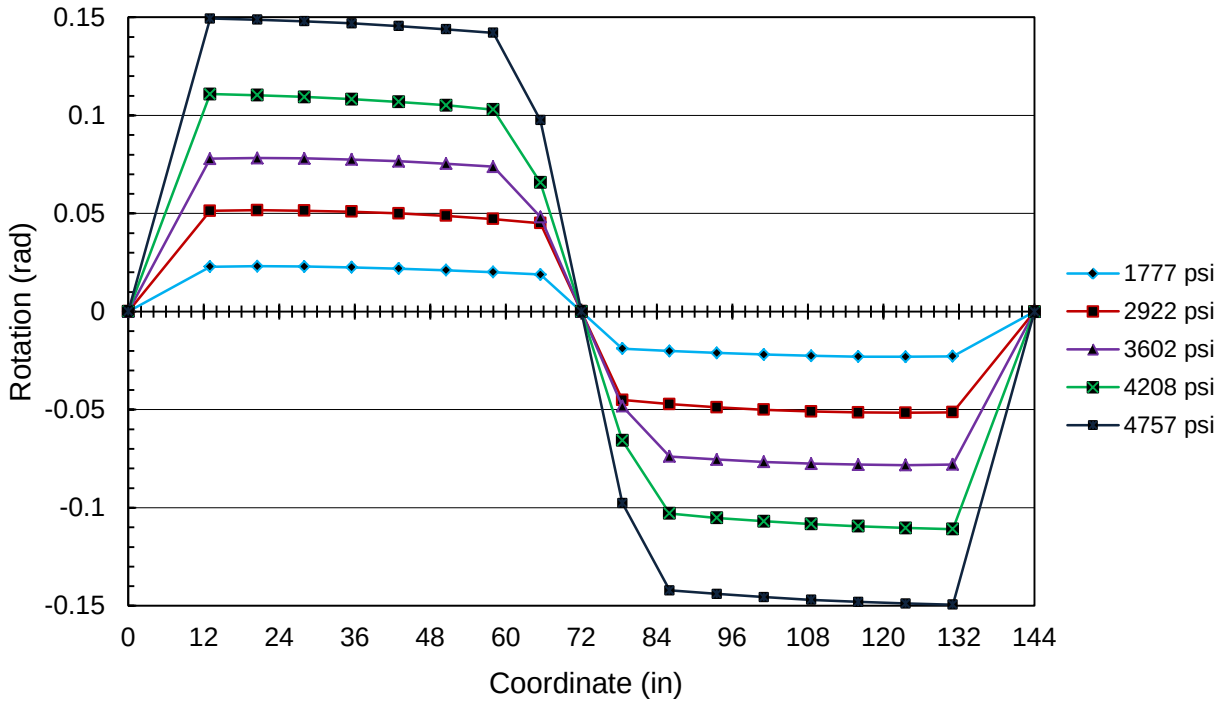

Figure 4-29. Progression of rotation of fixed UHPC column.

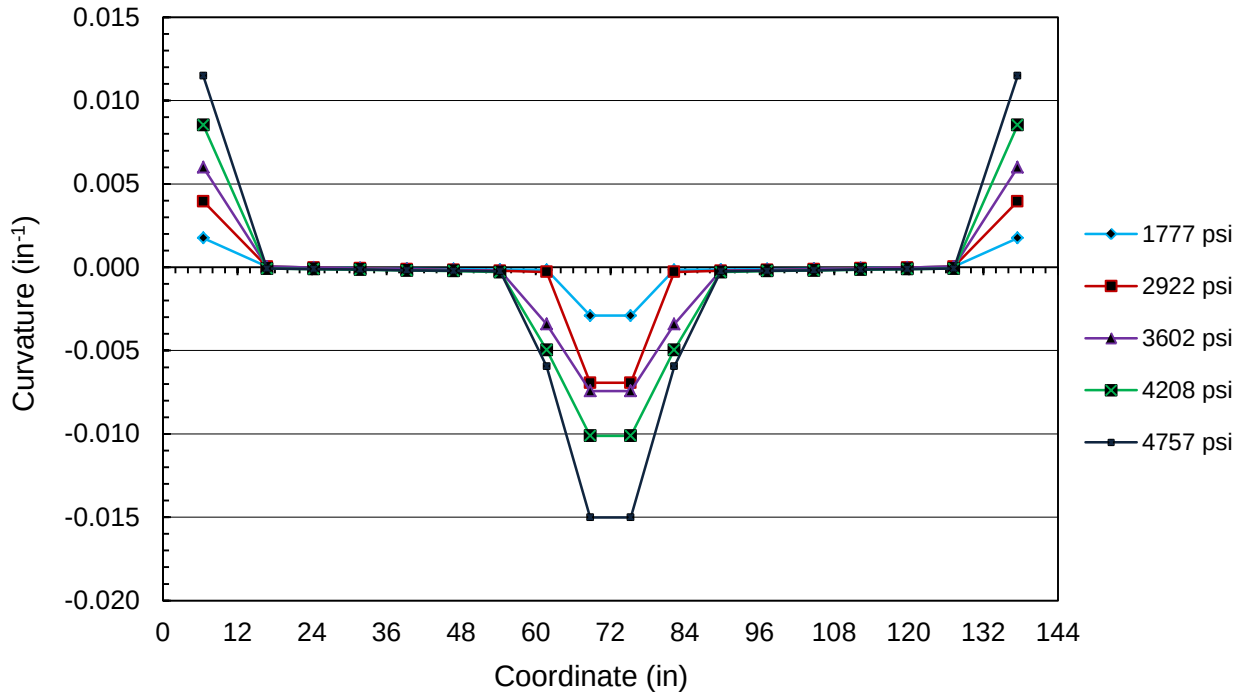

Figure 4-30. Progression of curvature of fixed UHPC column.

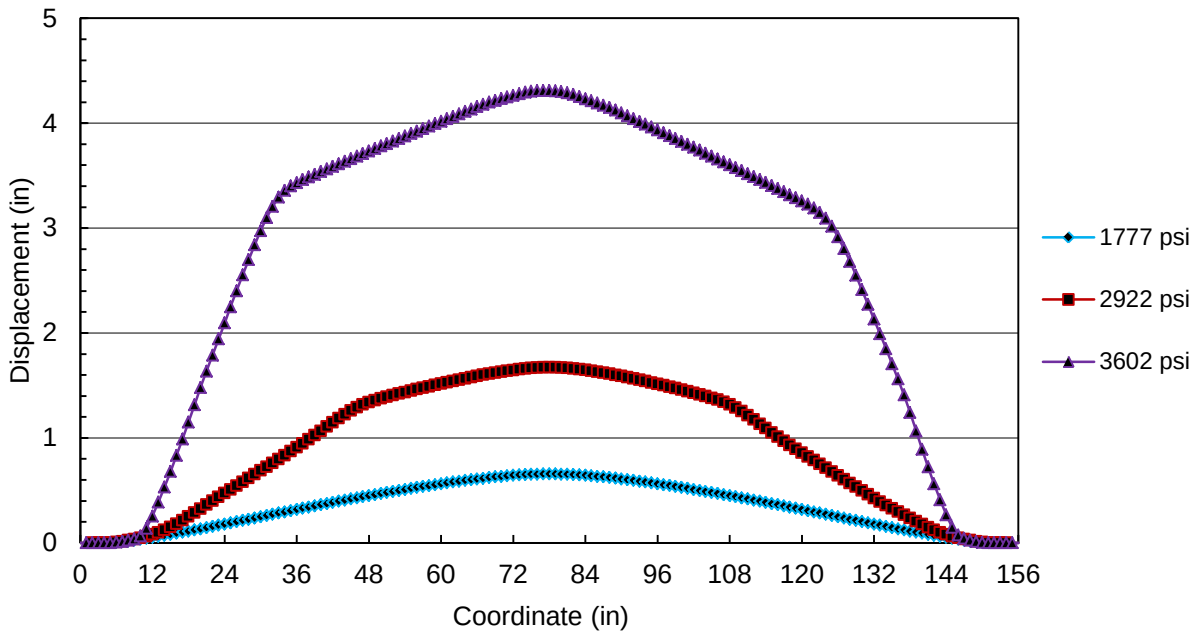

Figure 4-31. ABAQUS deflected shapes for fixed UHPC column.

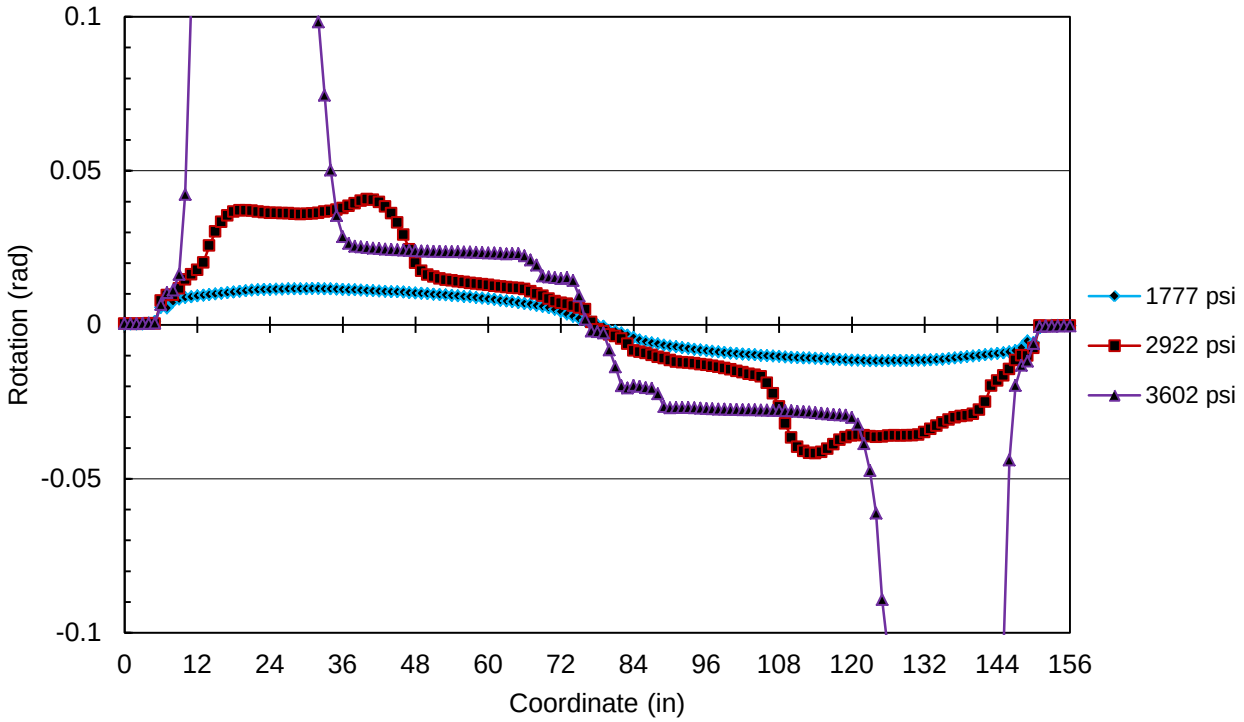

Figure 4-32. ABAQUS rotations for fixed UHPC column.

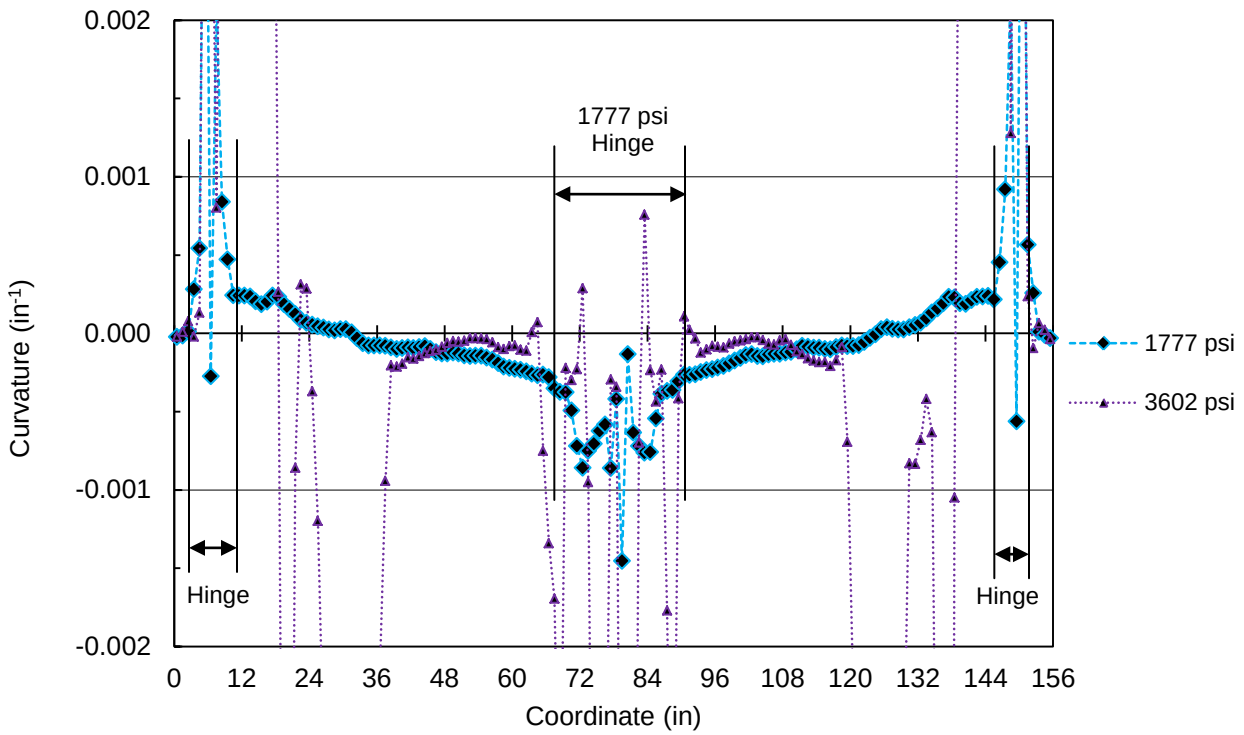

Figure 4-33. ABAQUS curvatures for fixed UHPC column.

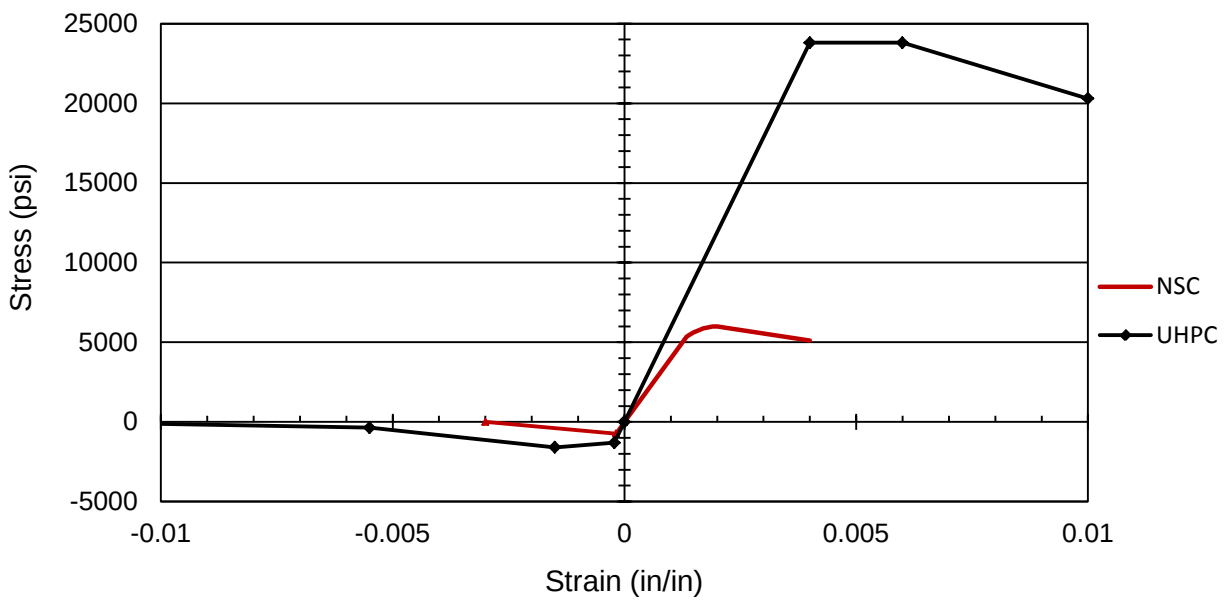

Figure 4-34. Comparison of NSC and UHPC constitutive models.

CHAPTER 5
CONCLUSIONS AND RECOMMENDATIONS

5.1 Overview

The preceding chapters examined the plastic hinge behavior relevant of normal strength and ultra high performance concretes. Chapter 1 introduced the motivation behind and the general focus of the study, while Chapter 2 provided the necessary background for conducting structural analyses of NSC concrete and an overview of UHPC's material properties and applications. Chapter 3 then organized the methodological steps by which the study was carried out, including the adaptation of DSAS's programming and the techniques employed for study validation. Finally, Chapter 4 processed the parametric study's results regarding the plastic hinge formation of concrete columns with both simple and fixed supports. This chapter in turn encapsulates the presented work as a whole and remarks on the conducted study retrospectively.

In addition to an abbreviated summary of activities, this chapter elaborates on the progress made in plastic hinge and UHPC analyses and demonstrates the need for continued experimentation in the fields of interest. Section 5.2 narrates the conclusions that can be drawn from the analysis of Chapters 3 and 4, and section 5.3 details a number of recommendations made for consideration with future endeavors. The suggestions reference the analytical tools akin to concrete members as well as the investigation of plastic hinge formation in structural entities.

5.2 Conclusions

The validation stage of the work that dealt with the Feldman and Siess (1958) beams 1C and 1H was shown to be successful. Though several assumptions were

made for the DSAS input parameters, the program's ability to simulate the beams' maximum responses was refined within engineering reason. In addition to representing the experimentally displayed behavior, the Beam-1C case exemplified correlation between DSAS and ABAQUS. The overall product of the validation was the NSC and reinforcing steel material models and the verification of properly plotting the rotation and curvature data of a concrete beam.

Regarding the peak response analysis of the NSC and UHPC columns, the greatest compatibility observed between DSAS and ABAQUS was most often for the middle range of blast pressures (2922 psi and 3602 psi). The divergence of the small and excessively large deformations is invariably, in part, a product of relating the constitutive material models between programs, especially considering ABAQUS's use of the concrete damaged plasticity model to represent the behavioral inelasticity. Individually, the two programs expressed consistent comparisons between the improved strength of using UHPC over NSC.

The plastic hinge modeling proved generally consistent with the overriding theory and demonstrated respectable correlation between DSAS and the finite element modeling of ABAQUS. Originally, the hinge element introduced to DSAS was intended to take the place of the entire hinge and spread a distance of the effective depth. Upon inspection however, the hinges formed within the column's span were consistently observed to expand two effective depth lengths in total (or a hinge length in either direction away from the critical section). Though this result was not the projected behavior, the implementation of the effective depth element eased the graphical representation of curvature for DSAS's larger mesh density. It also sufficiently

encapsulated the hinge generated at the boundaries, which proved in ABAQUS to be of a length less than effective depth. The large hinge element present at the boundaries in DSAS also weakens the depiction of curvature change when represented graphically.

The study of reinforced concrete columns clearly demonstrates the significance of plastic hinge behavior in its contribution to column failure. For fixed columns, a fully formed hinge releases the boundary constraints and enables the member to continue to act as though it were a simple support system. The final hinge to develop in a fixed column, or the only one to do so in simply supported column, provides the ultimate failure mechanism around which the column will invariably collapse under extreme forces.

Ultimately, the contrast between the NSC and UHPC columns highlighted UHPC's dominant strength and endurance. The advanced ductility of UHPC was to be expected, but the material also proved quite resistant to rotation outside of the critical sections. The NSC on the other hand exhibited excessive span yielding under the severe uniform pressures, at least via DSAS's configuration. This discrepancy introduces the plausibility of a second tier plastic hinge as demonstrated by Figure 4-7 and 4-8. Though not validated by the ABAQUS output, extensive experimental data this area would assist in the clarification. The deviation from theory may also plausibly delineate from the large meshing sized used in an attempt to capture the behavior or an error in shape data processing.

Finally, while processing the additional behavior studies of the diagonal shear, direct shear, and tension membrane behaviors, it is noted that these models and computational considerations are not necessarily translatable between NSC and UHPC.

Without proper examination of UHPC through experimentation, the shear reduction factor employed is functionally meaningless, and it was only included to provide a resemblance between the concrete types and limit the altered variables within the column study. A discrepancy also exists with the prediction of UHPC's failure amongst the lack of tension membrane consideration. Unless the transverse reinforcement is the originating cause, the UHPC should display equal ability to the NSC in terms of ductility and large deformations. The designation of failure for the US4 and US5 trials in the absence of tension membrane behavior emphasizes a need for further development of the DSAS UHPC analytical capabilities.

5.3 Recommendations

After completion of the validation and parametric studies, it is prudent to reflect upon and critique the explicated methodology and results as well as to express how they would best be implemented or adapted. This section addresses the limitations of the parametric study performed and presents recommendations for future studies relative to the inelastic hinge behavior of NSC and UHPC columns.

The congruency between the programming codes used for the dynamic analyses was foremost limited by the extent to which the material models are known. Although the NSC column properties derived from Beam-1C, which demonstrated a strong relationship between DSAS and ABAQUS, the effect of uniform pressures on the column were not equally compatible. The two code models were intended to correspond to one another, but discrepancies in the plastic material models may have resulted, especially with respect to describing the concrete plasticity model. The CDP parameters were based on previous studies and standard ABAQUS assumptions, but their true value definitions are not directly known. Also, although parametric studies have formerly

been conducted to hone on the most suitable CDP model for the Beam-1C concrete, the same background is not provided for UHPC. Instead, various dilation angles between 15 and 40 degrees were tested for the overall most reasonable compatibility with the DSAS output. The dilation angle was ultimately changed from 40 degrees (for the NSC model) to 35 degrees to more appropriately suit the UHPC.

The parametric study of plastic hinge formation was also limited by the breadths of column supports considered and the forms of loading to which they were subjected. The supports considered were idealized and therefore simplified. In reality, column supports are not precisely ‘simple’ or ‘fixed’ and demonstrate varying grades of stiffness per their degrees of freedom. Given that hinges form at the locations of highest concentrated moment, whether one is to form at a particular support or the length it would assume is dependent upon the supports’ true disposition. With respect to loadings, uniform span loads were the type primarily considered. The validation case briefly introduced the effects of a concentrated load, but no further load cases were pursued. For uniform loads, the critical point of maximum moment (not including the supports) corresponds to midspan which was appropriately identified by DSAS. Whether the program properly develops hinges along the span not at midspan, as would occur under a linearly distributed load for example, was not expressly tested. Though brief checks of the program were made to verify its functionality, such as placing a point load at the quarter span, etc., extensive studies in this fashion were not completed or compared with an alternate source (ABAQUS or experimental data).

To remedy the narrated study limitations, the recommendations made are geared toward the study of plastic hinge behavior as well as the continued development of

UHPC's characterization. It may be beneficial to run and thoroughly analyze more theoretical cases, such as the hinging of circular concrete columns, non-uniform loads, or altered UHPC behavioral models. Yet, based on the research and analytical focus of this paper, the all-encompassing recommendation is to verify the work through actual experimentation.

Addressing the topic of reinforced concrete columns, Bae and Bayrak (2008) presented findings on plastic hinges in cantilevers, and their exposition proposed a new expression for hinge lengths under severe axial loads. Their experimentations did not address varied boundary conditions or effects of critical transverse loads however. So while this case provides an example of work being conducted in the inelastic deformation regime of normal strength concrete, additional realistic data in this area would significantly benefit the analytical study.

Finally, the effort of describing concrete's complete behavior, regardless of type, is unending. To further capture the most realistic behavior of concrete structures, experimentation is required. The programming capabilities of both DSAS and ABAQUS are deterred when there is little support of their processed outcomes. Again, without a firm understanding of concrete's behavior in the inelastic regime, which is not to be modeled by a single, simple theory, the study of large deformations exponentially increases in difficulty.

Recognizing UHPC's relative youth and high material variability, the scarcity of a universally available behavioral model is to be expected. UHPC research is being conducted on a worldwide scale, yet the specific interest in large deformations or plastic hinging has not necessarily been thoroughly explored. It has been demonstrated that

the shear and tension membrane models used through the parametric study may not necessarily be replicated between normal strength and ultra high performance concretes. These areas of behavior provide just a few examples of those remaining to be further explored with respect UHPC. To better situate UHPC's use in protective structures, subjecting UHPC columns to blast and severe impact loads is crucial. Such experimentation on UHPC beams is being advanced at CIPPS, and the results will enable and lead to a more defined picture of the inelastic modes of UHPC structural members.

LIST OF REFERENCES

Abdelrazig, B. (2008). “Properties & applications of CeraCem ultra high performance self compacting concrete.” *Proceedings of the International Conference on Construction and Building Technology*, Kuala Lumpur, Malaysia, 217-226.

Acker, P., and Behloul, M. (2004). “Ductal technology: a large spectrum of properties, a wide range of applications.” *Proceedings of the International Symposium on Ultra High Performance Concrete*, Kassel, Germany, 11–23.

American Concrete Institute (ACI). (2008). “Building code requirements for structural concrete.” *ACI 318-08, ACI 318R-08*, Farmington Hills, MI.

Association Française de Génie Civil. (2002). *Bétons fibrés à ultra-hautes performances – Recommandations provisoires (Ultra High Performance Fibre-Reinforced Concretes – Interim Recommendations).* Association Française de Génie Civil, France.

Astarlioglu, S. (2008). *Dynamic Structural Analysis Suite (DSAS) User Manual*. Center for Infrastructure Protection and Physical Security (CIPPS), Gainesville, FL.

Astarlioglu, S., Krauthammer, T., and Felice, C. (2010). “State-of-the-Art Report on Fiber Reinforced Ultra-High Performance Concrete.” *Report No. CIPPS-TR-003-2010*. Center for Infrastructure Protection and Physical Security, University of Florida, Gainesville, FL.

Bae, S., and Bayrak, O. (2008). “Plastic hinge length of reinforced concrete columns.” *ACI Structural Journal*, 105(3), 290-300.

Biggs, J.M. (1964*). Introduction to structural dynamics*. McGraw-Hill, New York, NY.

Brandt, A.M. (2008). “Fibre reinforced cement based (FRC) composites after over 40 years of development in building and civil engineering.” *Composite Structures,* 86, 3-9.

Buitelaar, P. (2004). “Ultra high performance concrete: developments and applications during 25 years.” *Plenary Session International Symposium on UHPC*, Kassel, Germany.

Cavill, B. (2005). “Ductal an ultra-high performance material for resistance to blasts.” *Engineering and Research Forum*, Canberra, Australia.

Curbach, M., and Speck, K. (2008). “Ultra high performance concrete under biaxial compression.” *Proceedings of the Second International Symposium on Ultra High Performance Concrete*, Kassel, Germany, 477–484.

Dhakal, R.P., and Fenwick, R.C. (2008). “Detailing of plastic hinges in seismic design of concrete structures.” *ACI Structural Journal*, 105(6), 740-749.

Dusenberry, P.O. (2010). *Handbook for Blast Resistant Design of Buildings*. John Wiley & Sons, Inc., Hoboken, NJ.

Fehling, E., Bunje, K., and Leutbecher, T. (2004). “Design relevant properties of hardened Ultra High Performance Concrete.” *Proceedings of the International Symposium on Ultra High Performance Concrete*, Kassel, Germany, 327-338.

Feldman, A., and Siess, C.P. (1958). “Investigation of Resistance and Behavior of Reinforced Concrete Members Subjected to Dynamic Loading Part II.” *Structural Research Series No. 165*. University of Illinois, Urbana, IL.

FHWA, High Performance Concrete Technology Delivery Team. (2005). “High Performance Concrete Structural Designers’ Guide.” *Pub. No. FHWA-RCBAL-05-007*, Federal Highway Administration, U.S. Department of Transportation.

Graybeal, B.A. (2005). “Characterization of the Behavior of Ultra-High Performance Concrete.” Ph.D. Thesis, University of Maryland, College Park, MD.

Habel, K., Denarie, E., and Bruhwiler, E. (2004). “Structural response of composite UHPFRC-concrete members under bending.” *Proceedings of the International Symposium on Ultra High Performance Concrete*, Kassel, Germany, 389–400.

Habel, K., and Gauvreau, P. (2008). “Response of ultra-high performance fiber reinforced concrete (UHPFRC) to impact and static loading.” *Cement & Concrete Composites*, 30, 938-946.

Hsu, T.T.C. (1993). *Unified Theory of Reinforced Concrete.* CRC Press, Boca Raton, FL.

Japan Society of Civil Engineers. (2006). *Recommendations for Design and Construction of Ultra High Strength Fiber Reinforced Concrete Structures (Draft)*. JSCE Guidelines for Concrete No.9, Tokyo, Japan.

Jayakumar, K. (2004). “Role of silica fume concrete in concrete technology.” *Proceedings of the International Symposium on Ultra High Performance Concrete*, Kassel, Germany, 165-174.

Krauthammer, T., Schoedel, R., and Shanaa, H. (2002). “An analysis procedure for shear in structural concrete members subjected to blast.” *Report No. PTC-TR-001-2002*. The Protective Technology Center, Pennsylvania State University, University Park, PA.

Krauthammer, T., and Shahriar, S. (1988). “A computational method for evaluating modular prefabricated structural element for rapid construction of facilities, barriers, and revetments to resist modern conventional weapons effects.” *Report No. ESL-TR-87-60*, Air Force Engineering and Services Center, Tyndall Air Force Base, FL.

Krauthammer, T., Shahriar, S., and Shanaa, H.M. (1990). “Response of reinforced concrete elements to severe impulse loads.” *Journal of Structural Engineering*, 116(4), 1061-1079

Malvar, L.J., and Crawford, J.E. (1998). “Dynamic Increase Factors for Concrete.” *Twenty-Eighth DDESB Seminar*, Orlando, FL.

Markeset, G. (2002). “Ultra high performance concrete is ideal for protective structures.” *High-Performance Concrete. Performance and Quality of Concrete Structures. Proceedings, Third International Conference*, Recife, PE, Brazil, 125-137.

Millard, S.G., Molyneaux, T.C.K., Barnett, S.J., and Gao, X. (2009). “Dynamic enhancement of blast-resistant ultra high performance fibre-reinforced concrete under flexural and shear loading.” *International Journal of Impact Engineering*, 37, 405-413.

Mirza, S.A. (1990). “Flexural stiffness of rectangular reinforced concrete columns.” *ACI Structural Journal*, 87(4), 425-435.

Morency, D. (2010). “Large Deflection Behavior Effect in Reinforced Concrete Column under Severe Dynamic Short Duration Load.” M.S. Thesis, University of Florida, Gainesville, FL.

Orgass, M., and Klug, Y. (2004). “Fibre reinforced ultra-high strength concretes.” *Proceedings of the International Symposium on Ultra High Performance Concrete*, Kassel, Germany, 637–647.

Park, J.J., Koh, K.T., Kang, S.T., and Kim, S.W. (2008). “Influence on the ingredients of the compressive strength of UHPC as a fundamental study to optimize the mixing proportion.” *Proceedings of the Second International Symposium on Ultra High Performance Concrete*, Kassel, Germany, 105–112.

Park, R., and Paulay, T. (1975). *Reinforced concrete structures*. John Wiley & Sons Inc., New York, NY.

Rebentrost, M., and Wight, G. (2009). “Investigation of UHPFRC Slabs Under Blast Loads.” *UHPFRC 2009*, Marseille, France.

Rong, Z., Sun, W., and Zhang, Y. (2009). “Dynamic compression behavior of ultra-high performance cement based composites.” *International Journal of Impact Engineering*, 37, 515-520.

Roth, M.J., Boone, N.R., Kinnebrew, P.G., Davis, J.L., and Rushing, T.S. (2008). “Development of new protective solutions to counter emerging and adaptive threats.” U.S. Army Engineer Research and Development Center, Vicksburg, MS.

Schachinger, I., Mazanec, O., and Schubert, J. (2004). “Effect of mixing and placement methods on fresh and hardened ultra high performance concrete (UHPC).” *Proceedings of the International Symposium on Ultra High Performance Concrete*, Kassel, Germany, 575-586.

Schmidt, M., and Fehling, E. (2005). “Ultra-high-performance concrete: research, development and application in Europe.” *ACI Special Publication*, 228, 51-78.

Shah, S.P., and Weiss, W.J. (1998). “Ultra high performance concrete: a look to the future.” *ACI Special Proceedings from the Paul Zia Symposium*, Atlanta, GA.

SIMULIA. (2010). *Abaqus 6.10 Analysis User’s Manual*. Dassault Systèmes Simulia Corp., Providence, RI.

Smith, P.D., and Rose, T.A. (2002). “Blast loading and building robustness.” *Progress in Structural Engineering and Materials*, 4(2), 213-223.

Spasojevic, A., Redaelli, M., Fernandez Ruiz, M., and Muttoni, A. (2008). “Influence of Tensile Properties of UHPFRC on Size Effect in Bending.” *Proceedings of the Second International Symposium on Ultra High Performance Concrete*, Kassel, Germany, 303–310.

Tang, M. (2004). “High performance concrete – past, present and future.” *Proceedings of the International Symposium on Ultra High Performance Concrete*, Kassel, Germany, 3-9.

Teichmann, T., and Schmidt, M. (2004). “Influence of the packing density of fine particles on structure, strength and durability of UHPC.” *Proceedings of the International Symposium on Ultra High Performance Concrete*, Kassel, Germany, 313-323.

Tran, B.A. (2009). “Effect of short-duration-high-impulse variable axial and transverse loads on reinforced concrete columns.” M.S. Thesis, University of Florida, Gainesville, FL.

Unified Facilities Criteria. (2008). “Structures to resist the effects of accidental explosions.” *Report No. UFC 3-340-02*, U.S. Department of Defense, Washington, DC.

Williams, E.M., Graham, S.S., Reed, P.A., and Rushing, T.S. (2009). “Laboratory characterization of Cor-Tuf concrete with and without steel fibers.” *Report No. ERDC/GSL TR-09-22*, U.S. Army Corps of Engineers, Washington, DC.

Wu, C., Oehlers, D.J., Rebentrost, M., Leach, J., and Whittaker, A.S. (2009). “Blast testing of ultra-high performance fibre and FRP-retrofitted concrete slabs.” *Engineering Structures*, 31, 2060-2069.

BIOGRAPHICAL SKETCH

Tricia Caldwell received her Bachelor of Science degree in civil engineering from University of Florida in December of 2009. The following semester she continued studying at UF in pursuit of her Master of Engineering with emphasis in the area of structural engineering. Tricia worked with the Center for Infrastructure Protection and Physical Security (CIPPS) to complete her graduate research and thesis under the guidance of Drs. Theodor Krauthammer and Serdar Astarlioglu. Her research focused on the computational methods of analyzing normal strength and ultra high performance concrete columns under blast loading.